EXPERIMENTAL INVESTIGATION OF CF_3I-CO_2 GAS MIXTURES ON THE BREAKDOWN CHARACTERISTICS IN UNIFORM AND NON-UNIFORM FIELD CONFIGURATIONS

A thesis submitted to Cardiff University

in candidature for the degree of

Doctor of Philosophy

By

MUHAMMAD SAUFI KAMARUDIN

School of Engineering

Cardiff University

June 2013

All praise is to Allah, the Most Gracious, the Most Merciful
Peace and blessings be upon our Prophet Muhammad
and upon his family and companions

ACKNOWLEDGEMENTS

I would like to express my appreciation and sincere gratitude to my supervisor, Professor A. Haddad, for all his guidance, advice, support, and encouragement throughout the duration of this work. I have greatly benefited from his extensive knowledge and recognised experience in the field of high voltage engineering.

I would also like to thank the following for their contributions:

Dr. Noureddine Harid as my co-supervisor

Malcolm Seaborne for his expertise in gas handling.

Philip Leichauer for his extensive knowledge and help on the test rig construction.

All the members of the academic and administrative staff of School of Engineering, Cardiff University.

All technical staff, especially Stephen P. Mead, whose technical skills have greatly assisted me in the completion of the test rig.

Maurizio Albano, Rahisham Abd Rahman, Haziah Abd Hamid, Mohd Fahmi Hussein, Fabian Moore, Salah Mousa, Tony Chen, Khalifa Elnaddab, Philip Widger for valuable discussions and their friendship.

I would also like to thank Universiti Tun Hussein Onn Malaysia (UTHM) and the Ministry of Higher Education, Malaysia, for their scholarship award.

And my special thanks to my wife Samihah Sarpan, my children Qaisara and Zulaikha, and my parents Kamarudin Khalid and Rokiah Idris, for their selfless patience and endless support which they have shown throughout the period of my studies.

Lastly, to everyone who has contributed directly or indirectly to this work that is now being presented here, thank you.

PUBLICATIONS

i. M. Kamarudin, M. Albano, N. Harid, A. Haddad, P. Coventry, 'Study on the Potential of CF_3I Gas as Alternative for SF_6 in High Voltage Applications', Forty-fifth International Universities' Power Engineering Conference (UPEC) 31 August – 3 September 2010, Cardiff, UK

ii. M. S. Kamarudin, M. Albano, N. Harid, A. Haddad, P. Coventry, 'A Survey on the Potential of CF_3I Gas as an Alternative for SF_6 in High Voltage Applications', Fourth Universities High Voltage Network (UHVNet), 18-19 January 2011, Southampton, UK

iii. M. S. Kamarudin, M. Albano, P Coventry, N. Harid, A. Haddad, 'Potential of CF_3I as a Replacement for SF_6 in High Voltage Switchgears', Talent Management Symposium (TMS), 18 – 20 July 2011, London, UK

iv. L. Chen, M. S. Kamarudin, K. H. Elnaddab, A. Haddad, H. Griffiths, 'Gas Insulated Transmission Line using CF_3I-CO_2 Gas Mixture', Sixth Universities High Voltage Network (UHVNet), 16 – 17 January 2013, Glasgow, UK

v. L. Chen, M. S. Kamarudin, K. H. Elnaddab, P. Widger, A. Haddad, H. Griffiths, 'CF_3I and Its Mixtures: Potential for Electrical Insulation', International Council on Large Electric Systems (CIGRE) Session 45, 24 – 30 August 2014, Paris, France, *abstract accepted*

SUMMARY

This thesis is concerned with the investigation of trifluoroiodomethane (CF_3I) gas mixtures as an alternative for an insulation medium in high voltage applications. The work has involved a broad review of literature, followed by developing a test rig for carrying out experimental investigations, extensive computational modelling and simulation studies as well as extensive laboratory tests on CF_3I gas and its gas mixtures.

The literature survey reviewed the current trend of efforts taken by researchers to find solutions for minimizing the usage of sulphur hexafluoride (SF_6) as a gas insulator, focusing on CF_3I and its mixtures. The physical properties of CF_3I are investigated, along with thermal and electrical properties.

A new test rig has been designed and constructed specifically to be used for gas insulation research. The test rig is integrated with wireless temperature and humidity sensors, as well as an electrode gap length control system. The test rig is completed with a gas recovery system to ensure proper gas handling is carried out after each test.

Extensive laboratory experimental investigations on CF_3I mixtures have been completed, focusing on the mixture of CF_3I-CO_2 gas with a ratio of 30%-70%. Standard lightning impulse of 1.2/50 has been used, with both positive and negative polarity. The effects of electrode configuration, impulse polarity, electrode gap length, gas pressure, and CF_3I content have been investigated. Insulation properties such as 50% breakdown voltage (U_{50}) and *V-t* characteristics for each test condition are investigated and presented, as well as the electric field behaviour. Finite element method (FEM) has been used to determine the electric field behaviour of a given test condition. This study revealed that CF_3I gas mixtures perform better under more uniform field condition. It was also found that an increase in gas pressure will increase the insulation strength and an increase in CF_3I content is more likely to give benefit in conditions with a more uniform field when compared to less uniform field conditions. Also, relation between liquefaction temperatures of a CF_3I-CO_2 mixture with varying CF_3I content has been developed for various pressures based on literature.

Observations on solid by-products of CF_3I have also been carried out. It has been found that iodine particles are deposited on both high voltage and ground electrodes, which can affect the insulation properties of CF_3I and its mixtures.

LIST OF CONTENTS

CHAPTER 4:SIMULATION MODEL AND FUNDAMENTAL MEASUREMENT TECHNIQUES ON AIR BREAKDOWN UNDER LIGHTNING IMPULSE

LIST OF FIGURES

LIST OF TABLES

CHAPTER 1: INTRODUCTION

1.1 Background

The electrical power supply plays such an important role in today's modernized world that the quality and continuity of supply is of highest priority. Power producers have put enormous effort into ensuring demand for electricity is securely and reliably delivered to customers, ranging from a small power outlet in a house to a large processing plant. From the consumer's perspective, any interruptions to the electrical supply could be problematic, be it a blackout, voltage dip, or overvoltage that could contribute to loss of equipment, or disruption of service. In fact this could directly impact the economy as a whole, if on a large enough scale.

In a typical power system, there are three major parts, these include generation, transmission, and distribution of electricity. During generation, other sources of energy, such as wind, solar, water, and even nuclear, are converted into electrical power. The power is then transmitted in bulk by means of overhead lines or underground cables at a variety of levels which depend on the power generated, distance of transmission, loads condition at the end part and other factors. Voltage is typically increased significantly prior to transmission in order to reduce losses. The final stage of the delivery of electricity is distribution. Distribution usually involves a network of substations, again depending on the consumers' needs, these will be in different levels of rating. Figure 1.1 below shows an example of such system.

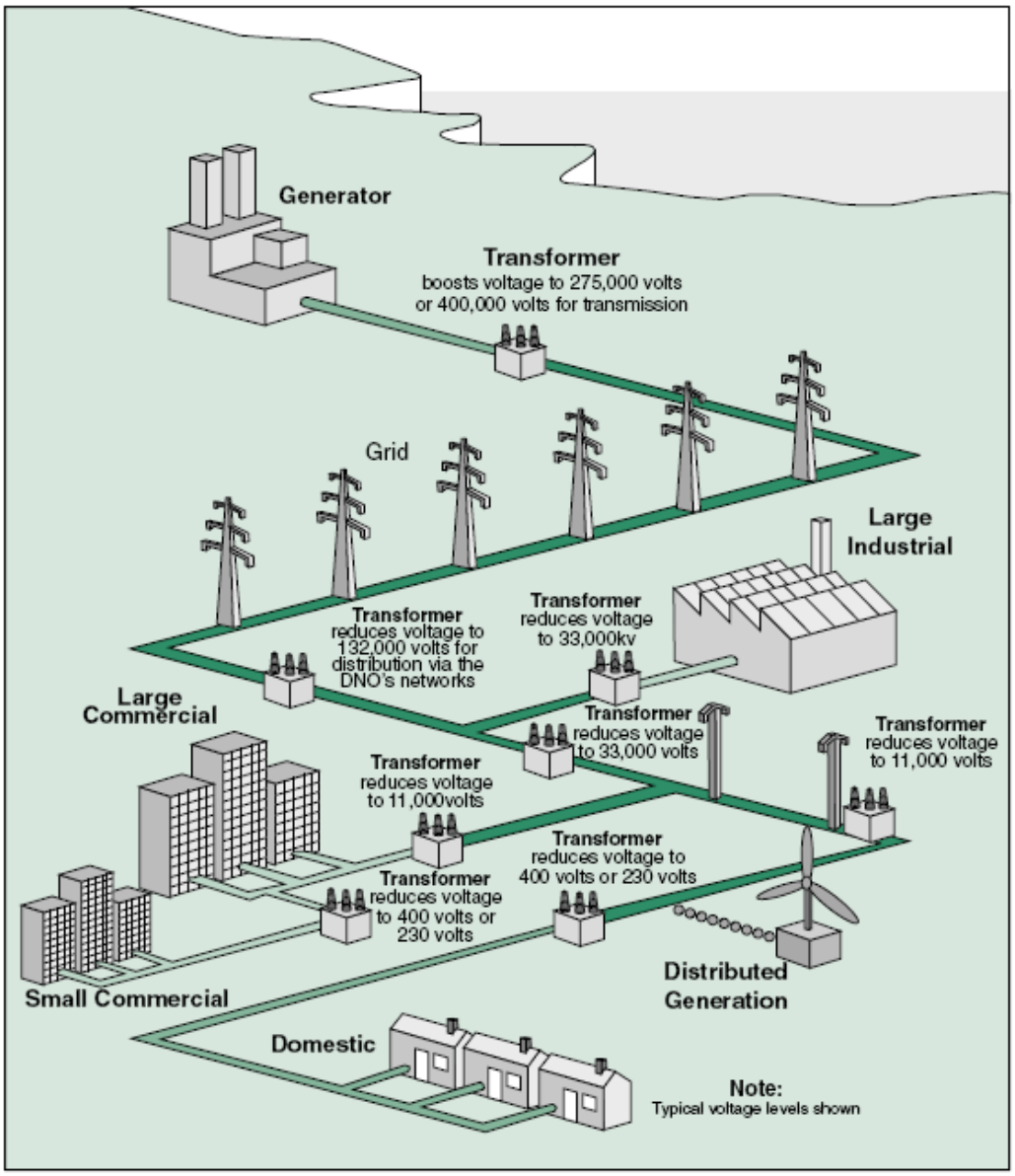

Figure 1.1: Simplified UK electrical power transmission system [1]

In an electricity network, some of the high voltage applications make use of sulphur hexafluoride (SF_6) gas as an insulation medium, such as in the gas insulated transmission line (GIL), gas insulated switchgear (GIS), and gas circuit breaker (GCB). Due to its superior insulation properties, SF_6 has been the primary insulator for many high end electrical applications. However, many studies show that SF_6 greenhouse effects raise concerns to its environmental impact. There are three major types of global

warming potential (GWP) gases: these are hydrofluorocarbons (HFCs), perfluorocarbons (PFCs), and SF_6. In addition to having high GWPs, SF_6 and PFCs have an extremely long atmospheric lifetime, resulting in an accumulation in the atmosphere once released [2]. Some of the studies in the awareness of the hazard caused by SF_6 have been well described in the following statements:

"SF_6 is a strong greenhouse gas and the molecule is very resistant against attack in the atmosphere. The natural self cleansing property of the atmosphere is insufficient to deal with such super molecules. Its production is now restricted under the Kyoto Protocol." [3]

"Sulfur hexafluoride is the most potent greenhouse gas in existence. With a global warming potential 23,900 times greater than carbon dioxide, one pound of SF_6 has the same global warming impact of 11 tons of carbon dioxide." [4]

"The atmospheric lifetime of SF_6 is 3,200 years, which results in essentially irreversible heat trapping within the atmosphere." [5]

Takuma et al [6] stated in a report that although emission of SF_6 is relatively small compared to CO_2, the global warming potential (GWP) is the highest of all available gases. For that reason, the electrical power industry has been working hard to find a replacement for SF_6 with a smaller GWP and less environmental impact. In fact, Schneider Electric has introduced the Premset switchgear [7] and Mitsubishi Electric has introduced the Dry Air Insulated Switchgear [8] to be used in medium voltage distribution which are free from SF_6.

Until recently, researchers have been trying to find suitable alternatives for SF_6. Gases and gas mixtures, especially the ones containing carbon (C) and fluorine (F), can have better dielectric strength than SF_6. Some perfluorocarbons and related mixtures are showing breakdown strengths as high as 2.5 times that of SF_6, but these are also

greenhouse gases [9]. One of the very promising candidates is trifluoroiodomethane (CF_3I). Due to its high boiling point property, CF_3I gas is mixed with other gases such as CO_2 and N_2 to provide a more practical way of deploying it as an insulation medium, since CO_2 and N_2 have lower boiling temperatures.

1.2 Direction of Research and Objectives

The focus of this study is to provide a fundamental knowledge on the breakdown properties of CF_3I and its mixtures under lightning impulses. As mentioned earlier, it is fairly important to search for good prospective insulation gases in order to find an alternative for SF_6. U_{50} and *V-t* characteristics properties will offer an insight into how well the CF_3I gas mixtures behave as an insulation medium.

For the tests to be carried out successfully, a reliable experimental setup needs to be developed. This consisted of an air-tight pressure vessel, with all the security measures, fittings, and assemblies fitted, as well as generation and measurement of the lightning impulse, and the data acquisition of the test results. A reliable gap length control is particularly important. The entire available electrodes configuration should not disturb the gas mixtures inside the vessel.

A simulation technique is needed to determine the electrical field for any given test condition. This will ensure a full understanding of the level of the maximum electric field that the CF_3I gas mixtures can handle, and to provide better insight into actual performance under electric field behaviour. The specific objectives of this study are outlined below:

i. To review current knowledge and trends in research interests related to this study, which include alternative gases for SF_6, determination of the

electric field effects, factors affecting breakdown of gases, and measurement techniques in high voltage testing;

ii. To build a novel pressure vessel as part of the test rig design and construction, with consideration given on the size, gas recovery system, gap control system, safety measures, and reliability of the vessel;

iii. To investigate the breakdown properties of CF_3I-CO_2 mixtures under lightning impulse and several factors, such as electrode configurations, polarity of lightning impulse, gap length between electrodes, pressures and CF_3I content. The gap length is limited to 5cm while the maximum lightning impulse that can be applied is limited to around 170 kV in order to protect the HV bushing of the pressure vessel; and

iv. To examine the electric field for each given test condition using an adequate model in simulation software.

1.3 Contribution of Thesis

The following contributions were achieved during this research programme:

i. Extensive literature search on CF_3I properties and its potential for high voltage applications.

ii. Designed and constructed a pressurised test chamber equipped with measurement and control apparatus, including CF_3I gas recycling.

iii. Conducted extensive tests and collected data on CF_3I gas and its mixtures which allows better understanding of breakdown properties and dielectric strength.

iv. Uniform and non-uniform field properties of the CF_3I gas and its mixtures were clarified and the effect of CF_3I content was quantified

v. Microscopic analysis of breakdown by-products was achieved.

1.4 Organization of Thesis

This thesis is divided into seven chapters:

CHAPTER 2 provides an extensive review of published literature with regard to the study undertaken. A general overview of CF_3I gas and its mixtures are presented along with previous investigations by other researchers for numerous possible mixtures, such as CF_3I-air, CF_3I-N_2, and CF_3I-CO_2, with comparison to SF_6.

CHAPTER 3 presents the development of the test rig design and construction. A detailed explanation of the construction of the pressure vessel is presented. It includes all the considerations related to fittings and assemblies, such as material, pressure relief valve, gauges, linear actuator, and other equipment. This chapter aims to give an overview of the constructed gas evacuation and filling systems as well as how the system is being assembled and operated for mixing gases.

CHAPTER 4 reports investigation and calibration tests and results related to air breakdown. Some fundamental tests with air have been carried out to verify that the test rig is working properly and as means of calibration so that it can be used for further tests with CF_3I gas mixtures. Tests were carried out according to available standards, to determine the U_{50} and *V-t* characteristics for different pressures. This chapter also presents the simulation studies undertaken with detailed explanation on the modelling to be used in numerical simulations.

CHAPTER 5 investigates the breakdown properties of CF_3I mixtures under lightning impulses. In this chapter, focus is given to CF_3I-CO_2 mixtures with a ratio of 30%-70%. Tests were carried out to investigate the effects of three electrode configurations, which are rod-plane, plane-plane, and sphere gap. The CF_3I-CO_2

mixture was subjected to both positive and negative lightning impulses. Also, the effect of gap length was investigated. Based on U_{50} results for a given test parameter, the electric field curves were determined to clarify the effect of electric field on breakdown of the gas.

CHAPTER 6, on the other hand, investigates the breakdown properties of CF_3I-CO_2 mixtures under lightning impulses for different ratios of CF_3I content apart from 30%-70%; these include 40%-60% and 20%-80%. These results will offer insight on how much influence the CF_3I gas has in terms of dielectric strength if it is mixed with CO_2. In addition, the effect of pressure was investigated. CF_3I-CO_2 mixture with a ratio of 30%-70% was tested for up to 2 bars in a rod-plane gap with variable lengths.

CHAPTER 7 presents overall conclusions based on results and findings in this study and outlines recommendations for future investigations.

CHAPTER 2: CF_3I MIXTURES AS SF_6 ALTERNATIVE: A REVIEW

2.1 Introduction

Recent developments in the search for alternative gases to replace SF_6 gas throughout the electrical power industry have triggered numerous investigations on SF_6 mixtures, other gases, and mixtures of gases. This is in terms of fundamental characteristics of insulation such as breakdown strength, voltage-time (*V-t*) characteristics, partial discharge properties, fault interruption capability and others. Although many experimental works and tests have been carried out and presented by researchers [10], [11], [12], [13], [14], [15], there are still gaps that needed to be filled in order to convince the working committee to make a decision to replace SF_6 in high voltage applications.

The aim of this chapter is to provide a comprehensive review of the studies related to the research programmes in order to provide a good understanding of one of the prospective gases in replacing SF_6 gas as an insulation medium. These include several factors including insulation characteristics, environmental properties, types of gas mixtures, and overall stability. A good understanding of these factors is vital in determining the implications and the protective performance of the gas mixtures.

2.2 Sulphur Hexafluoride (SF_6) as an Insulation Gas

Air is known as a preferred gas insulating medium in the electrical power system, but for more specific applications, such as gas insulated substations and circuit

breakers, sulphur hexafluoride (SF_6) has been widely used. SF_6 is regarded as the best gas insulation medium known in high voltage applications [6]. As indicated in the previous chapter, SF_6 is a greenhouse gas and many investigations have been carried out to find an adequate replacement [16].

Although SF_6 is colourless, odourless, and tasteless, its weight is approximately five times heavier than air. Since SF_6 is heavier than air, it tends to pool in low places, so there is a danger of suffocation through oxygen displacement. If the oxygen content in air is reduced to less than 13 percent from the normal 20 percent, nausea and drowsiness can occur [17].

When electrical discharges occur in equipment filled with SF_6, toxic by-products can be produced. These by-products are a threat to the health of workers that come in contact with the by-products. There are four types of electric discharges which will lead to decomposition of SF_6 [18]:

i. partial corona discharges,

ii. spark discharges,

iii. switching arcs, and

iv. failure arcs.

SF_6 by-products, for examples gases such as hydrogen fluoride (HF), sulfuryl fluoride (SO_2F_2), silicon tetrafluoride (SiF_4) and sulphur dioxide (SO_2), are very irritating to the eyes, nose, and throat [19]. James et. al. [20] reported that two workers collapsed after entering an SF_6 storage tower. One of the workers suffered pulmonary edema (excess collection of water fluid in the lungs) for three days. SF_6 and SO_2F_2 were then detected at the area and both exceeded the threshold limit value (TLV).

CF_3I, on the other hand, has been used in fire extinguishing systems [21]. Just as SF_6, CF_3I is also colourless, odourless, and electrically a non-conductive gas. In 1994,

Moore et. al. [22] prepared a report to illustrate the conclusion of several studies in order to replace Halon with CF_3I as a fire extinguisher. The report was based on a wide number of publications that focused on the following areas:

i. fire suppression characteristics,

ii. global environmental characteristics,

iii. toxicology information,

iv. stability for temperatures below 116 ºC in the absence of light, oxygen, and water, and

v. compatibility with other materials

It is reported that based on the toxicological, environmental, and fire fighting results for unoccupied areas and streaming applications, CF_3I was selected as a very good candidate to be used as Halon replacement, and this includes Halon 1301 and Halon 1211.

2.3 Properties Required for Power System Applications

In this section, several general characteristics for SF_6 replacement are provided for circuit breakers, gas-insulated transmission lines, and power transformers [23].

2.3.1 Circuit breaker applications

The most important physical characteristics of an insulating gas in circuit breakers (CBs) are related to the electric arc. The characteristics required for arc interruption are high dielectric strength, high interruption capability, which consist of high thermal conductivity and high electron attachment, quick gas recovery and the ability to re-form (self-healing).

2.3.2 Gas-insulated transmission lines (GIL) applications

The properties required for gas-insulated transmission line applications are different from the applications in circuit breakers. Important properties that the adopted gas needs to fulfil are high dielectric strength, long term stability, inertness and good thermal conductivity.

In particular, the gas needs to show a high dielectric strength under different stress conditions, such as uniform and non-uniform fields, electrode roughness and possible presence of conducting particles, and various geometric configurations. Although SF_6 is a good gas dielectric, its stability in non-uniform field is not as good as in uniform field, and this is a major issue [24].

There should be no possibility of chemical reaction within the electrode materials or the metallic structure and the sealing-materials in long-term use (40 years or more). There should also be no contaminations due to deposits, such as carbon deposits, polymerization, or decomposition. Other important characteristics connected to maintenance include being easily removable, having non-harmful by-products, and creating no hazards for personnel or structure, including no risk of fire, explosion, toxicity or corrosion.

2.3.3 Gas-insulated transformers applications

High rating power transformers use oils as dielectric and cooling media. However, several problems in the use of oil exist. The risk of ignition in the presence of air, breakdown due to contamination particles, and ion accumulation are all possible in insulation oils. The adoption of a gas instead of an oil can offer several advantages, such as lower risk of ignition and explosion, reduced weight of the machine and reduced noise overall (gas transmits less vibration than oil).

The properties that a gas should offer to be used successfully in power transformers are high dielectric strength at high pressure (e.g. 500 kPa), low toxicity, inertness, good thermal stability, no risk of fire, fire suppressor, high cooling capability, no reaction with various solid materials, good partial discharge characteristic, wide operative temperature range, easy to handle, a large amount available on the market and low price. Another important property is low boiling point, so that the gas will not liquefy at low temperature conditions, such as during winter time.

2.4 Physical and Chemical Properties of CF_3I

CF_3I is found to have attractive insulation properties. It is known with various names in industry. The most common synonyms for trifluoroiodomethane (CF_3I) include [25]:

- Iodotrifluoromethane,
- Trifluoromethyl Iodide, and
- Perfluoromethyl iodide.

The 3D molecular drawing for CF_3I is shown in Figure 2.1.

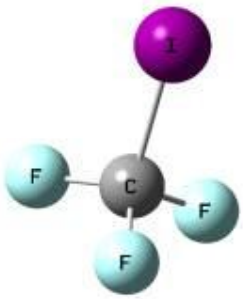

Figure 2.1: 3D molecular drawing of CF_3I, showing three fluorine atoms (light blue) and an iodine atom (purple) connected to a carbon atom (grey) [26]

CF_3I can be identified in the international databases using the following numbers:

- Chemical Abstracts Service (CAS) Number 2134-97-8 or
- European Chemical (EC) Number 219-014-5

Table 2.1 shows the physical properties of CF_3I.

Table 2.1: Physical properties of CF_3I [27]

Physical or Chemistry Property	**Value or Description**
Molecular weight	195.1
Physical state at 20°C	Gas
Melting point	– 110°C (– 166°F)
Boiling point at 1 atm	– 22.5°C (– 8.5°F)
Liquid density at – 32.5°C	2.36 g/mL
Odour threshold	Odourless
Solubility in water	Slight
Vapour pressure at 25°C	78.4 psia
Pressure-temperature curve	log psia = 5.7411-1146.82/T/K
Critical pressure	586 psia (estimated)
Critical temperature	122°C (estimated)
Critical volume	225 cm^3/mole (estimated)
Electron affinity	150 ± 20 kJ/mole
Vapour heat capacity	16.9 cal/mole-K
C-I bond dissociation energy	54 kcal/mole
Vapour density (air = 1)	6.9

As discussed in Chapter 1 (*Introduction*), one of the main reasons for researchers to search for an alternative gas to replace SF_6 is due to the concern about the SF_6 greenhouse effects. The global warming potential (GWP) of SF_6 is so high that its production has been restricted under Kyoto Protocol [28]. CF_3I, on the other hand, has a

very low GWP. Table 2.2 below shows a comparison between CO_2, SF_6, and CF_3I in terms of environmental attributes.

Table 2.2: Lifetimes, radiative efficiencies and direct GWPs relative to CO_2 [29]

Gas	Life time (years)	Radiative efficiency (W m^{-2} ppb^{-1})	GWP for given time horizon (years)		
			20	100	500
CO_2	N/A	1.4×10^{-5}	1	1	1
SF_6	3200	0.52	16300	22800	32600
CF_3I	0.005	0.23	1	0.4	0.1

In order to replace SF_6 with CF_3I successfully several physical characteristics need to be investigated. The first property that must be fulfilled is that of a high dielectric strength. The dielectric strength of the selected gas needs to offer a higher value than air and the same order of SF_6 in order to use the same design applied in current GIS systems. A comparative list with dielectric strength of various gases expressed as relative value to SF_6 is shown in Table 2.3:

Table 2.3: Breakdown strengths of selected gases relative to SF_6 [23]**,** [30]

Gas	Relative strength to SF_6	Electron attaching
C-C_6F_{12}	≈2.4	Very strong or strong
C_4F_6	≈2.3	
C-C_4F_6	≈1.7	
C-C_4F_8	1.3	
CF_3I	1.21 (107.7 kV/cm)	
SF_6	1.0 (89 kV/cm)	
C_3F_8	0.9	
CO	0.4	Weak
N_2O	0.44	
CO_2	0.3	
Air	≈0.3	
N_2	0.36	Non-attaching
H_2	0.18	

2.4.1 Electron Interaction Properties

It has been reported in [23] that in order to present good dielectric strength, the gas should present with the ability to reduce the number of free electrons. Therefore the following properties need to be considered:

- electron attachment or electronegative property for removing free electrons by attachment;
- the ionization cross section should present a low value in order to offer a reduced number of free electrons;
- electron slowing-down properties should allow a slowdown of electrons in order to facilitate their capture at lower energy; and
- the electron impact ionization should have a high value as it prevents the ionization by electron impact.

De Urquijo et al. [31], [32], [33] as well as Deng and Xiao [34] have determined electron interaction properties of CF_3I, CF_3I-N_2 and CF_3I-CO_2 mixtures using a pulse Townsend experiment and Boltzmann equation analysis. In particular, the electron drift velocity v_e, the effective ionization coefficient $(\alpha-\eta)/N$, and the limiting field strength E/N_{lim} for CF_3I and its mixture with N_2 and CO_2 at different percentages were published. In these properties, α is electron impact ionization coefficient, η is the attachment coefficent, E is the electric field and N is the gas density.

2.4.1.1 Electron Drift Velocity, v_e

Figure 2.2 depicts the electron drift velocities for CF_3I-N_2 and CF_3I-CO_2 for various levels of pressure in comparison with SF_6.

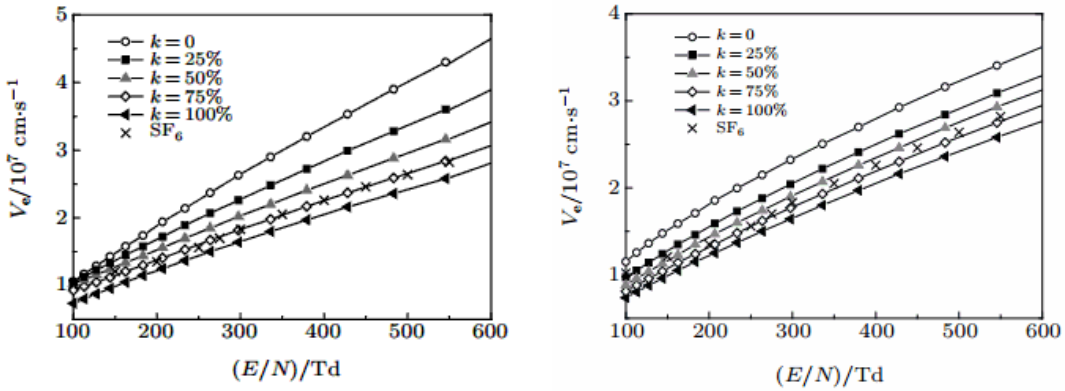

(a) CF_3I-N_2 **(b) CF_3I-CO_2**

Figure 2.2: Electron drift velocities as a function of E/N at different CF_3I ratio *k* in comparison with SF_6 [34]

It is clear that the electron drift velocity (v_e) decreases as the CF_3I content increases for both gas mixtures, as expected with an electronegative gas as in CF_3I. The v_e for CF_3I-N_2 mixtures of 75%-25% gives the same value with those of SF_6. Using the same mixture ratio, CF_3I-CO_2 gives slightly lower v_e than SF_6.

2.4.1.2 Effective Ionization Coefficient, (α-η)/N

The density-normalized effective ionization coefficient (α-η)/N, calculated by Deng and Xiao [34], indicates that (α-η)/N increases when E/N increases for both CF_3I-N_2 and CF_3I-CO_2 gas mixtures, as shown in Figure 2.3. Interestingly, for CF_3I-N_2 mixtures, where E/N is more than 300 Td, the increment of (α-η)/N for the mixtures tends to be higher than that of pure N_2 itself. This calculation has been confirmed by de Urquijo et al. [31] as noted in the experimental results.

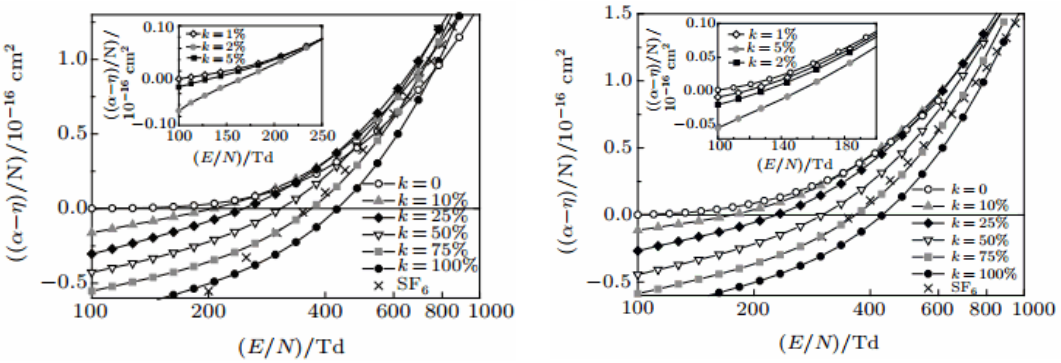

(a) CF_3I-N_2 **(b) CF_3I-CO_2**

Figure 2.3: Density-normalized effective ionization coefficients (α-η)/N as a function of E/N at different CF_3I gas mixture ratio *k* in comparison with SF_6 [34]

2.4.1.3 Limiting field strength, E/N_{lim}

The limiting field strength, E/N_{lim} is given when ionisation is equal to attachment, $\alpha = \eta$ and when $(\alpha-\eta)/N = 0$. The critical field strength of pure CF_3I is 473 Td, and is higher than that SF_6 which is 361 Td [31], [32], [33]. Figure 2.4 depicts the E/N_{lim} values for CF_3I-N_2 and CF_3I-CO_2 mixtures in comparison with SF_6-N_2 mixture, since it has been widely used as a binary gas mixture for power equipment [34].

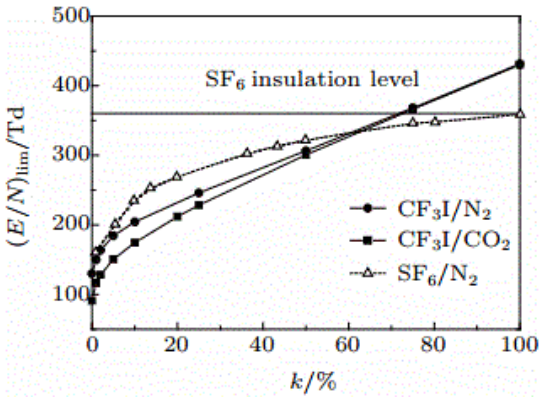

Figure 2.4: The limiting field, E/N_{lim} as a function of CF_3I and SF_6 gas content *k* [34]

For a lower content of CF_3I (< 30%) in its mixtures, E/N_{lim} of CF_3I-N_2 is higher than that of CF_3I-CO_2. In mixtures where CF_3I is more dominant, the E/N_{lim} values are the same for both mixtures, and at 60% or more of CF_3I, the E/N_{lim} values are higher than SF_6-N_2. If the content of CF_3I is more than 75%, mixtures of CF_3I with N_2 or CO_2 are even better for pure SF_6.

2.5 Thermal Properties of CF_3I

A good gas insulation medium for high voltage equipment should show good characteristics under high vapour pressure and high temperature. A high vapour pressure avoids the possibility of phase change from gas into liquid for a given temperature range. High thermal conductivity, on the other hand, ensures the gas has a good cooling characteristic. In this part, saturation vapour pressure curve for CF_3I is analyzed.

Duan et al. [35] measured the saturated densities of the gas from which the critical point parameters were calculated:

- critical density ρ_c 868 kg m^{-3}
- critical temperature T_c 396.44 K (123 °C)
- critical pressure P_c 3.953 MPa

In another study, Duan et al. [36] measured several vapour pressure data points for CF_3I and an analytical correlation of pressure and densities were derived. The pressure-temperature conditions of phase change are demonstrated by:

$$\ln\left(\frac{P}{P_c}\right) = (A_1\tau + A_2\tau^{1.25} + A_3\tau^3 + A_4\tau^7)\frac{T_c}{T} \qquad (2.1)$$

where

τ: $1-T/T_c$

T_c: critical temperature

P_c: critical pressure

A_i: coefficients, as shown in Table 2.4

Table 2.4: Coefficients for Eqn. (2.1) [36]

A_1	A_2	A_3	A_4
-7.19045	1.34829	-1.58035	-5.46680

The saturation vapour pressure curve for CF_3I is then plotted using MATLAB based on Eqn. (2.1). Figure 2.5 below, shows the CF_3I curve along with those for SF_6, CO_2, and N_2, which are taken from [37], [38], and [39]. Figure 2.6 shows the same curves for pressure between 0.1 MPa to 1.0 MPa.

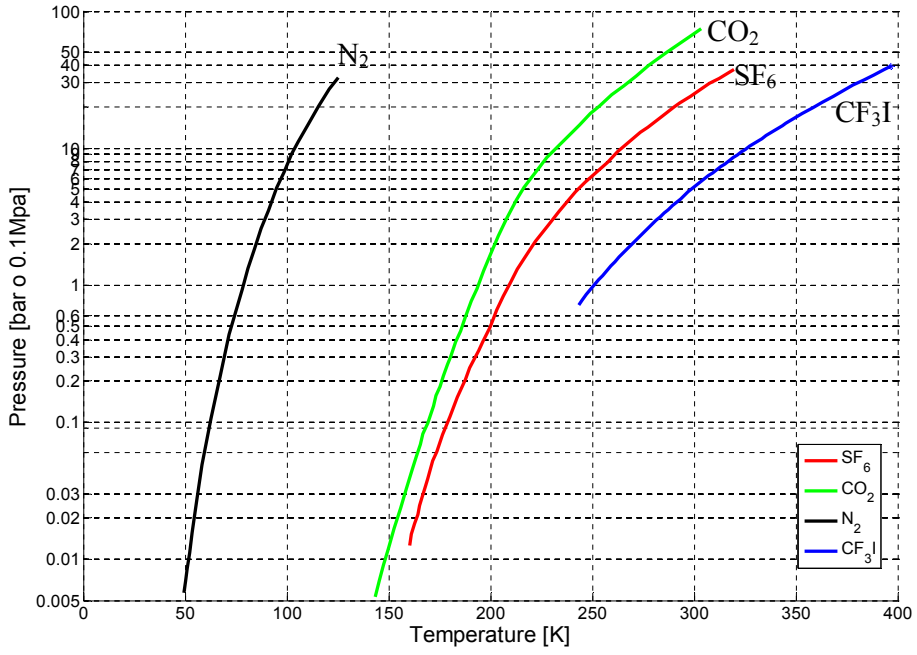

Figure 2.5: Saturation vapour pressure curves for SF_6, CO_2, N_2, and CF_3I

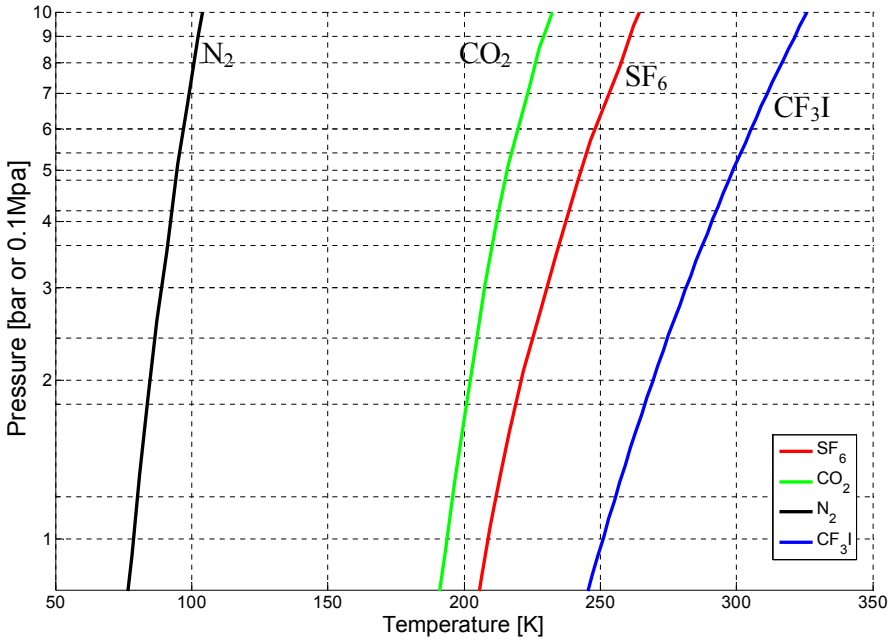

Figure 2.6: Saturation vapour pressure curves for SF_6, CO_2, N_2, and CF_3I (0.1 MPa to 1.0 MPa)

Based on Figure 2.6, at 0.1 MPa, the boiling points for CF_3I and SF_6 are approxiamately 251K (–22.15ºC) and 208K (–65.15ºC), respectively. According to Katagiri et al. [40], a typical gas-insulated circuit breaker (GCB) for GIS uses SF_6 gas at 0.5 MPa as the insulation medium. Again, by referring to Figure 2.6, at 0.5 MPa, the boiling points for CF_3I and SF_6 are given at around 298 K (24.85ºC) and 243 K (–30.15ºC). As a reference, Figure 2.7 shows the saturation vapour pressure curves for CF_3I and SF_6 as given by Katagiri in [40].

It is clear that it can be difficult to use compressed pure CF_3I in HV switchgear under these conditions. As an example, during winter times in certain countries, the temperature may drop to lower than –22.15ºC. If this occurs, then the CF_3I gas will liquefy. The adoption of other gases, such as nitrogen (N_2) or carbon dioxide (CO_2) as a

mixture in CF_3I, helps in reducing the boiling point, and it is absolutely required for outdoor application. This is required in order to prevent CF_3I from liquefying.

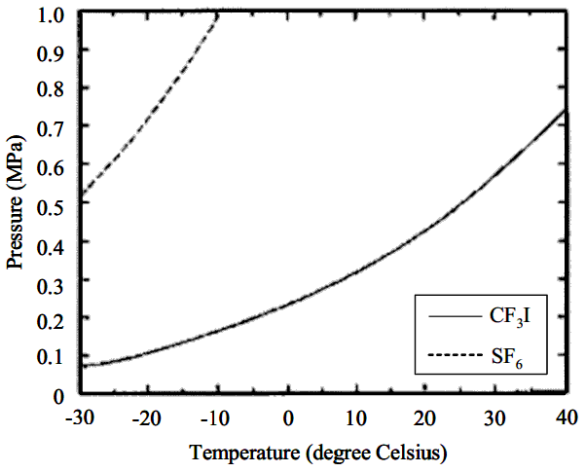

Figure 2.7: Saturation vapour pressure curves for CF_3I and SF_6 as given by [40]

According to Dalton's law, the total pressure of mixture of gases equals the sum of the pressures that each would exert if it were present alone as depicted in Eqn. (2.2) below.

$$P_T = P_1 + P_2 + \ldots + P_n \quad \text{or} \quad P_T = \sum_{i=1}^{n} P_i \qquad (2.2)$$

where

$P_1, P_2, \ldots, P_n$ represent the partial pressure of each gas

Kasuya et al. [41], [42] and Katagiri et al. [40], [43] reported that at 0.5 MPa, the boiling point of CF_3I-CO_2 (40%-60%) and CF_3I-CO_2 (30%-70%) gas mixtures are about –5 ºC and –12 ºC, respectively. Referring to Figure 2.6, the boiling point for pure CF_3I gas at 0.5 MPa is around 300 K (26.85 ºC). Further discussion on the boiling point of CF_3I-CO_2 gas mixtures is presented in Section 6.3.3.

2.6 Electrical Properties of CF_3I and Its Mixtures

Insulation properties, such as voltage-time (*V-t*) characteristics, 50% breakdown voltage (U_{50}), and interruption capabilities, need to be investigated before a gas or gas mixture is used as a gas insulation medium in high voltage applications. Many researchers are focusing on mixing CF_3I with either CO_2 or N_2, since both gases are easily available and have a much lower boiling point [40], [44], [41]. However, due to the fact that CF_3I has just recently become known (less than 20 years) to have promising insulation characteristics, investigation reports on CF_3I and its mixtures are not as many as for SF_6. Only recently has there been progressive work on CF_3I mixtures. Hence the opportunity to explore its capabilities as an insulation medium is expansive.

2.6.1 50% Breakdown Voltage (U_{50})

It is possible to investigate U_{50} as a self-restoring insulation, such as a gas insulator, and in this case, CF_3I. U_{50} can be evaluated by using two methods [45]:

i. the multiple-level method with at least four (4) voltage levels, and at least ten (10) impulses per level, and

ii. the up-and-down method with one (1) impulse per group and at least twenty (20) useful applications.

2.6.1.1 50% Breakdown Voltage (U_{50}) of CF_3I

It is known that CF_3I has a dielectric strength of around 1.21 times higher than SF_6 [23], [30]. Toyota et al. [46] evaluated U_{50} for both SF_6 and CF_3I gases in their research. Under the application of a steep front square voltage with a wave front of 16 ns, Toyota measured the U_{50} using the up-and-down method, and the results are shown

in Table 2.5. The measurements were carried out with a rod-plane gap, with the tip radius of the electrode is given as 0.4 mm, the pressure was 0.1 MPa.

Table 2.5: 50% breakdown voltage, U_{50}, for SF_6 and CF_3I gases at 0.1 MPa under steep front square voltage application [46]

Gas	Gap length	Polarity	U_{50}
SF_6	10 mm	Positive	47 kV
		Negative	–52 kV
	20 mm	Positive	64 kV
		Negative	–98 kV
CF_3I	10 mm	Positive	35 kV
		Negative	–61 kV
	20 mm	Positive	46 kV
		Negative	–84 kV

From the above table, for a gap length of 10 mm, U_{50} for CF_3I is around 0.74 times lower than SF_6 under positive polarity, but 1.17 times higher than SF_6 under negative polarity. Meanwhile, for a gap length of 20 mm, in both polarities, U_{50} for CF_3I is lower than SF_6, with 0.72 times under positive polarity and 0.86 times under negative polarity.

However, there is inconsistency within the negative polarity results. For a 10 mm gap length, U_{50} for CF_3I is lower than SF_6, while it is higher in a 20 mm gap length. This is due to a change in the gap geometry, and hence, a change in field utilization factor. For a rod-plane electrode system, an increase in gap length will result in a decrease in field utilization factor, which represents more non-uniform electric field configuration. As have been reported by Takeda et al. [47], CF_3I has lower sparkover voltages in lower field utilization factors, as compared to SF_6.

2.6.1.2 50% Breakdown Voltage (U_{50}) of CF_3I Mixtures

Further tests on U_{50} have been carried out by Katagiri et al. [40]. For these measurements, CF_3I was mixed with CO_2 in various ratios to investigate the effects of CF_3I content on a given test condition. By applying standard lightning impulse voltage, with a sphere gap of 10 mm apart, the results on the aforementioned tests were obtained (see Figure 2.8).

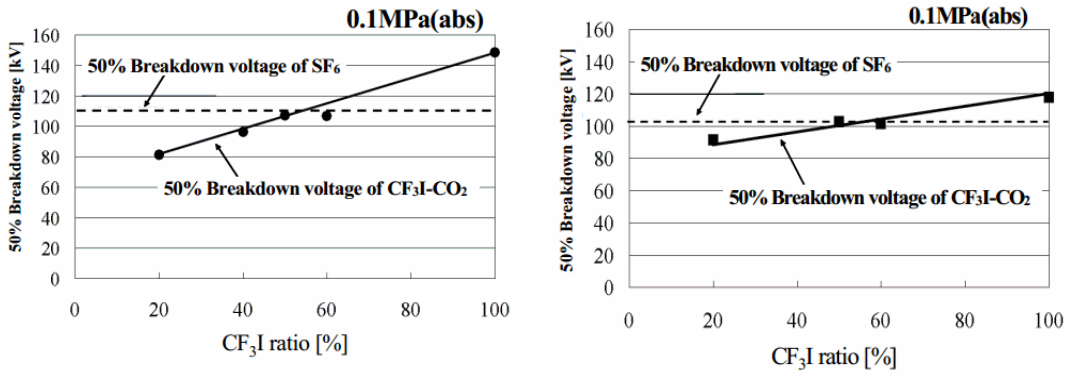

(a) Positive polarity **(b) Negative polarity**

Figure 2.8: U_{50} for CF_3I-CO_2 mixtures [40]

For this electrode system, it is clear that the U_{50} for pure CF_3I is higher than the given U_{50} of SF_6, which is around 1.2 times better. In both polarities, the U_{50} curves increase linearly with the proportion of CF_3I. At a CF_3I ratio of 60%, the dielectric strength of the CF_3I-CO_2 mixture is close to that of SF_6. The U_{50} for SF_6 presented is higher than the rated 89 kV, due to the tests being carried out with lightning impulse, where statistical effect of electron production plays a major role. According to Anis and Srivastava [48], the space charge due to corona under lightning impulses does not have sufficient time to stabilize, which is also related to rate of production of initiatory electrons. A lightning impulse, which happens in a very short period, then requires higher electric field (and hence higher voltage) to provide a condition for breakdown.

Under static electric field conditions, such as in dc voltage, the U_{50} for SF_6 would be around 89 kV.

However, according to Katagiri et al., because of the high boiling point of CF_3I, the proportion of CF_3I in the mixture should not be more than 30% which gives the dielectric strength of CF_3I-CO_2 (30%-70%) of around 0.75 to 0.8 times that of SF_6. It should be noted that these measurements were carried out with only fifteen (15) breakdown tests [40]. If the measurements were using an up-and-down method, the tests should be carried out with at least twenty (20) useful applications to conform to the international standard BS EN 60060-1 (2010) [32].

2.6.2 *V-t* characteristics

Another characteristic used to evaluate the insulation performance for a gas, considers the *V-t* characteristic which represents the relationship between the breakdown voltage and time to breakdown. If the voltage used in the measurements is a standard lightning impulse waveform, the breakdown can occur before, after, or at the peak value. The value of voltage when the breakdown occurs and its associated time lag are recorded and used to plot the *V-t* characteristics, as shown in Figure 2.9.

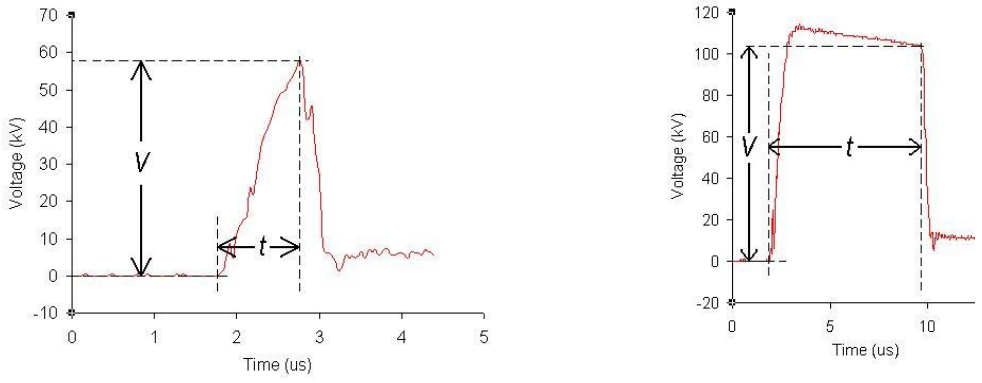

(a) **(b)**

Figure 2.9: Breakdown (a) before and (b) after peak of lightning impulse

2.6.2.1 *V-t* characteristics of pure CF_3I

In 2005, Toyota et al. [46], [49] compared CF_3I *V-t* characteristics with SF_6, with emphasis given to non-uniform field conditions. Toyota applied a steep-front square voltage with a front wave of 16 ns and a peak value up to 200 kV. These short time range measurements are useful in dealing with very fast, transient overvoltage problems caused in GIS. Another impulse voltage has been used in the tests characterised as 1.8/450 μs, in which the wave front was similar to the lightning impulse.

The electrodes were configured as rod-plane system, with a radiation source installed behind the plane electrode to promote the initial electrons generation. By using Cobalt-60, the electrons are accelerated towards the anode. This irradiation technique was used to overcome the statistical variability [48]. The results are shown in Figure 2.10 and Figure 2.11.

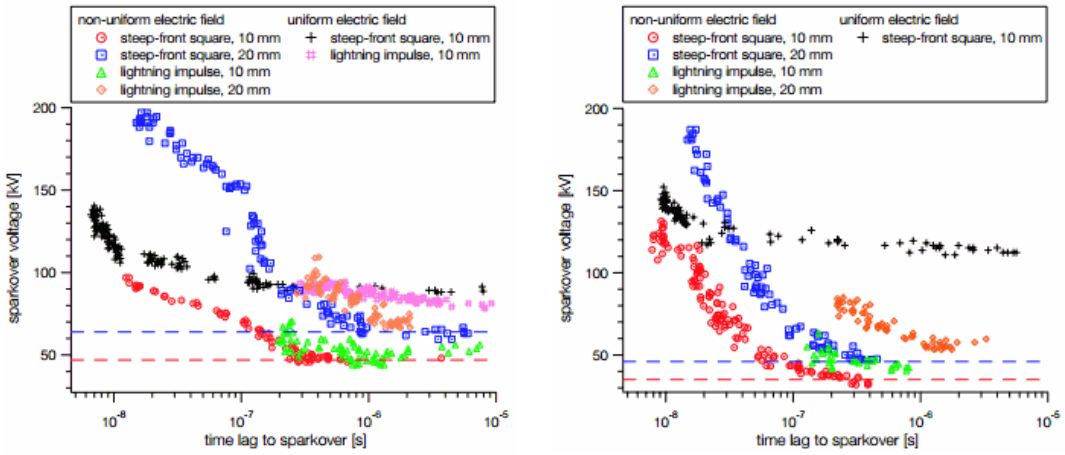

(a) SF_6 **(b) CF_3I**

Figure 2.10: *V-t* characteristics at 0.1 MPa [46] **under positive polarity. Dashed lines indicate U_{50} in Table 2.5**

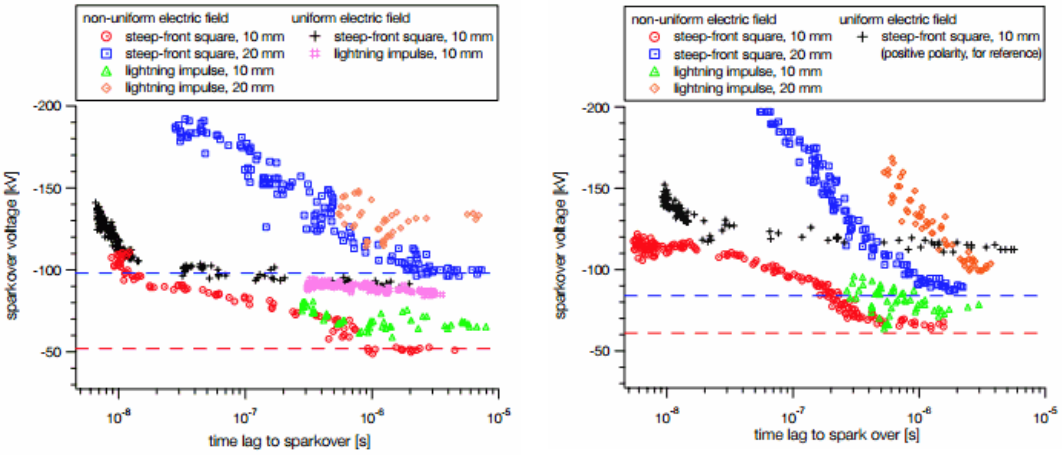

(a) SF_6 **(b) CF_3I**

Figure 2.11: *V-t* characteristics at 0.1 MPa [46] **under negative polarity. Dashed lines indicate U_{50} in Table 2.5**

Toyota found that for the same period, in the time lag (t), the sparkover voltage (V) under steep front square voltage is lower than those at 1.8/450 μs lightning impulses (non-standard). This effect is not easily explained.

Takeda et al. [47], [50], [51] carried out further tests on *V-t* characteristics for CF_3I with more options in electrode configurations, by applying the same steep front square voltage. The field utilization factors, which is a function of the geometrical characteristic (the mean electric field/the maximum electric field) for each electrode configuration are shown in Table 2.6. Takeda's findings are summarized in the Figure 2.12.

Figure 2.12 shows that higher field utilization factors (0.38 onwards) for CF_3I, have higher *V-t* characteristics (the *V-t* characteristics shifted upwards), while for a low field utilization factor, SF_6 is better in terms of *V-t* characteristics. This might be of interest since in order for CF_3I to replace SF_6 fully as an insulation medium, CF_3I has to have a better *V-t* characteristics for all types of electrode configurations, since they represent various kinds of high voltage apparatus.

Table 2.6: Field utilization factors for different electrode configurations [47]

Electrode configuration	Field utilization factors
100 mm hemisphere	0.89
ϕ 12 mm hemispherical rod	0.45
ϕ 6 mm hemispherical rod	0.38
Conical rod (r=0.4 mm)	0.095

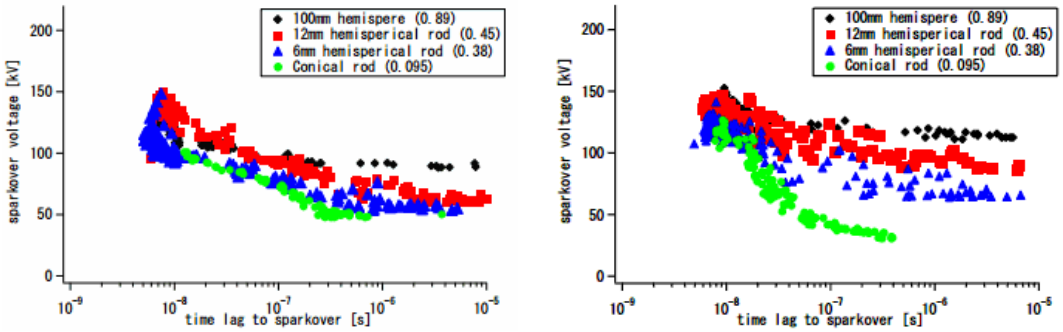

(a) SF_6 **(b) CF_3I**

Figure 2.12: *V-t* characteristics for gap 10mm; positive polarity [47]

2.6.2.2 *V-t* Characteristics of CF_3I Mixtures

In 2006, Nakauchi et al. [52] reported that sparkover voltage in a CF_3I-N_2 mixture is almost the same as that in a CF_3I-CO_2 mixture under square pulse voltage. Toyota et al. [49] carried out further tests on *V-t* characteristics for several CF_3I mixtures, namely CF_3I-N_2 and CF_3I-Air mixtures. A 50 mm radius hemisphere-to-plane electrode is used in the tests, giving a field utilization factor of 0.89 when the gap is 10 mm. Again, the CF_3I mixtures were subjected to steep front square wave voltage with a rise time of 20 ns. The total pressure of the gas is 0.1 MPa. The tests are carried out for positive polarity only. Figure 2.13 shows the summary of these findings [49].

It can be concluded that the *V-t* characteristics for both CF_3I-N_2 mixtures are almost identical. For both mixtures, with a CF_3I ratio at 60%, the *V-t* characteristics will

be the same as that of pure SF_6, as has also been reported in [53]. Therefore, the same dielectric strength is obtained. This is the same amount Katagiri et al. [40] reported in the investigation on U_{50} for CF_3I-CO_2 mixtures, in which around 60% of CF_3I, the CF_3I-CO_2 mixture gives approximately the same voltage level as U_{50} for SF_6.

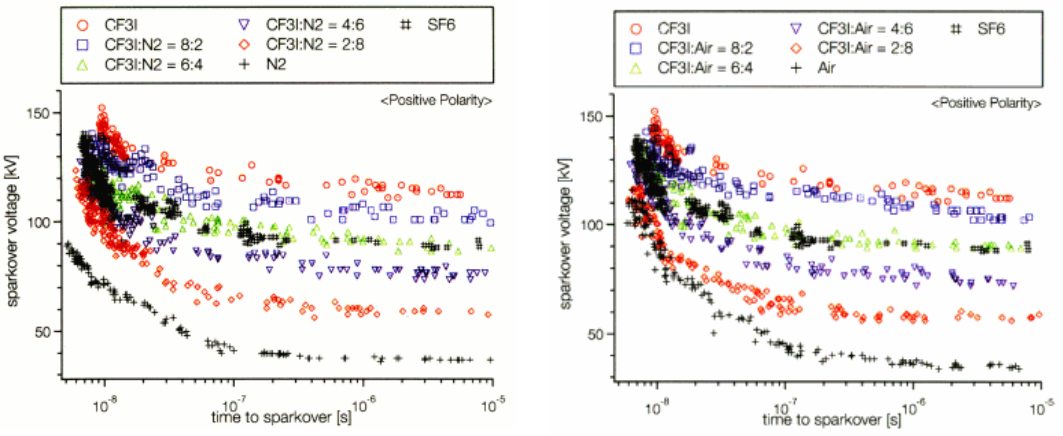

(a) CF_3I-N_2 **(b) CF_3I-Air**

Figure 2.13: *V-t* characteristics at 0.1 MPa [49]

2.6.3 Other electrical properties for CF_3I and its mixtures

Interruption capabilities of CF_3I have been investigated by Katagiri et al. [40] and [54], Taki et al. [44] and Kasuya et al. [41]. Using a model of an arc-extinguishing chamber, the authors investigated short line fault (SLF) and breaker terminal fault (BTF) interruption capabilities of CF_3I, CF_3I-N_2, and CF_3I-CO_2 mixtures compared to SF_6. It was found that although dielectric strength of CF_3I is 1.2 times higher than SF_6, SLF interruption performance of CF_3I is around 0.9 times that of SF_6, and BTF interruption performance is almost 0.7 times that of SF_6.

Katagiri also reported that the interruption performance of CF_3I-CO_2 mixtures is higher than CF_3I-N_2 mixtures. This is thought to be due to the electron attaching

properties of CO_2 which are better than N_2. A clearer view of this is depicted in Figure 2.14. An interesting point to be considered is that for CF_3I-CO_2 mixtures with at least 30% of CF_3I, interruption performance is almost the same of that of pure CF_3I. This gives a good indication, in terms of boiling point, of the gas mixture.

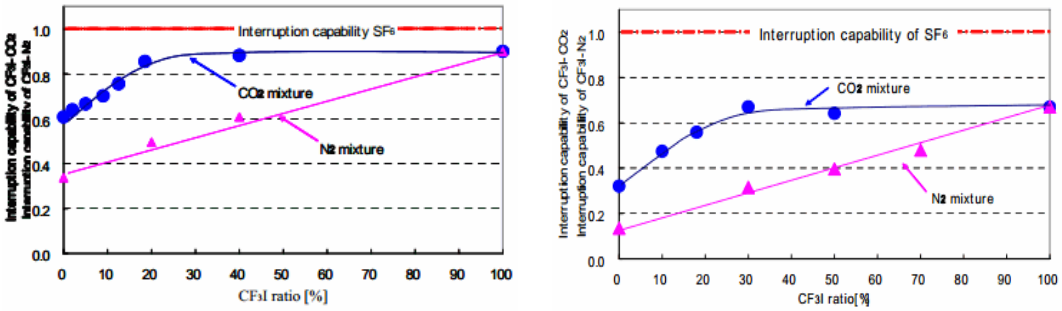

(a) SLF **(b) BTF**

Figure 2.14: Interruption capabilities of CF_3I, CF_3I-N_2 and CF_3-CO_2 mixtures as compared to SF_6 [40]

Takeda et al. [47] and [55] carried out further tests on CF_3I to investigate surface flashover characteristics. A polytetrafluoroethylene (PTFE) dielectric is placed between two plane electrodes, immersed in CF_3I gas, with the application of steep front square wave voltage. It was found that, upon a surface discharge in CF_3I, the subsequent flashovers are lower than the previous ones. Upon investigation, a brownish material is found to be deposited on the PTFE surface, and this was later identified as iodine. The deposition of iodine increases with each flashover. It is possible that solid iodine deposited along the path of flashover may conduct current and, hence, may decrease the insulation performance of CF_3I gap.

2.7 *By-products of CF_3I*

One of the major concerns in SF_6 use is by-product production upon electrical discharges. SF_6 by-products, such as SO_2F_2, SiF_4, and SO_2, are very irritating to the eyes, nose, and throat [19]. Due to this, the need to investigate the by-products of CF_3I, particularly in terms of insulation performance and dielectric strength are present.

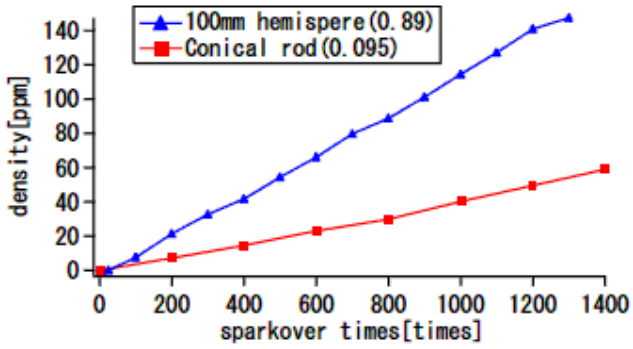

Figure 2.15: Relation between C_2F_6 and amount of sparkover times with different electrodes [57]

Investigations on gaseous decomposition of CF_3I have been carried out by Takeda et al. [47] and [57] and Kamarol et al. [58], using gas chromatography-mass spectrometry (GC-MS) to measure the by-products qualitatively and quantitatively. In the measurements, C_2F_6, C_2F_4, CHF_3, C_3F_6, C_3F_8, and C_2F_5I are detected as gaseous by-products generated by sparkover. In these investigations, the amount of these by-products is found to be higher under uniform fields than that in non-uniform fields. This is due to the fact that higher breakdown voltage is needed in uniform fields, which related proportionally to the energy (energy, $E \propto V^2$) produced during the breakdown. C_2F_6 has the highest quantity among the gases, and this decomposition seems to be linearly increased in conjunction with amount of sparkover time, as depicted in Figure

2.15. A report by Webb et al. [59] stated that although C_2F_6 is a potent greenhouse gas, CF_3I reformation is almost double the speed of that of production of C_2F_6.

Although many gaseous by-products of CF_3I have been reported, it is solid by-products that raise interest among researchers and one particular solid by-product is iodine (I_2). These findings have been reported in [40], [47], [41], [55], [57], [60], [42], [43], [61] and [62]. To offer a better understanding of how by-products of CF_3I can affect insulation performance, Takeda et al. [57] carried out extensive works through research.

Three (3) different test conditions were investigated:

i. clear electrode with fresh CF_3I, namely "condition A",

ii. used electrode with fresh CF_3I, namely "condition B", and

iii. used electrode with used CF_3I, namely "condition C"

The findings are summarized in Figure 2.16.

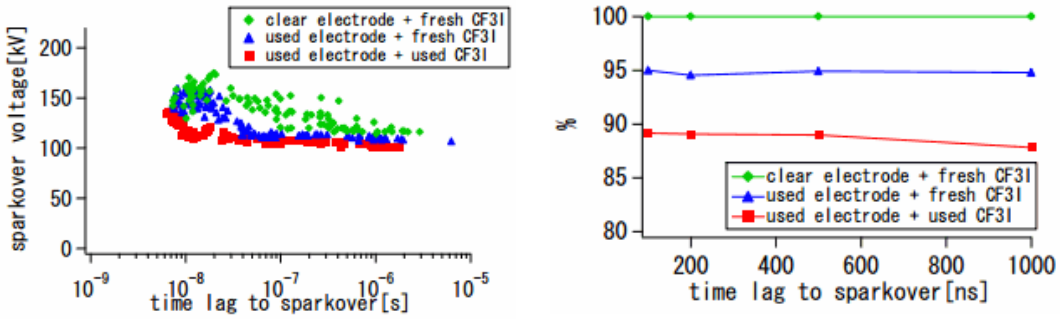

(a) **(b)**

Figure 2.16: Effects of by-products and deteriorated CF_3I on insulation performance [57]

Based on Figure 2.16, it is clear that the *V-t* characteristic for condition A > that for condition B > that for condition C, and the by-products of CF_3I affected insulation performance by more than 10%. To determine which by-products play the biggest role,

further tests carried out by Takeda showed that, although more than 1400 times the sparkover occurred in uniform gap electrode configurations; there is less than 150 ppm (0.014%) of C_2F_6 density detected in the by-products. Hence, it is assumed that deterioration in insulation performance of CF_3I gas is mainly due to the deposition of iodine on the electrode. For this reason, it is suggested that only 30% of CF_3I is used in any of the mixtures.

2.8 Reducing the By-Products of CF_3I

Because of the effects on insulation performance of CF_3I, many works have been carried out to reduce the amount of iodine after each electrical discharge. To reduce the iodine density generated by CF_3I upon a current interruption, Kasuya et al. [42] and Katagiri et al. [43] used an adsorbent to try to adsorb the iodine, which Kasuya claimed to be an activated carbon (C2X). The amount of adsorbent is increased gradually to track the effects, and the current interruptions are carried out repeatedly to see whether the adsorbent can maintain the adsorption effect. The results are shown in Figure 2.17.

By increasing the amount of adsorbent, the iodine can be removed almost completely. However, the capability of adsorbent was weakened gradually with an increasing number of interruptions. It is due to the fact that the iodine density increases when the interruption frequency increases that this occurs. Hence, by increasing the adsorbent amount, the iodine adsorption capability is increased and the iodine cannot be detected at all, even after 22 interruptions.

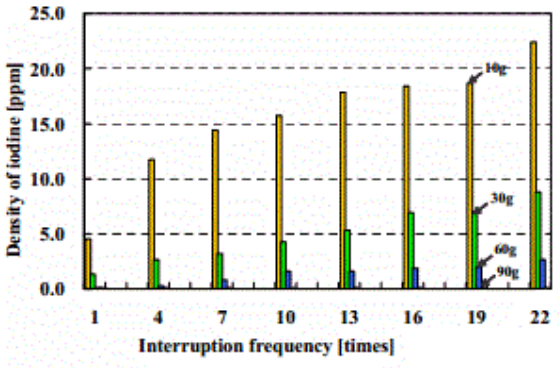

Figure 2.17: Iodine adsorption [42]

Katagiri et al. [43] also examined the effects of absorbing time on the density of iodine. Two measurements were made by Katagiri of the iodine density after a particular interruption (i.e. shortly after a current interruption and then 5 minutes later). The results showed that, after a certain amount of time, the iodine density became lower, which is helped by the effect of adsorbent, as shown in Figure 2.18.

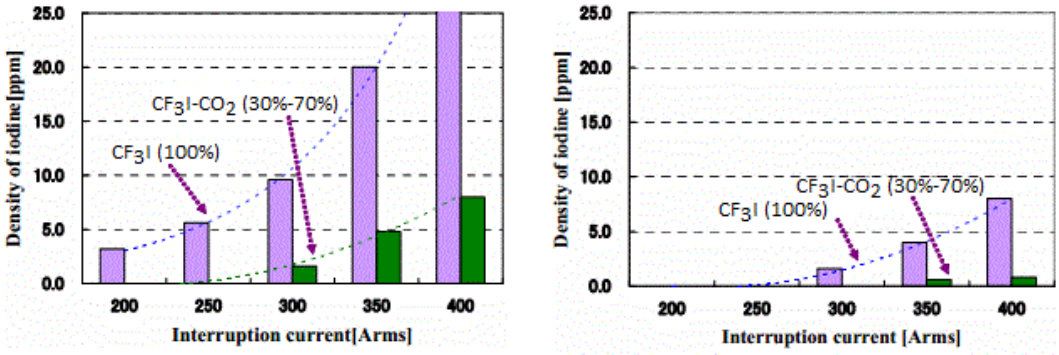

(a) **(b)**

Figure 2.18: Iodine density (a) shortly and (b) five minutes after an interruption [43]

Further research on iodine absorption revealed several methods for iodine trapping that were evaluated in 2004 by Burger and Scheele [63]. This report reviewed several iodine trapping technologies in order to identify the best system to remove

radioiodine from gas mixtures during nuclear fuel reprocessing. Burger and Scheele [63] divided various technologies into two possible groups, liquid scrubbers and solid absorbers. For the removal of iodine from CF_3I gas mixtures, however, it is not possible to use any liquid methods. Therefore, only the latter groups were listed here:

i. The Handford PUREX (Plutonium-Uranium Extraction) silver reactor – adopted to retain the radioactive iodine for long periods,

ii. Organic solids – macroreticular resins can be adopted to absorb iodine, thanks to the high affinity for iodine,

iii. Carbon filters – this method is widely adopted in nuclear reactor applications for low iodine concentrations,

iv. Silver-containing sorbents – three solids can be adopted, namely silver mordenite (AgZ), silver faujasite (AgX) and the European-developed amorphous silica with silver nitrate (AgSi)

2.9 Toxicity of CF_3I and Its By-Products

It is important to review the toxicity of CF_3I gas. In 2004, the committee on toxicology of the National Research Council (NRC) published an important review about the toxicity of CF_3I [27]. However, the NRC report was issued with the hypothesis of CF_3I as a fire extinguisher. The review was concluded as follows:

"Overall, the toxicity of CF_3I is low. The effect of CF_3I on mutagenicity and reproductive parameters is equivocal and may warrant further investigation. Human exposure to CF_3I could occur during the manufacturing, transportation, storage, or packaging processes. Accidental releases are also potential sources of exposure" [27].

More details on the information of safety issues has been taken from [64] for each of the available by-products of CF_3I, in comparison to CF_3I itself, as well as CO_2 and SF_6. Table 2.7 shows the summary of the information.

According to Table 2.7, the only gas that needs attention is C_3F_6, also known as hexafluoropropene. According to the material safety data sheet (MSDS), C_3F_6 is toxic if inhaled, and it is recommended that any person handling it uses a complete body protection suit. However, the amount produced is miniscule, as one sparkover in CF_3I produces only 0.00122 ppm under a uniform electric field and 0.000501 ppm under a non-uniform electric field [57]. According to Kamarol et al. [58], the dominant gas by-products of CF_3I is C_2F_6 and although C_3F_6 was also detected, the amount was extremely small.

Table 2.7: Toxicity review of SF_6, CO_2, CF_3I and by-products of CF_3I [65]**,** [66]**,** [67]**,** [68]**,** [69]**,** [70]**,** [71] **and** [72]

Gas/ gaseous by-products	**CAS-No.**	**EC-No.**	**Hazard statement**	**Precautionary statement**	**Potential health effects**	**Personal protection**
SF_6	2551-62-4	219-854-2	Contain gas under pressure May explode if heated	Protect from sunlight Store in a well ventilated place	May be harmful if inhaled. May cause respiratory tract irritation May be harmful if swallowed May be harmful if absorbed through skin. May cause skin irritation May cause eye irritation	Safety goggles Gloves Impervious clothing
CO_2	124-38-9	204-696-9	Contain gas under pressure May explode if heated	Protect from sunlight Store in a well ventilated place	May be harmful if inhaled. May cause respiratory tract irritation May be harmful if swallowed May cause severe frostbite. May be harmful if absorbed through skin. May cause skin irritation May cause eye irritation Act as simple asphyxiate by displacing air	Safety goggles Gloves Impervious clothing
CF_3I	2314-97-8	219-014-5	Suspected causing genetic defects	Use personal protective equipment as required	May be harmful if inhaled. May cause respiratory tract irritation May be harmful if swallowed May be harmful if absorbed through skin. May cause skin irritation May cause eye irritation	Safety goggles Gloves Impervious clothing
C_2F_6	76-16-4	N/A	Contain gas under pressure May explode if heated	Protect from sunlight Store in a well ventilated place	May be harmful if inhaled. May cause respiratory tract irritation May be harmful if swallowed May be harmful if absorbed through skin. May cause skin irritation May cause eye irritation	Safety goggles Gloves Impervious clothing
CHF_3	75-46-7	N/A	Contain gas under pressure May explode if heated	Protect from sunlight Store in a well ventilated place	May be harmful if inhaled. May cause respiratory tract irritation May be harmful if swallowed May be harmful if absorbed through skin. May cause skin irritation May cause eye irritation	Safety goggles Gloves Impervious clothing

Table 2.7 continued

Gas/ gaseous by-products	CAS-No.	EC-No.	Hazard statement	Precautionary statement	Potential health effects	Personal protection
C_3F_6	115-15-4	204-127-4	Contain gas under pressure May explode if heated Harmful if inhaled	Avoid breathing gas Protect from sunlight Store in a well ventilated place	Toxic if inhaled. Causes respiratory tract irritation May be harmful if swallowed May be harmful if absorbed through skin. May cause skin irritation May cause eye irritation	Safety goggles Face shield Gloves Complete suit protection against chemicals
C_2F_5I	354-64-3	206-566-7	Contain gas under pressure May explode if heated Causes skin irritation Causes serious eye irritation May cause respiratory irritation	Avoid breathing dust/ fume/ gas/ mist/ vapours/ spray If in eyes: Rinse cautiously with water for several minutes. Remove contact lenses, if present and easy to do. Continue rinsing Protect from sunlight Store in a well ventilated place	May be harmful if inhaled. Causes respiratory tract irritation May be harmful if swallowed May be harmful if absorbed through skin. Cause skin irritation Causes serious eye irritation	Safety goggles Gloves Impervious clothing

2.10 Conclusion

In this chapter, an extensive review on the critical insulation factors of CF_3I and its mixtures have been presented. CF_3I provides good dielectric strength properties as well as environmentally friendly characteristics which make it the most suitable gas to date to replace SF_6 as a gas insulating medium.

Although CF_3I cannot be used alone, due to its high boiling point, mixing it with other gases provides researchers areas for further investigation. The possibility of CF_3I mixtures being used in high voltage equipment requires further studies. Air, N_2, and CO_2 have been used as possible mixtures with CF_3I. Of all the gases, CO_2 emerges as the better pair for CF_3I if the mixture were to replace SF_6, as it has been shown by previous investigations [40], [44], [41].

It has been shown that pure CF_3I provides better insulation performance than that of SF_6. However, mixing it with other gases will decrease the insulation characteristics, but performance will remain at appreciable levels. Based on previous works, CF_3I-CO_2 mixtures with a ratio of 70% of CO_2 and 30% of CF_3I have been chosen as the main substance to be investigated in this study. The choosing of CF_3I content in these mixtures is a trade-off between the following factors:

i. *Boiling point*: CF_3I content has to be low so that to reduce the boiling point of the mixtures;

ii. *Insulation performance*: CF_3I content has to be high to provide better insulation properties; and

iii. *By-products*: CF_3I content has to be low to reduce the amount of by-products, of which will affect its insulation performance.

CHAPTER 3: PURPOSE-BUILT TEST RIG: DESIGN PRINCIPLES AND CONSTRUCTION DETAILS

3.1 Introduction

In order to characterise the breakdown characteristics of CF_3I gas and its gas mixtures, a reliable pressurized vessel which is suitable for high voltage applications and able to withstand high pressure, was required. Furthermore, various measurement and control apparatus need to be built-in into the test system together with the gas handling and recycling systems. This chapter will explain in detail the building of a pressure vessel for this application. A test rig for carrying out experimental works on insulation gas will be explained.

3.2 Design of the Pressure Vessel

3.2.1 Structure

Figure 3.1 shows the initial drawing for the desired structure. The vessel is 500 mm high with a radius of 250 mm, giving the volume of the vessel around 0.0982 m^3, or 98.2 litres. The thickness of the vessel is 10 mm minimum. This thickness applies everywhere; on top, bottom, and also the side walls. This limited volume is to reduce the amount of gas required for each test.

At the top of the vessel, there is a window to place a high voltage bushing. The conductor in the bushing is then connected to a high voltage source. The side window is required in order to view every process which will be happening in the vessel while the CF_3I gas mixtures are being tested. This window will also help the researcher to adjust

and verify the gap between the high voltage electrode and the ground electrode for a given test. O-rings are used to prevent any leakage at every point which has bolts and nuts. There are three o-rings, located at the top and side window with another one at the bushing.

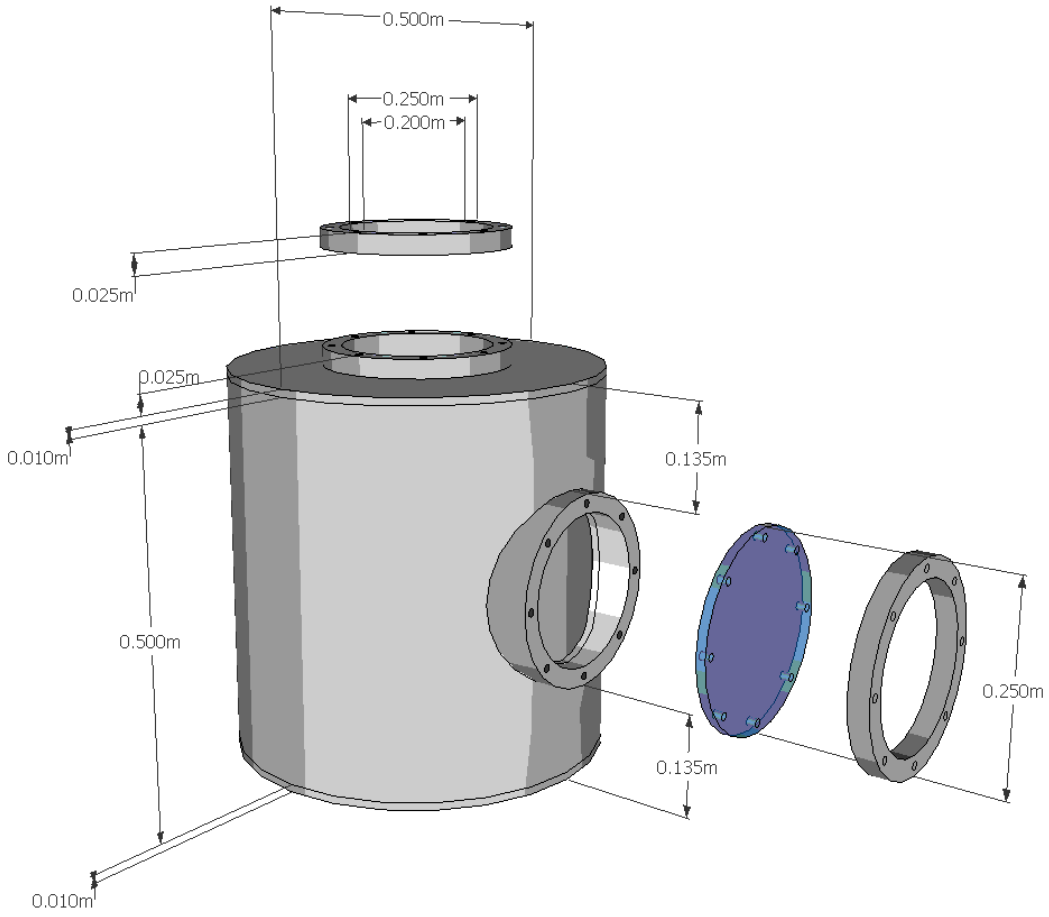

Figure 3.1: Pressure vessel

The bottom view of the vessel is shown in Figure 3.2. There are 12 small holes altogether, six on each side. Referring to Figure 3.2, and working from left to right, the dimensions of the holes at the top side are 13.2 mm, 13.2 mm, 26.4 mm, 21 mm, 21 mm, and 21 mm. These dimensions are the same for the holes at the bottom side. These holes are required for fittings and assemblies, which include an inlet hose, outlet hose, cables for measurements, gauges, and other related equipment.

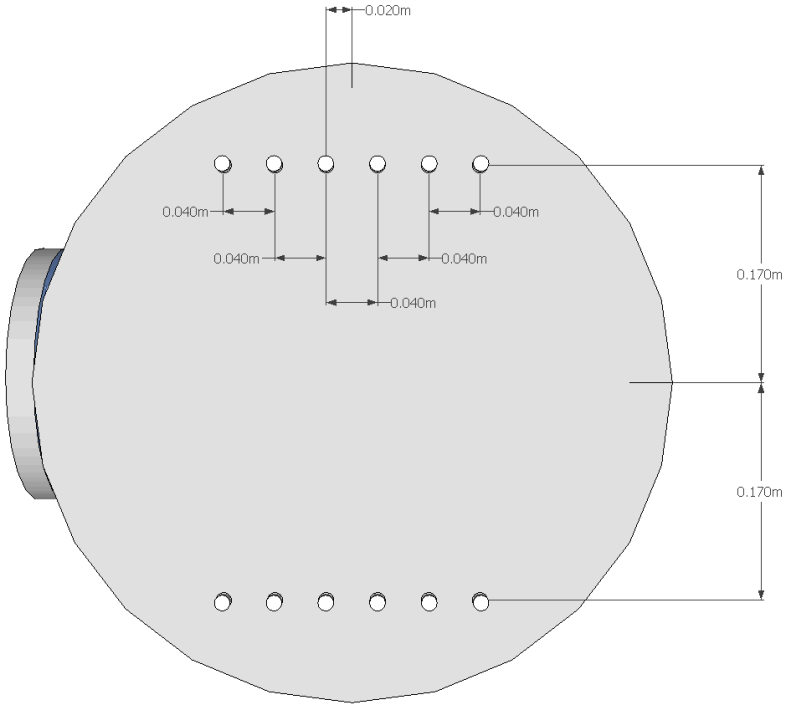

Figure 3.2: Bottom view of the pressure vessel

As shown in Figure 3.3, the vessel is welded with four steel-angled legs. The legs are joined together at the bottom with a wooden skateboard with four castors and each castor is fitted with a brake for safety reasons. The minimum height of the structure from the floor is 800 mm. This is to ensure enough clearance for all the fittings and assemblies and also a space to fix CF_3I gas cylinders.

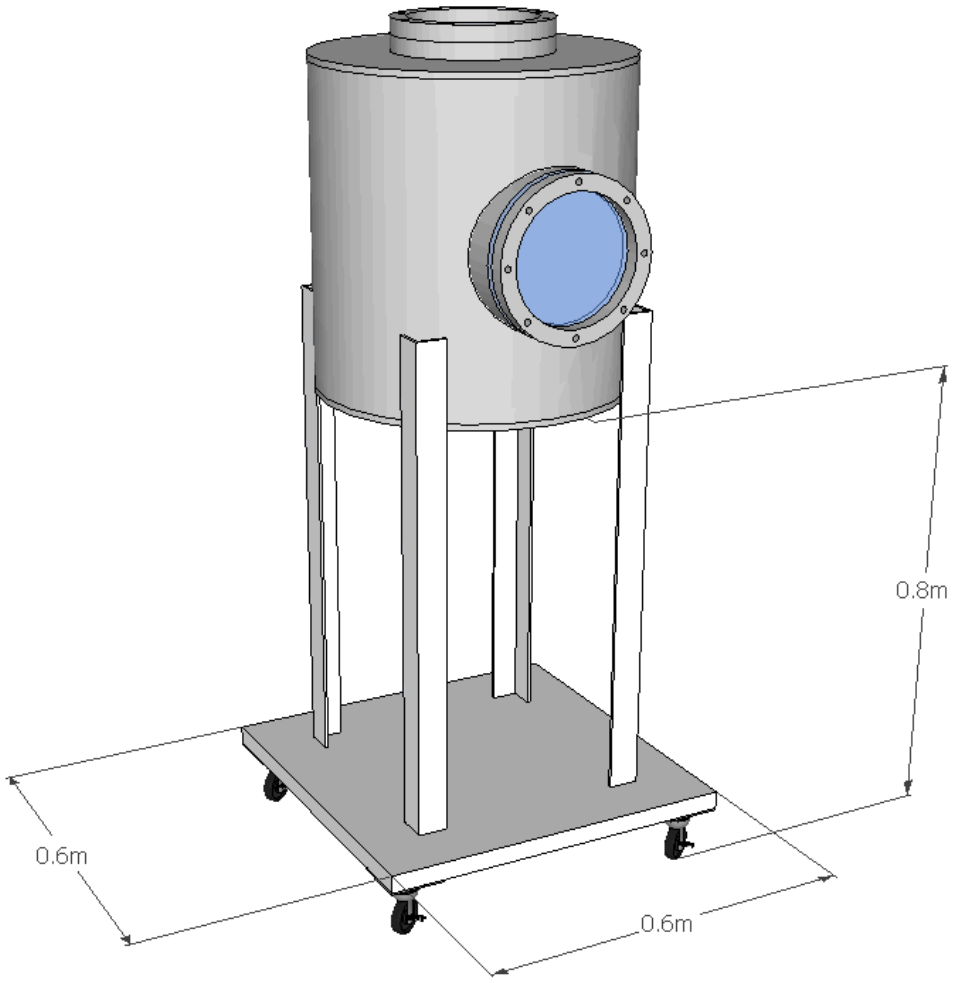

Figure 3.3: Structure with legs

3.2.2 Materials

For the structure to be able to withstand a specific high pressure and continuously be subjected to high voltage stresses, the materials shall be of industrial standard. For this reason, and after consulting with a manufacturer, mild steel grade S355J2G3, is chosen as the material for the structure. The symbol and properties of the material are shown in Table 3.1.

Table 3.1: Symbols used in EN 10025-2: 2004: Non-alloy structural steel [73]

Symbol	Example	Property designated
S	**S**185	Structural steel
E	**E**295	Engineering steel
360	E**360**	Minimum yield strength (R_{eH}) in MPa and 16mm
JR	S235**JR**	Longitudinal Charpy V-notch impacts 27 J at +20 ºC
J0	S275**J0**	Longitudinal Charpy V-notch impacts 27 J at +0 ºC
J2	S355**J2**	Longitudinal Charpy V-notch impacts 27 J at –20 ºC
K2	S355**K2**	Longitudinal Charpy V-notch impacts 40 J at –20 ºC
+AR	S235JR+**AR**	Supply condition as rolled
+N	S275J0+**N**	Supply condition normalized or normalized rolled
Customer options		
C	S235**C**	Grade suitable for cold forming

The side window is made of polycarbonate, a type of thermoplastic which is very tough and that is used in many applications, such as headlamps and tail lights in automotive, bottles and containers in packaging, and housing for mobile phones computers and fax machines in electrical and electronics [74]. The main advantages over other types of plastics are super strength and being very lightweight. More importantly, due to its high transparency level, polycarbonate transmits light well, although there is a known cut-off wavelengths, where polycarbonate is understood to block UV wavelengths below 386-390 nm [75]. Polycarbonate is also able to maintain the necessary properties over a wide range of temperatures, ranging from –20 ºC to 140 ºC [76]. The thickness of the polycarbonate used for the window is 30 mm. This is to ensure that it can withstand a pressure of at least 5 bars (abs) without undergoing any deformation. Although it seems quite thick, the visibility inside the vessel is very clear. Face type o-rings which are made of rubber are used as leakage prevention measures along the side of the window with a groove depth of 4.6 mm and groove width of 7.7 mm.

The pressure vessel has been tested and inspected by Pipaway Engineering Ltd. The test has been completed using calibrated test equipment traceable to national standards including:

i. Digital Pressure Gauge LE02-1-30 bar Serial No: 28942

The vessel is tested using dry nitrogen at 10 bars and held for 30 minutes. All welds are checked using PH Gas Leak Detector spray. No pressure drop is recorded and no leak is located.

Figure 3.4: Pressure vessel

3.3 Electrodes

There are eight different geometries which are available for the tests; rod-plane, sphere-plane, plane-plane electrode systems, as can be seen in the Figure 3.5. The rod type has a 45º angle and the tip has a radius of 0.5 mm. There are electrodes with radii of 6 mm, 12 mm, 24 mm, and 48 mm. A sphere electrode with a radius of 25 mm is

available, along with a plane electrode with a radius of 45 mm. Each electrode has an M10 size thread which is required to be fitted to the bushing through an M10 rod.

All the high voltage electrodes that are connected to the bushing will be stationary. Ground electrodes on the other hand, will be vertically moveable so that a desired gap length can be achieved between the ground electrode and the high voltage electrode. This is made possible by using a linear actuator described in the next section.

The electrodes are made from brass which is an alloy made from copper (Cu) and zinc (Zn). Lead (Pb) is also often added in concentrations of up to 3% to provide free-machining properties [77]. Brass is categorized as a non-sparking metal [78]; This is important so that no spark will be produced in a hazardous environment.

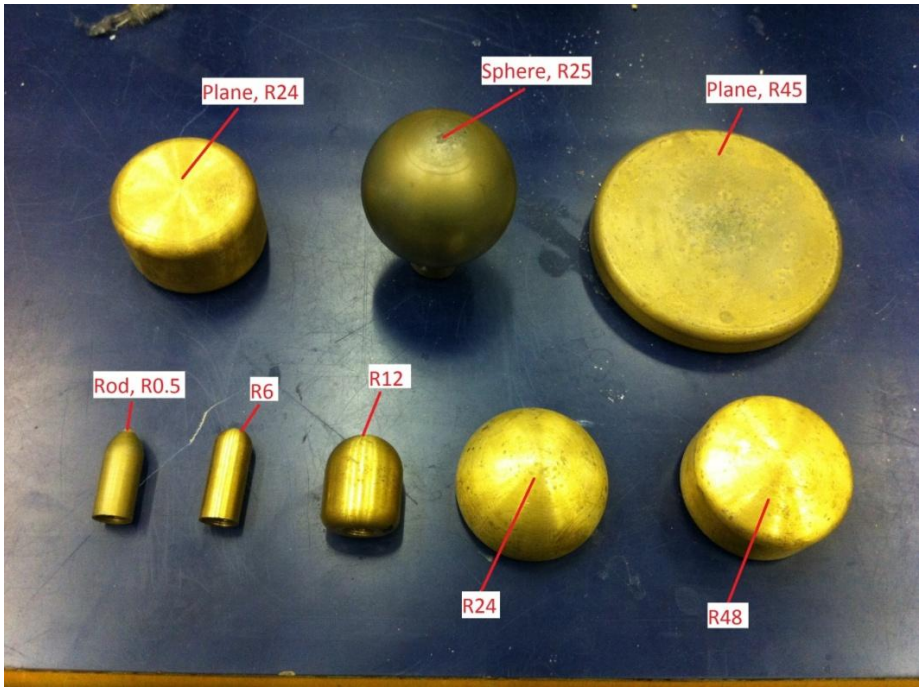

Figure 3.5: Electrodes (radius in mm)

3.4 Linear Actuator

For this research, a variable gap length system between high voltage electrodes and ground electrodes is preferred. With this system available, effects of gap lengths can be examined while maintaining other tests parameters, such as gas mixtures, gas pressures and electrode configuration.

Two major issues in designing such a system are that it will be placed in a pressurized vessel and it must be controlled from outside while the vessel is under pressure (without having to remove the gas prior to varying the gap). In this investigation, this is achieved by using a linear actuator.

3.4.1 Linear Actuator Main Unit

A linear actuator is an actuator which creates linear motion in any direction. The actuator used in this project is the Firgelli Linear Actuator L12-10-100-06-R, as shown in Figure 3.6. Figure 3.7 shows the dimensions of the actuator.

When power to the actuator is removed, the actuator stops moving and holds its position up to a load of backdrive force, namely 80 N. If the load exceeds the backdrive force, the actuator will then backdrive. According to the manufacturer, stalling the actuator while it is under power for a short period of time (several seconds) will not damage the actuator, albeit the actuator will draw a small amount of current which, in this case, is 450 mA.

Figure 3.6: Firgelli linear actuator [79]

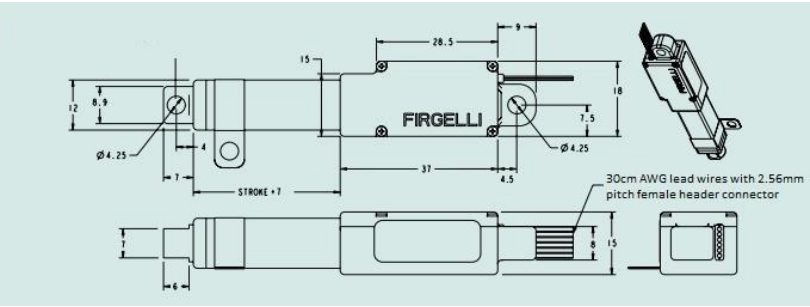

Figure 3.7: Firgelli linear actuator dimensions (in mm) [79]

3.4.2 Linear Actuator Controller

To make sure the actuator moves the ground electrode and stops at the exact gap length prior to any tests, a controller with a feedback loop is needed. For this reason, a controller made by Phidgets is used to control the speed, acceleration and position of the linear actuator. The controller is powered by a universal serial bus (USB) port of a laptop or PC. Figure 3.8 shows a picture of the controller.

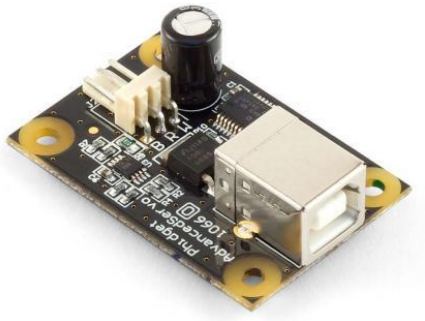

Figure 3.8: Liner actuator controller – PhidgetAdvancedServo 1-Motor [80]

3.5 Fittings and Assemblies

As mentioned in section 3.2.1, there are 12 holes of different sizes to accommodate several fittings and assemblies which have to be included. This section will explain all the necessary equipment fittings.

3.5.1 Gauges

Two types of gauges are used in this experimental setup for measuring pressure of less than 1 bar (abs) and for measuring positive pressures (i.e. more than 1 bar (abs)). To make pressure measurements more accurate, a –1 to +1 bar gauge is used so that there is continuity between a vacuum state and a pressurised state. Figure 3.9 below shows the described gauges. Each is 100 mm in diameter with 16.7 mm bottom entry.

Figure 3.9: Two types of gauges

3.5.2 Hose, Valves and Hose Tails

In order to connect gas cylinders to the vessel, a good quality hose is needed so that whenever the vessel is under a vacuum, the hoses will not collapse. A quality hose will ensure there will be no leakage of gas anywhere along the hose. For this reason, a

3/8” Toyo vacuum hose is used along with 3/8” ball valves and 3/8” hose tails. The ball valves will ensure the pressurised state (whether it is in a vacuum or positive pressure) will be locked properly and that the hose tails are needed to connect the hose to the ball valves.

3.5.3 Pressure Relief Valve

As a safety measure, a pressure relief valve is fitted at the bottom of the vessel and it is set at 6 bar (abs). This is very important as the valve will provide an auxiliary passage should the pressure inside the vessel exceed a predetermined pressure, currently set at 6 bars (abs). The pressure relief valve is calibrated using two types of equipment and is traceable to the T.J. Williams Calibration Certificate TJ48/10:

i. Pressure Booster Pneumax Model Px 1740.50n

ii. Pressure Gauge 0-14 bar

Firstly, the unit (pressure relief valve) is applied with pressure using pressure booster. Next, it is set to relieve at 6 bars (abs) and locked. Figure 3.10 below shows the pressure relief valve described above.

Figure 3.10: Pressure relief valve

3.6 Bushing

According to [81], a bushing is "an insulating structure, including a through conductor or providing a central passage for such a conductor, with provision for mounting on a barrier, conducting or otherwise, for the purpose of insulating the conductor from the barrier and conducting current from one side of the barrier to the other". Hence, a bushing is needed so that lightning impulse can be passed through to an electrode inside the vessel without the risk of flashover to the earthed vessel metal structure.

The high voltage bushing used in this project is rated at 38 kV. The bushing conductor is made from copper and it is bonded to a silicone rubber jacket as an outside housing insulator. Table 3.2: Bushing specifications is shown below.

Table 3.2: Bushing specifications [82]

Routine Tests: BS EN 60137 : 1996	
AC Dry Power Frequency	70 kV 1 minute
Partial Discharge	< 10 pC @ 24.5 kV
SF_6 Gas Tightness	No leaks
DC Resistance @ 1000 V	> 250 MΩ

Figure 3.11 below shows the bushing used in the experimental setup. According to [82], for a 38 kV rated bushing with dry power frequency withstand voltage of 70 kV, its dry lightning impulse withstand voltage (BIL) is limited to 170 kV peak.

Figure 3.11: Bushing

3.7 Temperature and Humidity Sensor

It is essential to record the humidity and temperature for every measurement so corrections can be made based on a correction factor as stated in *BS EN 60060-1:2010 – High voltage test techniques*. Since the CF_3I gas mixture is contained in a pressurised vessel, a wireless temperature and humidity sensor is desirable. For this reason, a set of devices manufactured by Oregon Scientific, which can provide such functionality, were used. These consist of a main unit (BAR208HGA) and a remote unit (THGR122NR). Both units have temperature and humidity sensors built in. The remote unit is placed inside the vessel and is designed to transmit readings to the main unit, which has a screen to display the temperature and humidity for both inside and outside the vessel. Table 3.3 summarises the main technical specifications of both humidity and temperature sensors. Figure 3.12 below shows both units.

Table 3.3: Humidity and temperature sensor specifications [83]

Type	Description
Main unit (BAR208HGA)	
L × W × H	182.5 × 94 × 51 mm
Weight	241 g without battery
Temperature range	–5ºC to 50ºC
Resolution	0.1ºC
Signal frequency	433 MHz
Humidity range	25% – 95%
Humidity resolution	1%
Power	3 × UM-3 (AA) 1.5 V batteries
Remote unit (THGR122NR)	
L × W × H	92 × 60 × 20 mm
Weight	63 g without battery
Transmission range	30 m unobstructed
Temperature range	–20ºC to 60ºC
Power	2 × UM-4 (AAA) 1.5 V batteries

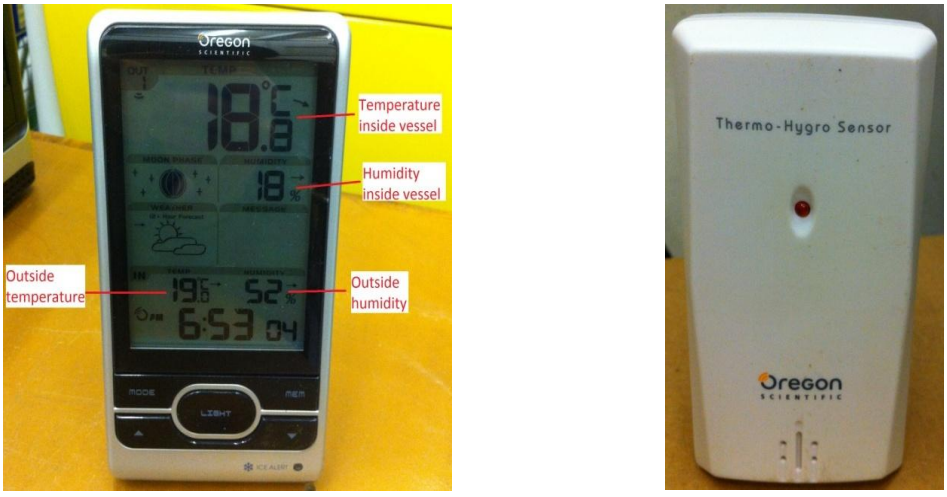

Figure 3.12: Temperature and humidity sensor – main unit and remote unit

3.8 Compression Seal Fitting

A compression seal fitting, which is also known as a sealing gland, is needed at one of the holes at the bottom of the vessel. This is used to seal wires that pass through

the pressurised gas inside the vessel to the outside. By using a sealing gland, there will be no gas leakage along the wires, while making the wires stationary because of the difference in pressure. The wires are needed to control the linear actuator.

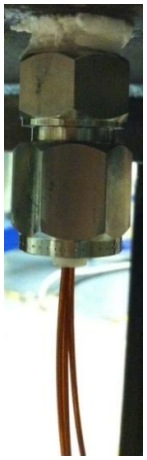

Figure 3.13: Sealing gland

In this experimental setup, an insulated conductor sealing gland made by Thermal Detection Ltd. was being used. Table 3.4 shows the exact specifications for the sealing gland.

Table 3.4: Sealing gland specifications

Product code	PL-18-A3-T-0.4/0.2M
Conductors	Three 18 AWG (1.02mm), Kapton® insulated solid copper conductors with a total length of 600mm
Electrical rating	13A at 600V AC or 850V DC per conductor
Gland body material	In 316 stainless steel
Cap nut and follower material	In 303 stainless steel
Process connection	½" BSP taper
Sealant	Teflon®
Temperature range	–185ºC to +232ºC
Pressure range at 20ºC	Vacuum to 345 bar

3.9 Regulators and Heater

In order to fill the pressure vessel with gas, a pressure regulator is needed. It is fitted at the outlet of a gas cylinder or a high pressure pipeline. The regulator is used to reduce the pressure of the gas inside the cylinder to a lower pressure set by the user. Figure 3.14 and Figure 3.15 show the pressure regulators for compressed air and CO_2 respectively.

Figure 3.14: Compressed air pressure regulator

Figure 3.15: CO_2 pressure regulator

When CO_2 passes through the outlet valve from the gas cylinder, the gas typically expands. During this process, the temperature of CO_2 will drop suddenly and the gas will become significantly cooler. This may cause the moisture in the CO_2 to freeze the regulator and the flow of the gas will be restricted, which may lead to blocking the system [84]. For that reason, a CO_2 heater is needed in order to eliminate this effect. The heater warms CO_2 gas to approximately 174 ºF (79 ºC) [84]. The heater is connected between the output of the gas cylinder and the input of the CO_2 pressure regulator. Figure 3.16 shows the CO_2 heater used in this research.

Figure 3.16: CO_2 heater

3.10 Gas Removal System

As this project involves gas mixtures of CF_3I, every test must be as leak proof as possible, so that no gas will be released into the atmosphere. After each experiment, CF_3I gas mixtures have to be taken out and stored properly in gas cylinders. For this reason, a gas removal system is needed.

A gas removal system made by DILO Company, specifically Mini Service Cart Model No. Z579R03 is used in the experimental setup. The service cart consists of a compressor, a vacuum compressor, a vacuum pump, a pre filter and some other fittings

and assemblies as shown in Figure 3.17. Figure 3.18 shows the modules and the functions.

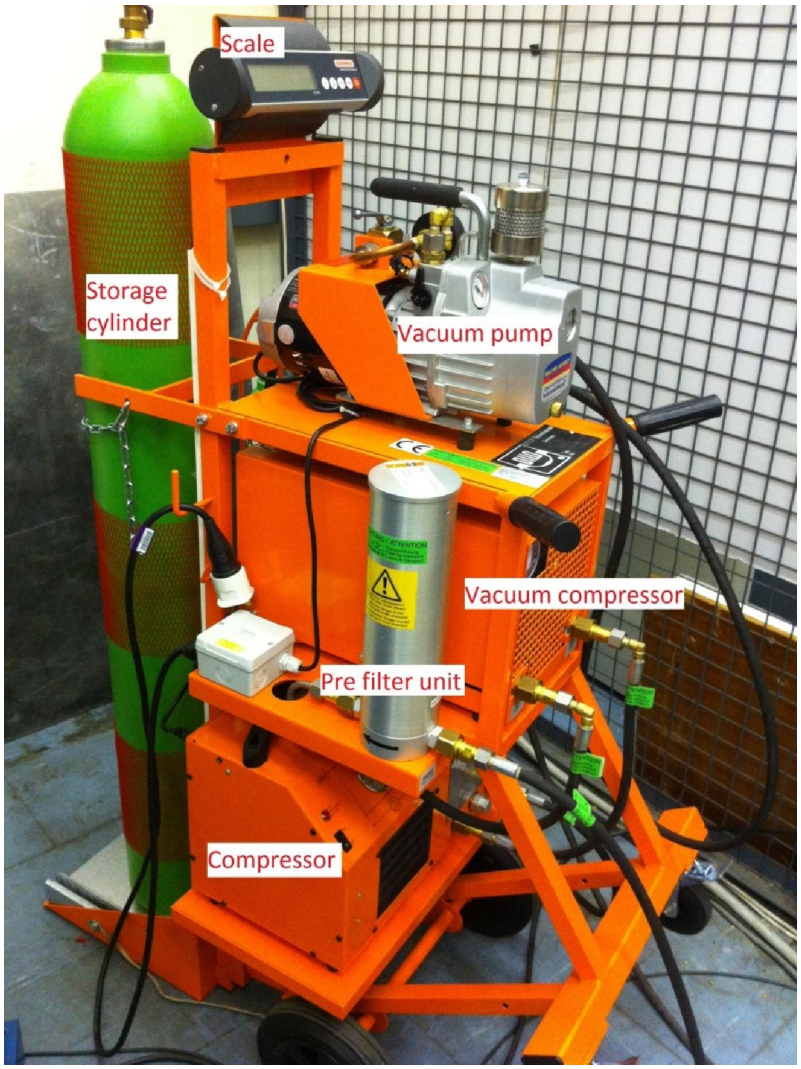

Figure 3.17: DILO gas recovery system

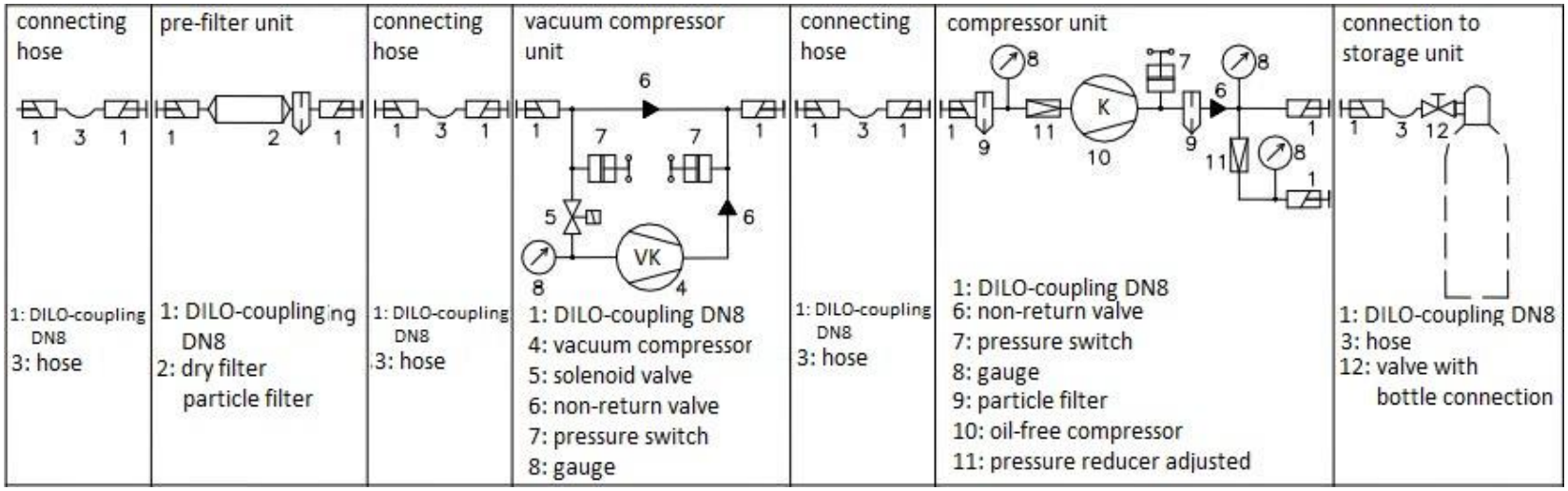

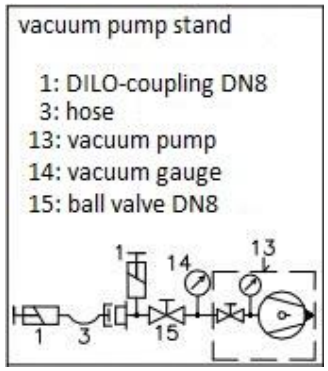

Figure 3.18: DILO modules and function [85]

The DILO unit acts as a recovery system for CF_3I gas mixtures. In recovering CF_3I gas, there are three main units that the CF_3I will pass through before being kept in a storage cylinder, these include the pre-filter unit, the vacuum compressor unit, and the compressor unit.

At the pre-filter unit, a dry filter cartridge absorbs moisture and decomposition products from the gas. The unit consists of a tube filled with desiccative. There is also a particle filter that filters solid particles and solid decomposition products out of the gas. This will ensure the gas is purified and dried during the recovery process.

The vacuum compressor unit allows the recovery of the gas down to less than 50 mbar. The compressor is the dry-running type which operates entirely without oil. The delivery rate is 1.3 m^3/hour, and the unit is capable of achieving a final vacuum of less than 10 mbar.

The compressor unit is also a dry-running type. The maximum suction overpressure is 10 bar and is controlled by a pressure switch. With a delivery rate of 1.0 m^3/hour, the unit is capable of giving a final pressure of up to 50 bar maximum.

To remove air from the pressure vessel, only a vacuum pump unit will be used. The suction capacity of this vacuum pump is 10 m^3/hour, and the final pressure that can be achieved is less than 1 mbar.

3.11 Gas Evacuation and Filling System

Figure 3.19 shows the test rig which has been deployed as a gas evacuation and filling system. Prior to any tests, there will be some air inside the test chamber. All valves, namely V_1, V_2, V_3, V_4, V_5, V_6, V_7, and V_8 are initially kept at the closed position. The vacuum pump is turned on and V_1, V_2, V_3, and V_4 are turned to the open position. This will ensure that all gas inside the pressure vessel will be evacuated. The

evacuation process will take at least 1 hour in order to ensure the pressure vessel is vacuumed properly and all water vapour in the vessel and hose has been fully evacuated. At the end of the evacuation process, V_1, V_2, V_3, and V_4 are closed and the reading on the pressure gauge will be at 0 bar (abs).

To fill the CF_3I-CO_2 gas mixture, the V_5 valve is first turned to the open position. The partial pressure of CF_3I is set to the desired value, e.g. 0.30 bar (abs), and V_1 valve is then opened. When the pressure gauge is showing 0.30 bar (abs), V_1 and V_5 valves are turned to the closed position. Next, V_6 is opened and the partial pressure of CO_2 is set, such as at 0.70 bar (abs), and V_2 is then turned to the open position. At the end of the filling process, the reading shown by the pressure gauge will be at 1.0 bar (abs) and V_2 and V_6 are then turned to the closed position. The gas mixture will be left for at least 24 hours before any tests are carried out to ensure the gases are properly mixed together, as recommended by Ohtsuka et al [86]. This technique has been investigated and it is found that the results were repeatable beyond 24 hours.

As for the CF_3I-CO_2 recovery process, V_3, V_7, and V_8 valves are turned to the open position. The DILO recovery system is then turned on. The recovery process will take approximately 2 – 3 hours, depending on the pressure of the gas mixture. At the end of the recovery process, V_3, V_7, and V_8 valves are returned to the closed position. At this time, the pressure gauge will show a 0 bar (abs) reading.

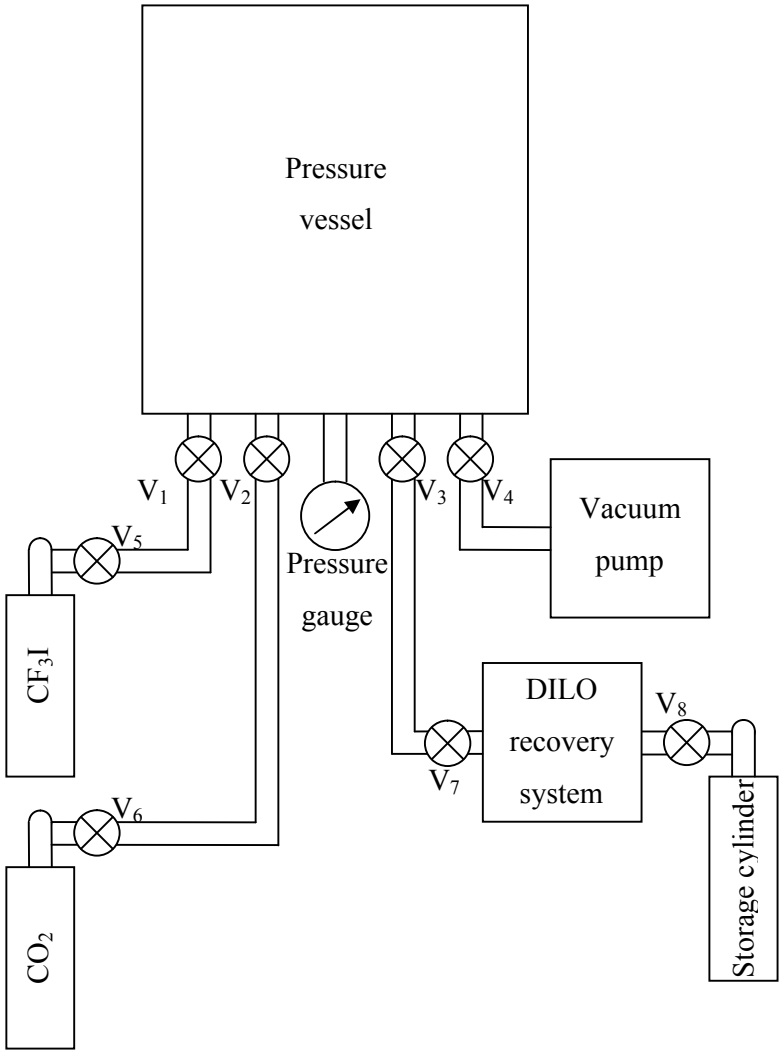

Figure 3.19: Gas evacuation and filling system

3.12 Generation and Measurement of a Lightning Impulse

It is essential to generate and measure the recommended shape of lightning impulse to be used in this project so that it will conform to the standard as stated in [45]. According to the standard, a full lightning impulse should have a front time of 1.2 μs and a time to half-value of 50 μs. It is described as a 1.2/50 impulse with a tolerance of:

Peak value	±3%
Front time	±30%
Time to half-value	±20%

3.12.1 Generation of a Lightning Impulse

A Haefely impulse generator, the SGSA 400-20 and a charging rectifier known as the LGR 100-20 are being used as the main equipment in generating a lightning impulse for this project. The non-inverting impulse generator consists of four stages, the Marx generator circuit which is capable of delivering 100 kV per stage, allows for a maximum output voltage of 400 kV. The circuit diagram of the generator is shown in Figure 3.20.

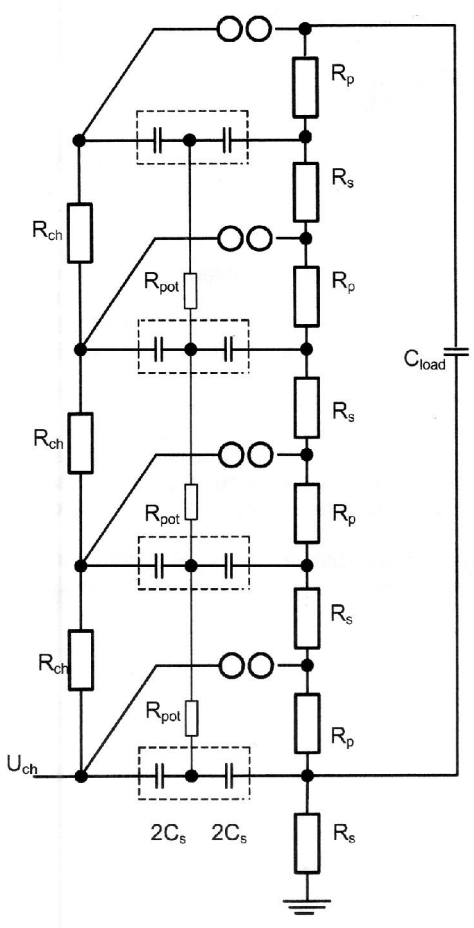

Figure 3.20: Schematic diagram of impulse generator; R_{ch} (4.7 kΩ): charging resistor; R_s (12.1 Ω): front resistor; R_p (67 Ω): tail resistor; R_{pot} (0.78 MΩ): potential resistor; C_s (2.0 µF): impulse capacitance; C_{load}=load capacitance [87]

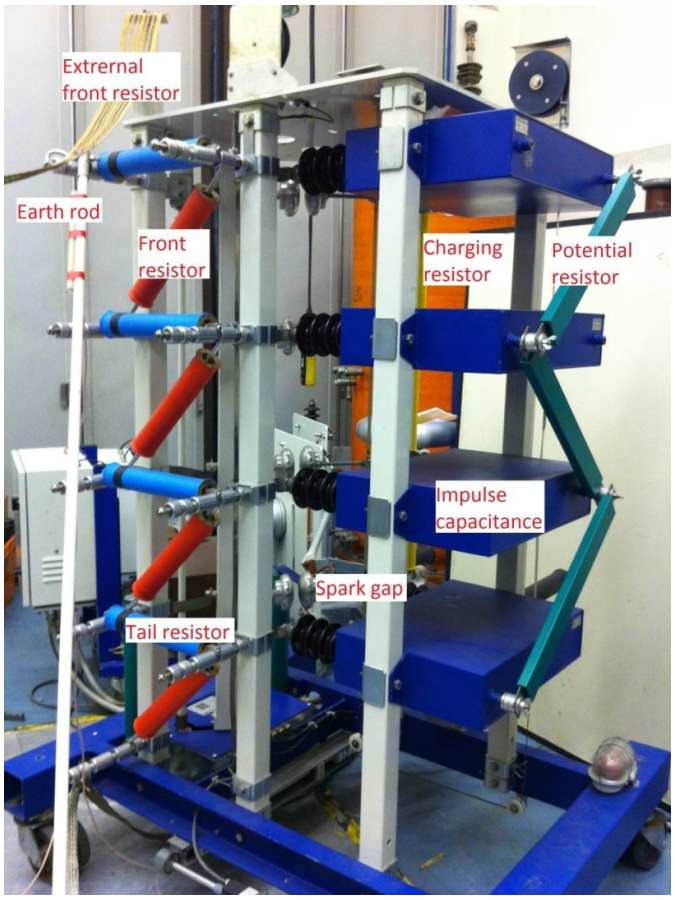

Figure 3.21: Haefely SGSA impulse generator

The charging unit is shown in Figure 3.22

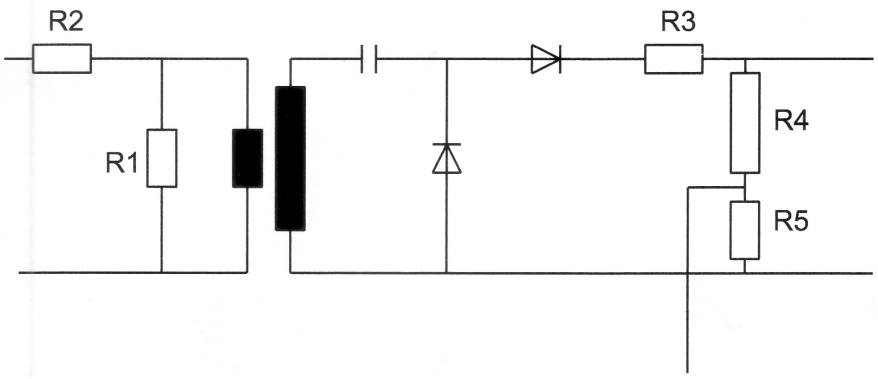

Figure 3.22: Schematic diagram for charging unit; R1 (165 Ω): Demagnisation resistor; R2 (2.7 Ω): Primary damping resistor; R3 (8.5 Ω): High voltage damping resistor; R4 (200 MΩ) and R5 (5.5 MΩ): DC measuring resistors [88]

To control the output of the lightning impulse, an impulse generator control Type GC 223 is used, as shown in Figure 3.23.

Figure 3.23: Impulse generator control unit

3.12.2 Measurement of Lightning Impulse

A capacitive voltage divider is used in this project to measure the lightning impulse with a ratio of 27931 V/V and stated response time of 49 ns as shown in Figure 3.24.

Figure 3.24: Capacitive voltage divider

3.12.3 Recording Instrument

A Lecroy Wave Jet 100MHz digital storage oscilloscope (DSO) is used in this work. The oscilloscope is able to capture high speed, single-shot impulses at a maximum sampling rate of 1 gigasample/second. Figure 3.25 shows the oscilloscope.

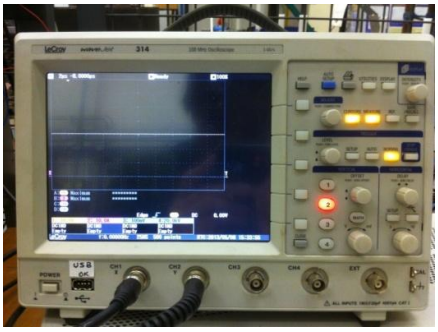

Figure 3.25: Digital storage oscilloscope

Figure 3.26 shows the complete block diagram of the test rig. An example of a standard impulse lightning 1.2/50 with a peak voltage of 50 kV is shown in Figure 3.27(a) and Figure 3.27(b) for positive and negative polarity respectively.

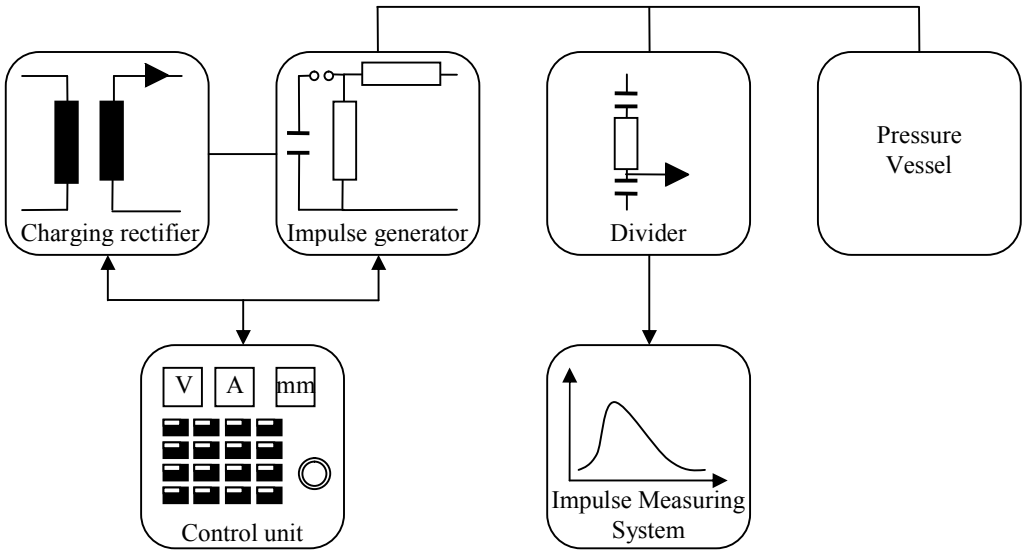

Figure 3.26: Block diagram of the test rig

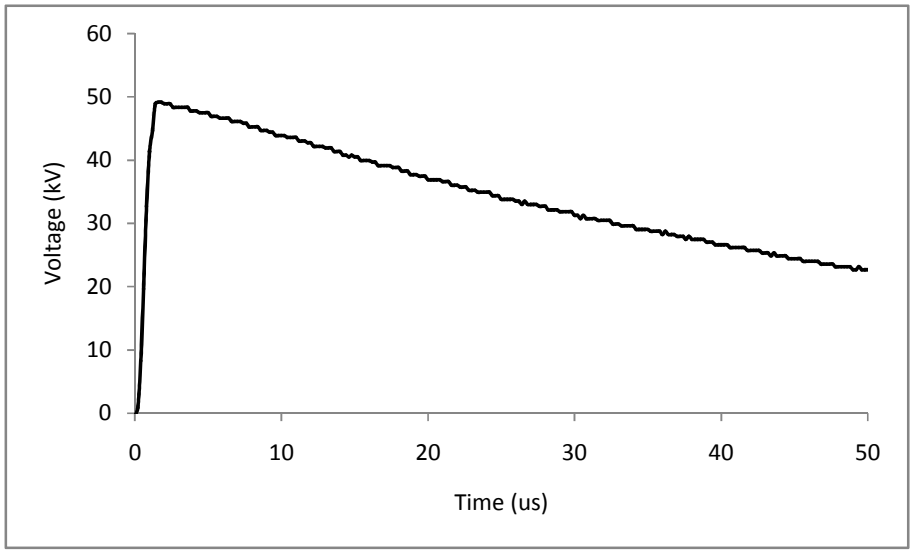

(a) positive polarity

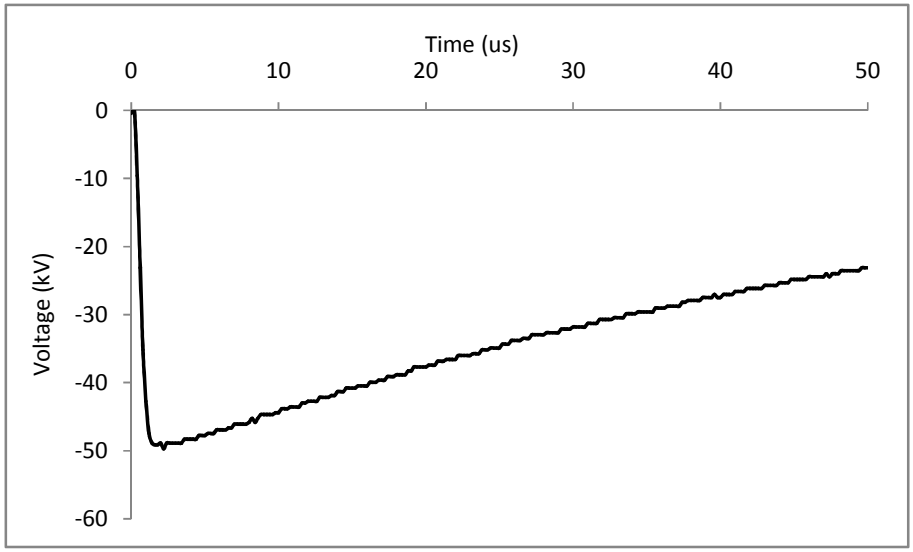

(b) negative polarity

Figure 3.27: Standard 1.2/50 lightning impulse

3.13 Conclusion

During this work, a new test rig has been developed specifically for gas research. There are five major parts in the test rig including: (i) *generation* of lightning impulse –

which includes a marx generator and charging unit; (ii) a *measurement* of lightning impulse – which includes a capacitive divider and digital storage oscilloscope; (iii) a *pressure vessel*, used as a test chamber; (iv) a *control unit* – which includes temperature and humidity sensors, pressure gauges, regulators, and electrode gap length control system; and (v) a *gas recovery* system – which includes a DILO unit and storage cylinders.

The test rig is capable of carrying out tests of up to 5 bars (abs) in pressure. An electrode gap length control system is made possible by using a sealing gland without having to remove gas from inside the test chamber, which greatly saves a lot of time. A system to record wirelessly the temperature and humidity inside the pressure vessel has also been deployed so that any atmospheric corrections can be made to ensure the results conform to the standards.

As it is important to investigate gas breakdown behaviour in various electric fields, there is a need to use different kinds of electrode configurations. For that reason, a set of brass electrodes has also been obtained. All the electrodes, the pressure vessel, and the bushing are cylindrical in shape, which allows the simulation model to make use of a 2D axis-symmetric feature, as will be discussed in the next chapter.

Although the capability of the lightning impulse generator is up to 400 kV, this study is limited to an impulse level of around 170 kV as it is the dry lightning impulse withstand voltage level of the bushing. The voltage level, however, is considered enough to be used throughout this research.

CHAPTER 4: SIMULATION MODEL AND FUNDAMENTAL MEASUREMENT TECHNIQUES ON AIR BREAKDOWN UNDER LIGHTNING IMPULSE

4.1 Introduction

The newly developed test rig that was described in Chapter 3 has to be tested in order to ensure it is fit for further tests on CF_3I mixtures. With the test chamber built from scratch, all the fittings and assemblies, such as gauges and ball valves are newly fitted. In addition, the bushing and the gap length control have been put into place and connected to the generator. It is very important that all the equipment work properly and provide accurate results.

The tests are carried out according to the international IEC standards [45]. A full lighting impulse voltage of 1.2/50 μs is applied in every test with the use of the up-and-down method, to determine the 50% breakdown voltage (U_{50}) of air in each test condition. To ensure all measurements are valid according to the standard, atmospheric corrections in dry tests have been carried out.

A technique of determining electric field is needed to understand fully the behaviour of air under certain electric field profiles. It is difficult to measure properly electric field at all locations between two electrodes. Due to the fact that the electrodes are placed under pressurized gas in a test chamber, further complexities need to be overcome. Although Cloete and van der Merwe [89] determined the electric field between two spheres by the method of images, numerical simulation techniques, as used by Slade and Taylor [90], are the preferred method. Numerical simulation techniques

using commercially available electromagnetic software provides a more practical and cost effective way to perform the measurements. This allows the user to avoid expensive and complex trial-and-error laboratory experiments which are often very difficult to carry out.

In this chapter, a finite element method is used for the computer simulation. The finite element method has been widely used in solving engineering problems, such as heat transfer, structural mechanics, fluid flow, and acoustics. Nevertheless, a thorough understanding of the mathematical approach in finite element method is not the main objective of this research. This can be studied in detail in many textbooks, such as [91], [92] and [93].

A simulation model of the test rig is developed in the computer software. Each electrode configuration has an individual model, providing a platform for further analysis with CF_3I tests. Focus is being given to the electrodes so the model is limited to electric field behaviour inside the test chamber.

4.2 Finite Element Modelling

In this study, a commercial finite element package, specifically COMSOL Multiphysics version 4.3a is used to carry out the modelling and electric field computations. In solving a particular problem, there are three stages involved, which are the pre-processing stage, solving stage, and post-processing stage. In the pre-processing stage, the fundamentals of the model are being developed and determined, such as geometrical structure, selection of materials and properties, domain and boundary conditions, and lastly meshing criteria. The solving stage, or execution stage, is carried out with a related mathematical model of differential equations, whether the study is stationary or time-dependent. Lastly, in the post-processing stage, users see the results

and generate a plot for various kinds of variables or parameters, whether it is a 1D plot, 2D plot, or 3D plot, depending on the model. Figure 4.1 shows the FEM flowchart and the process involved in each stage.

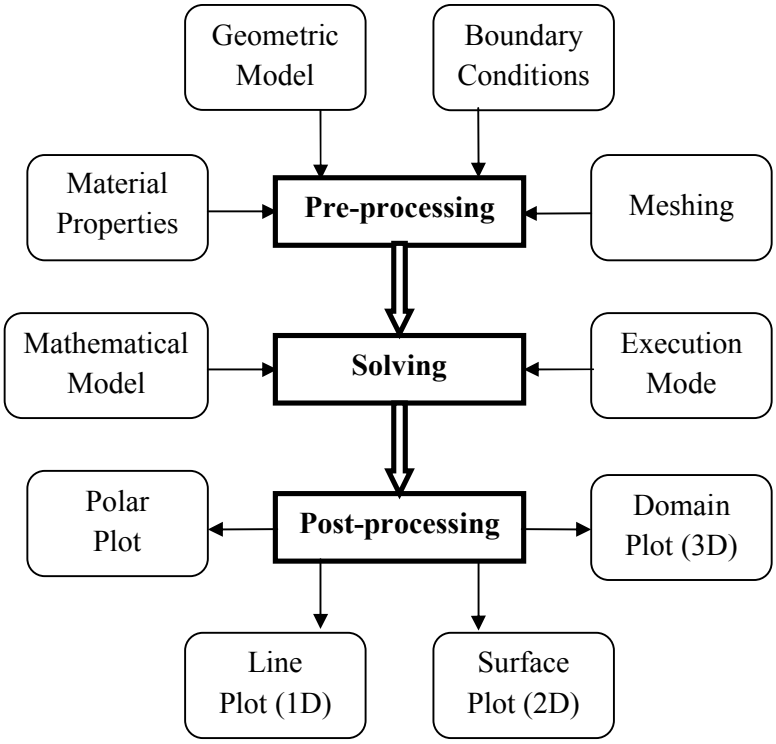

Figure 4.1: General procedures for FEM simulations in COMSOL Multiphysics

4.2.1 Simulated Model

The model of the pressure vessel is created in the COMSOL Multiphysics software using a drawing tool that is available. Since the pressure vessel, electrodes, and bushing are cylindrical in shape, the modelling is simplified into a two-dimensional (2D) model instead of a full three-dimensional (3D) model. Even though it is in a 2D model, the accuracy of the simulation results will not be affected. By adopting this technique, memory and processing time will be saved. Axis-symmetric features are used to simplify further the model without affecting the simulation, as shown in Figure 4.2.

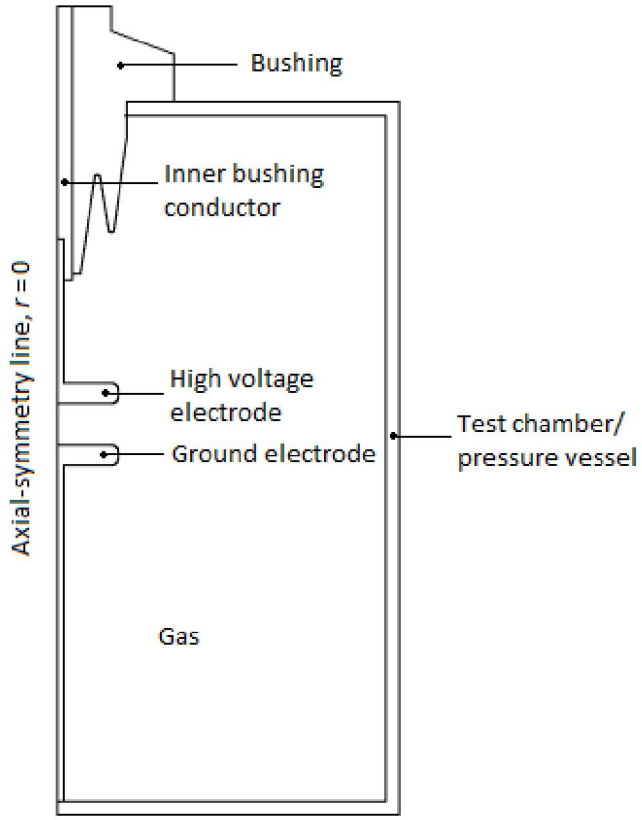

Figure 4.2: A 2D- axis-symmetric model in COMSOL Multiphysics

The above model is based on a plane-plane electrode configuration with a gap of 3 cm. As for other electrode configurations with different gaps, the model can be modified to represent the exact test conditions. All the dimensions are scaled according to the actual setup. As for the above exact model, the diameter of the plane electrode and its edge profile are according to Figure 4.7(a).

4.2.2 Material Properties

In this model, there are three important domains to be considered. These are the conductor, i.e. body of the pressure vessel, conducting rod, and electrodes, and the

dielectric material, i.e. bushing and gas. The conducting domains are defined as what it is in the actual test setup, which are steel for the body of the pressure vessel and the rod and brass for electrodes. However, in simulating electrostatic problems, every conducting domain is excluded in the analysis. Only exterior boundaries of those domains are defined (i.e. high voltage terminal or ground). That leaves the researcher with two other domains. For the bushing, silicone rubber is selected as the dielectric material, as has been stated in the manufacturer's data sheet, with a relative permittivity of 3.1 [94], while for the gas domain the relative permittivity is selected as 1.0 [95]. Generally, for a vacuum and most non-polar gases, or those known as the noble or inert gases [96], relative permittivity can be taken as 1, since the number of atoms or molecules per unit volume is very small compared to those in liquids and solids, except at very high pressures. Table 4.1 shows the material properties used in the modelling, with the exception of conducting materials.

Table 4.1: Properties of materials used for FEM modelling

Materials	Relative permittivity, ε_r
Silicone rubber	3.1
Air	1.0

4.2.3 Boundary Conditions

In the boundary condition settings, only two boundaries in the model have to be defined, i.e. high voltage terminal and ground. For this study, during the experimental phase, the bushing is connected to a full lightning impulse source. The up-and-down method with a step size of 3% is used to evaluate the U_{50} of the specific test conditions. The calculated value of the U_{50} is then used in the simulation investigation to define the

boundary condition in the high voltage terminal setting and then to plot the corresponding electric field.

Ground or 0 V is defined for other conducting materials' boundary conditions, i.e. the ground electrode, the ground rod, and also the body of the pressure vessel. The symmetry line of the model is then set to be the axial-symmetry axis on the r-z plane.

4.2.4 Mesh

The final part in the pre-processing stage is the meshing of the model. After completing the model with geometric drawing, as well as defining the material properties in the domain section and defining the boundary conditions, the whole model is then dissected into non-overlapping triangular elements during the meshing process. Depending on the region of interest, the triangular elements can be refined to be smaller resulting in an increase in the number of the meshing elements that will enhance the accuracy of the simulation results. In this model, focus is being given to the curved edge of the high voltage electrodes, as it is the most likely part to have the maximum electric field magnitudes. As a result, the mesh refinement which results in reduced element size (and hence increases the number of triangular elements), can be seen from the concentrated meshing as shown in Figure 4.3.

The selection of how far the refinement is needed is a trade-off between the accuracy of the plot results, with the memory consumption, and processing time included. The further refinement of the mesh will result in a smoother plot of the electric field, but will consume higher computational memory and will take a longer time to process. An optimised refinement will provide less simulation time without compromising the accuracy of the results.

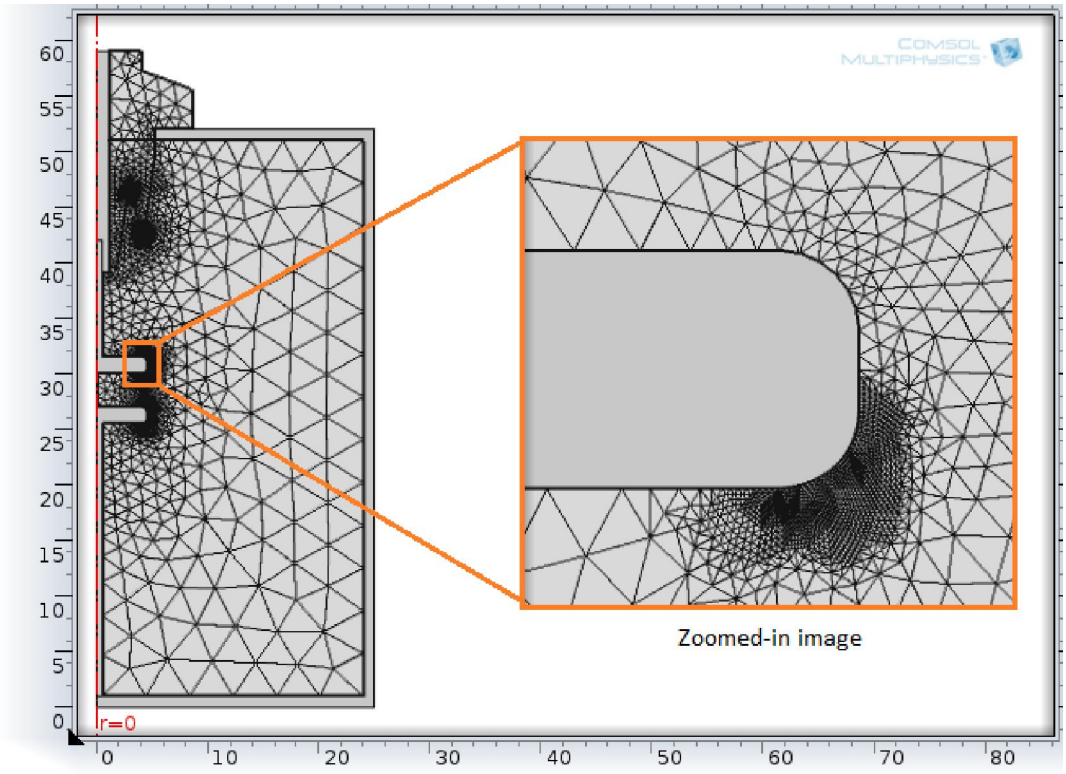

Figure 4.3: Discretisation of the domain problem with mesh refinement at the region of interest (plane-electrode)

4.2.5 Solver Settings

The model is simulated in an AC/DC module through COMSOL Multiphysics software using an electrostatics interface solver. This allows the user to solve a charge conservation equation for the electric potential given the spatial distribution of the electric charge. This interface allows the user to specify permittivity, polarization, or permanent electric displacement of a material to be used in the constitutive relation [97].

4.3 Atmospheric Corrections in Dry Tests

Due to the possibility of deterioration with repeated voltage applications, and in order to ensure all the tests meet the national standard, it is fairly important to consider

correction factors for each test condition. In this specific study, the aforementioned deterioration has been observed in slight changes in temperature while the laboratory works were carried out, albeit just around 0.1 – 0.2 ºC. The standard reference atmosphere is taken as

temperature $t_0 = 20$ ºC

absolute pressure $p_0 = 1013$ hPa (1013 mbar)

absolute humidity $h_0 = 11$ g/m^3

This section will explain atmospheric correction factors related to this study as stated in [45].

4.3.1 Atmospheric Correction Factors for Air Gaps

The breakdown of air insulation depends on the atmospheric conditions. It is usually increased with air density or humidity. When the relative humidity exceeds 80%, the breakdown voltage may become irregular. Hence, the breakdown voltage is proportional to the atmospheric correction factor K_t below

$$K_t = k_1 k_2 \qquad (4.4)$$

where

k_1: the air density correction factor

k_2: the humidity correction factor

By applying correction factors, a breakdown voltage measured, U in given test conditions under temperature t, pressure p, and humidity h, is then converted to the value U_0 which would have been obtained under standard atmospheric conditions with a relation of

$$U_0 = U/K_t \qquad (4.5)$$

4.3.1.1 Air Density Correction Factor, k_1

The air density correction factor k_1 depends on the relative air density δ and can be expressed as

$$k_1 = \delta^m \qquad (4.6)$$

where m is an exponent given in section 4.3.1.3.

If the temperatures, i.e. t and t_0 are expressed in degrees Celsius, and the pressures (i.e. p and $p_{0)}$ are expressed in the same units, the relative air density is represented by

$$\delta = \frac{p}{p_0} \times \frac{273+t_0}{273+t} \qquad (4.7)$$

The above correction is considered reliable for $0.8 < k_1 < 1.05$.

4.3.1.2 Humidity Correction Factor, k_2

The humidity correction factor is represented by

$$k_2 = k^w \qquad (4.8)$$

where w is an exponent given in section 4.3.1.3.

For an impulse, k is a function of the ratio of absolute humidity, h to the relative air density, and δ is given by

$$k = 1 + 0.010\,(h/\delta - 11) \qquad \text{for } 1\ \text{g/m}^3 < h/\delta < 20\ \text{g/m}^3 \qquad (4.9)$$

Eqn. (4.9) applies to both positive and negative polarities of lightning impulse voltages.

4.3.1.3 Exponents *m* and *w*

Since the correction factors depend on pre-discharges, a parameter, *g,* can be illustrated as shown below

$$g = \frac{U_{50}}{500L\delta k} \qquad (4.10)$$

where

U_{50}: 50% breakdown voltage at the actual atmospheric conditions (kV)

L: minimum discharge path (m)

δ: relative air density

k: dimensionless parameter as in Eqn. 4.9

In a case where U_{50} is not available, it can be assumed to be 1.1 times that of the test voltage U_0. For specified ranges of g, as shown in Figure 4.4 and Figure 4.5, the exponents m and w can be obtained from Table 4.2.

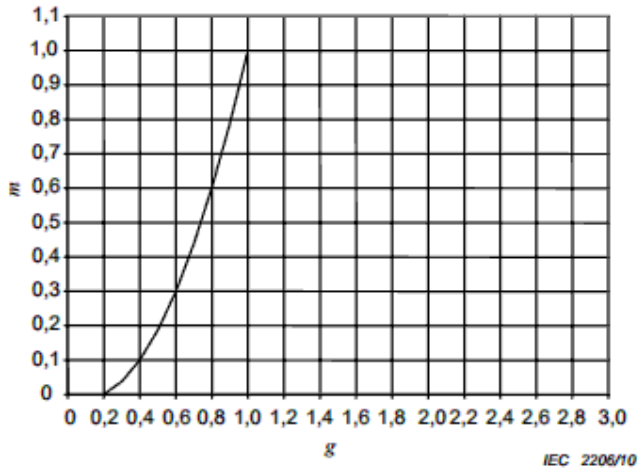

Figure 4.4: Values of exponent *m* for air density correction as a function of parameter *g* [45]

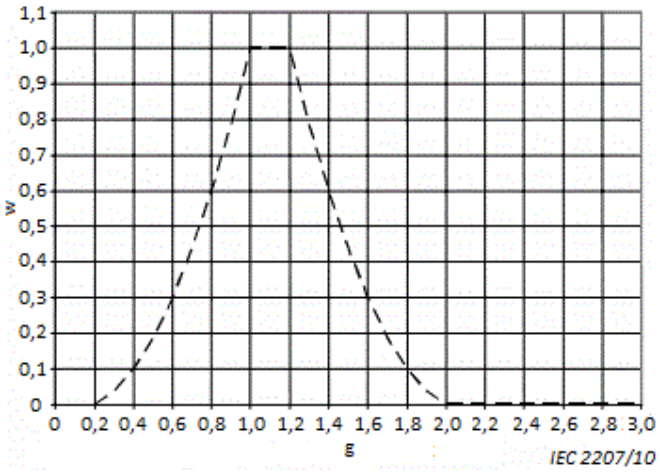

Figure 4.5: Values of exponent *w* for humidity correction as a function of parameter *g* [45]

Table 4.2: Values for exponents *m* for air density correction and *w* for humidity correction, as a function of the parameter *g* [45]

g	***m***	***w***
< 0.2	0	0
0.2 to 1.0	$g(g - 0.2)/0.8$	$g(g - 0.2)/0.8$
1.0 to 1.2	1.0	1.0
1.2 to 2.0	1.0	$(2.2 - g)(2.0 - g)/0.8$
> 2.0	1.0	0

4.3.1.4 Humidity Measurement for Correction

In this study, temperature and humidity measurements are recorded by a wireless temperature and humidity sensor as explained in section 3.7. The data are recorded in relative humidity, instead of absolute humidity, and degrees Celsius. In practice, humidity is the actual amount of moisture in a specific volume of air while relative humidity, on the other hand, is the percentage of the maximum amount of moisture that is possible in a specific volume of air at a given temperature. The relation between the absolute humidity, *h,* with the relative humidity and the ambient temperature is recorded as

$$h = \frac{6.11 \times R \times e^{\frac{17.6 \times t}{243+t}}}{0.4615 \times (273+t)} \qquad (4.11)$$

where

h: the absolute humidity in g/m^3

R: the relative humidity in percent

t: the ambient temperature in ºC

With an air-tight seal, no significant change in relative humidity has been recorded. The steps for atmospheric corrections can be summarized using the flow chart below:

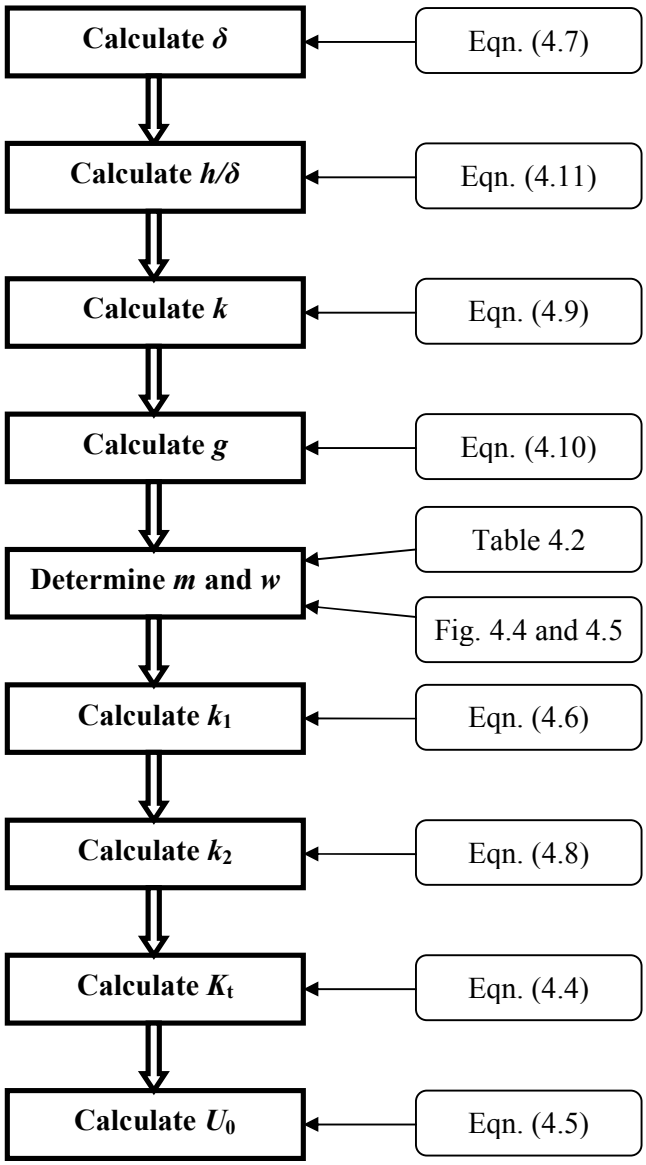

Figure 4.6: Flowchart for atmospheric corrections in dry tests

4.4 Experimental Characterisation on Air Breakdown

In these tests, three configurations of electrodes have been selected and used to study the breakdown voltage of air and as a verification and calibration process to the experimental test setup prior to further tests with CF_3I gas mixtures. The three configurations of electrodes represent three different kinds of electric field stress in the pressure vessel with three different gaps. It is recommended that the gap-to-size ratio of the electrodes is kept at 6-7:1 maximum. The up-and-down method is used to determine U_{50} by applying at least 20 impulse shots at a timed interval of 60 seconds. The behaviours of air breakdown obtained from the test measurements are then used in simulation to determine the electric field.

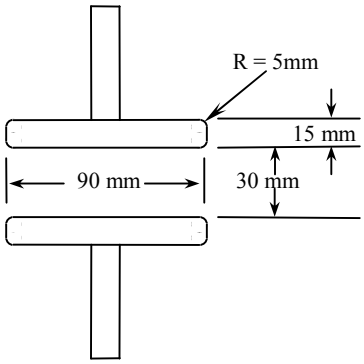

(a) Plane-plane; 3 cm gap

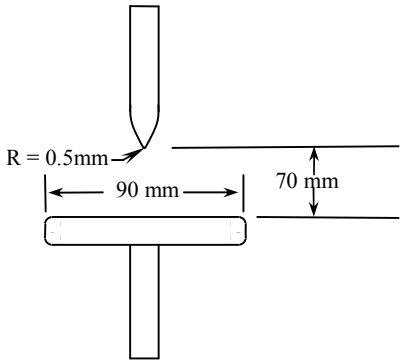

(c) Rod-plane; 7 cm gap

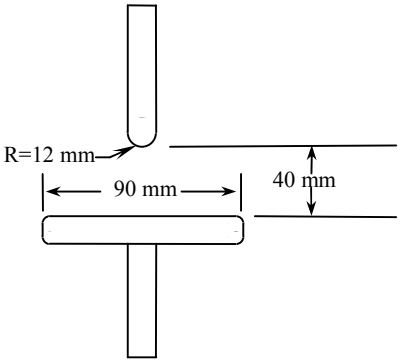

(b) hemisphere-plane; 4 cm gap

Figure 4.7: Three configurations of gap electrode for air breakdown tests

4.4.1 Effect of Gap Length and Pressure

In the tests, one electrode configuration, the rod-plane as shown in Figure 4.7(c), has been selected in order to investigate the effects of gap lengths on the breakdown behaviour of air. This is because the majority of insulating systems are in non-uniform gap configurations. The gaps used in these tests are 5 cm, 6 cm, 7 cm, and 8 cm. The results are shown in Figure 4.8, with Table 4.3 showing the values for positive lightning impulse.

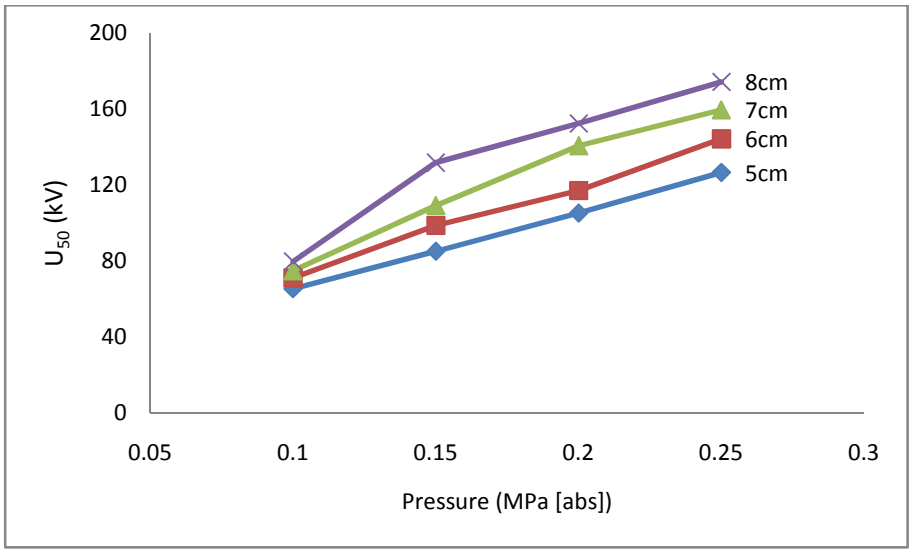

Figure 4.8: U_{50} for air breakdown in rod-plane gap as a function of pressure (positive polarity)

Table 4.3: U_{50} for air breakdown in rod-plane configuration (kV)

	Gap length			
Pressure (Mpa [abs])	**5 cm**	**6 cm**	**7 cm**	**8 cm**
0.10	65.3	71.0	74.8	79.7
0.15	85.1	98.7	109.1	131.8
0.20	105.2	117.1	140.6	152.3
0.25	126.5	144.3	159.6	174.3

Reviewing the U_{50} curves (Figure 4.8), the U_{50} of air increases almost linearly with increasing pressure, particularly for the 5 cm gap length. By considering only U_{50} taken at 0.10 MPa and 0.25 MPa, the U_{50} increased by 1.94 times for the 5 cm gap, 2.03 times for the 6 cm gap, 2.13 times for the7 cm gap, and 2.19 times for an 8 cm gap. This shows that a bigger gap length in electrode configuration will introduce a slightly bigger increase in U_{50} with the increment of pressure. However, at 0.1 MPa, there is not much difference in the values of U_{50} for different gaps.

The increment trends with pressure for each gap length in U_{50} of air breakdown agree with investigations on air breakdown by Husain and Nema [98] and Govinda Raju and Hackam [99], where U_{50} increases almost linearly from 0.1 MPa (750 torr) to 0.25 MPa (1875 torr). This region is where the Paschen curve is linear, albeit according to Lux [100], Paschen's Law applies typically at *pd* products of less than 1000 torr-cm. Naidu and Kamaraju [101], however, has published a Paschen curve for SF_6 gas at *pd* products of up to 2000 torr-cm, which is a linear curve from 500 torr-cm onwards. Nevertheless, deviations from linearity of Paschen's Law can happen due to the geometry of the electrode, where high electric field is introduced in non-uniform electrode configuration, as being carried out in this study.

The value of each U_{50} in Table 4.3 is then used in the COMSOL Multiphysics software to evaluate the maximum electric field (E_{max}) in each test configuration. This is because most of the time the pre-discharges occur in the region of high stress, where the E_{max} exists. Figure 4.9 shows an example of the location of E_{max} and the electric field plot along the given length. The model used is a 5 cm gap rod-plane electrode configuration. Figure 4.10 shows the electric field plot along the edge of the high voltage electrode from the tip of the rod to the side. As illustrated in Figure 4.9, the E_{max}

occurs at the tip of the rod with a value of approximately 376 kV/cm for a voltage of 65.3 kV (U_{50} at 0.10 MPa).

Referring to Figure 4.9, it is clear that E_{max} occurs at the tip of the electrode (point 'a'). This is true for all gap lengths in this study (i.e. for 5 cm, 6 cm, 7 cm and 8 cm gaps). This E_{max} will introduce a very high stress region and eventually pre-discharge will start to occur. This is followed by the breakdown of air starting at the tip of the rod onto the surface of the ground electrode.

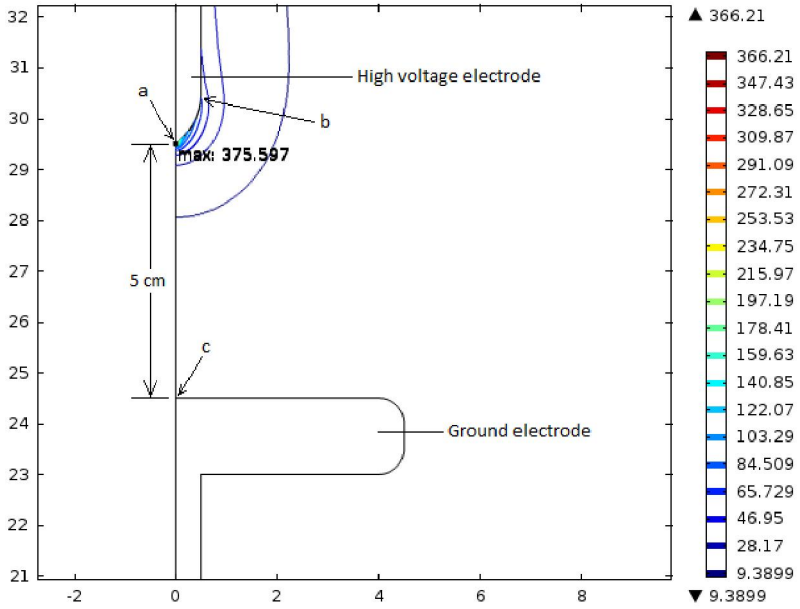

Figure 4.9: Lines of electric field with equal magnitudes with maximum electric field region at the tip of the rod (kV/cm)

Figure 4.10 shows the electric field plot along the edge of the rod electrode, starting from tip of the rod (point 'a' in Figure 4.9) and ending where the rod cap meets the straight edge (point 'b' in Figure 4.9). The maximum electric field occurs at point 'a', and the magnitude of electric field decreases as the length gets further from point 'a'. It can be seen that very high concentration of electric field occurs in the region

within 0.05 cm from the tip of the rod electrode. At 0.15 cm from the tip, the magnitude of electric field decreases steadily until it reaches point ‘b’.

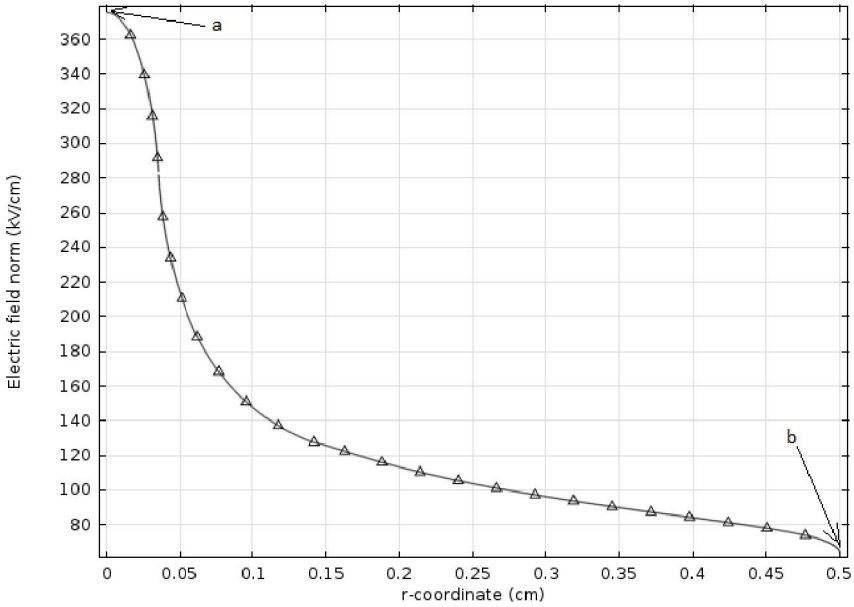

Figure 4.10: Electric field magnitude along the edge of the high voltage conductor (refer to Figure 4.9)

Figure 4.11 shows the electric field plot along the gap axis, starting from the tip of the high voltage rod (point ‘a’ in Figure 4.9) and ending at the surface of the ground plane electrode (point ‘c’ in Figure 4.9). Along this gap length, the electric field decreases exponentially. This exponential curve agrees with the investigation by Mavroidis et al. [102], where the electric field decreases sharply across the gap with a faster rate as the gap length increases [102]. Figure 4.12 shows the per unit value of E/E_{max} along the gap length.

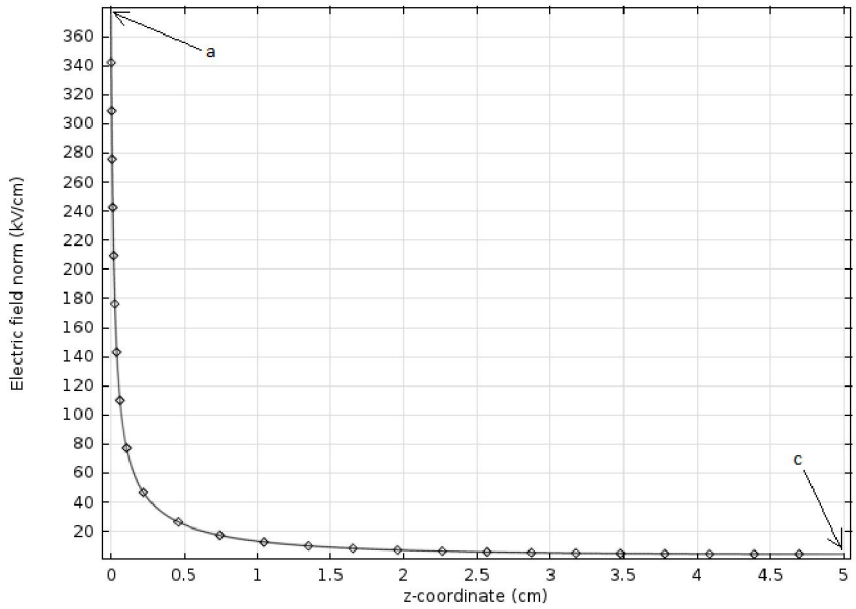

Figure 4.11: Electric field magnitude along the gap axis of the rod-plane electrode (refer to Figure 4.9)

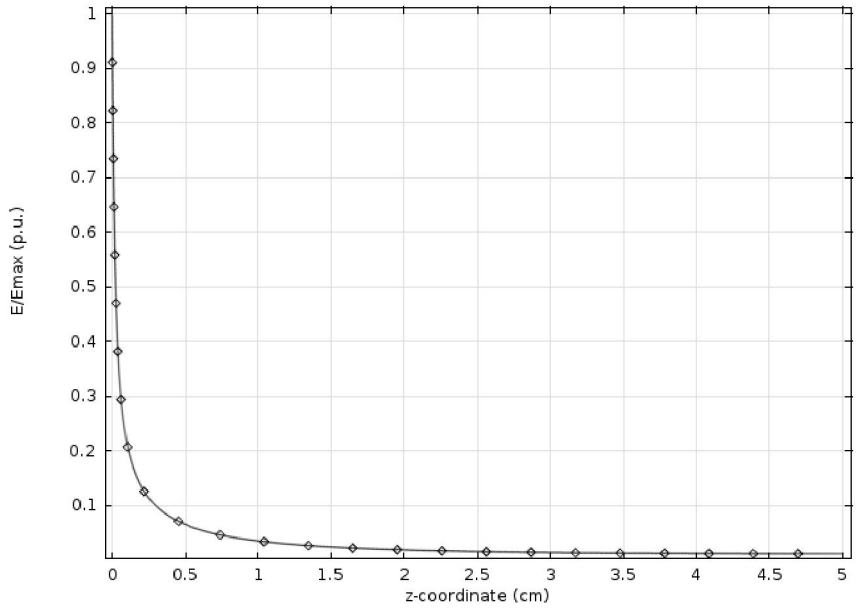

Figure 4.12: E/E_{max} curve along the gap of the rod-plane electrode

Table 4.4 shows E_{max} values for all the gap lengths in the rod-plane electrode configuration in correspondence with the respective U_{50} values from Table 4.3. Figure 4.13 shows the E_{max} curves, in relation to gap lengths, based on each pressure.

Table 4.4: E_{max} for air breakdown in the rod-plane configuration (kV/cm)

	Gap length			
Pressure (Mpa [abs])	**5 cm**	**6 cm**	**7 cm**	**8 cm**
0.10	376	398	413	435
0.15	489	554	602	719
0.20	605	657	776	831
0.25	727	810	881	951

Closer consideration of the E_{max} curves (Figure 4.13) offers a clear indication that, for low pressure (at 0.10 MPa), the E_{max} values are almost the same for every gap length. As the pressure is increased, the ability of air to withstand E_{max} (and high stress) is increased. This is particularly true for a higher gap length between the electrodes. Also, importantly, it can be deduced that by increasing a same amount of air pressure, a higher E_{max} withstand capability can be achieved in a longer gap length for this particular electrode configuration.

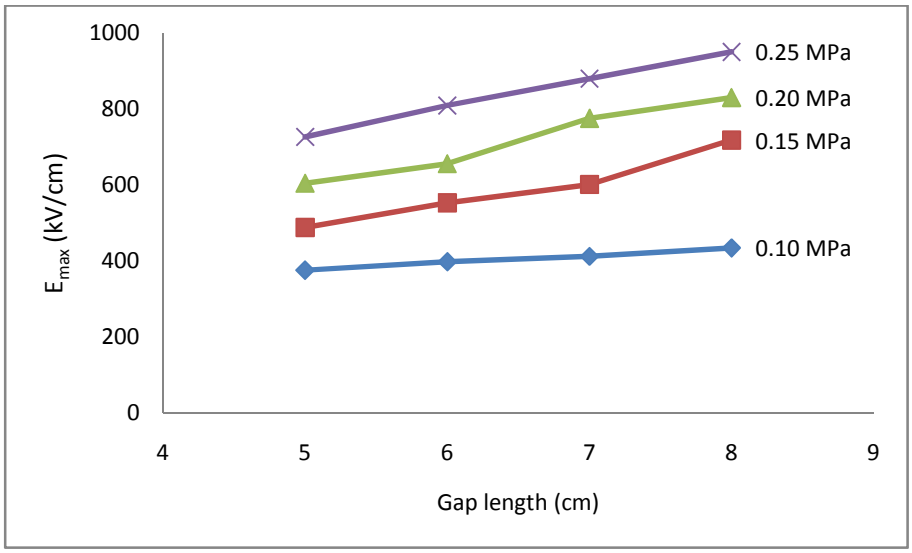

Figure 4.13: E_{max} for air breakdown in a rod-plane gap as a function of gap length (positive polarity)

Figure 4.14 and Figure 4.15 show U_{50}-*pd* curve and the E_{max}-*pd* curve respectively, which can be seen as almost linear curves. The U_{50}-*pd* (and hence E_{max}-*pd*)

curve agrees with Paschen characteristics as reported by Heylen [103] for the given pressures. Naidu and Kamaraju [101] also reported a linear Paschen curve for higher *pd* products. Although the magnitudes of the U_{50} in this investigation are significantly higher, as the tests were carried out using rod-plane electrode configuration, the U_{50}-*pd* curve is almost linear for the region specified, which conforms to [103].

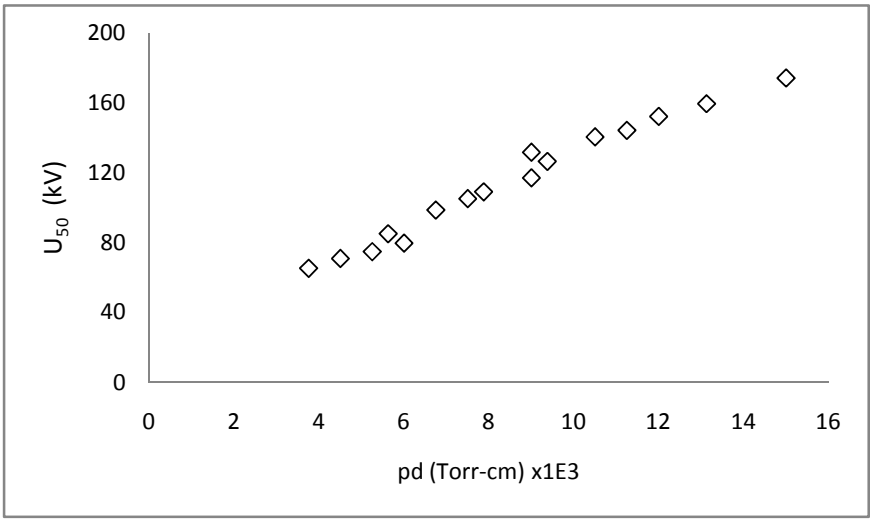

Figure 4.14: U_{50} curve for air under rod-plane electrode configuration in relation to product of pressure and gap length, *pd*

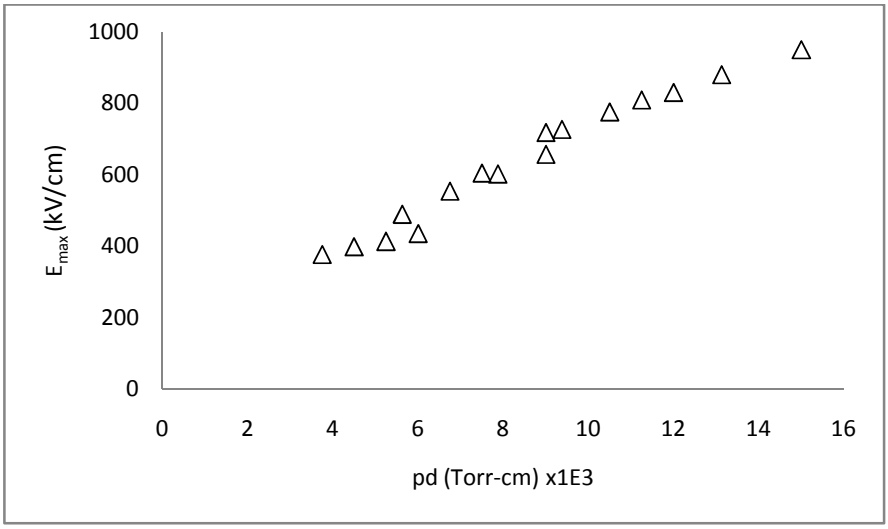

Figure 4.15: E_{max} curve for air under rod-plane electrode configuration in relation to product of pressure and gap length, *pd*

4.4.2 Effects of Electrode Configuration

Further tests have been carried out to obtain U_{50} curves for different electrode profiles as shown in Figure 4.7. For the plane-plane electrode configuration (configuration (a)), a 3 cm gap was used. For a R12-plane (configuration (b)), a 4 cm gap was used, and for the rod-plane (configuration (c)), a 5 cm gap was adopted. This test data is included in Table 4.3. The results of U_{50} measurements are shown in Figure 4.16 below and the values are given in Table 4.5.

Table 4.5: U_{50} for different electrode configurations (kV)

Pressure (Mpa [abs])	Plane-plane; 3cm	R12-plane; 4cm	Rod-plane; 5cm
0.10	81.84	72.80	65.33
0.15	112.62	89.57	85.13
0.20	139.97	111.73	105.18
0.25	162.37	129.42	126.52

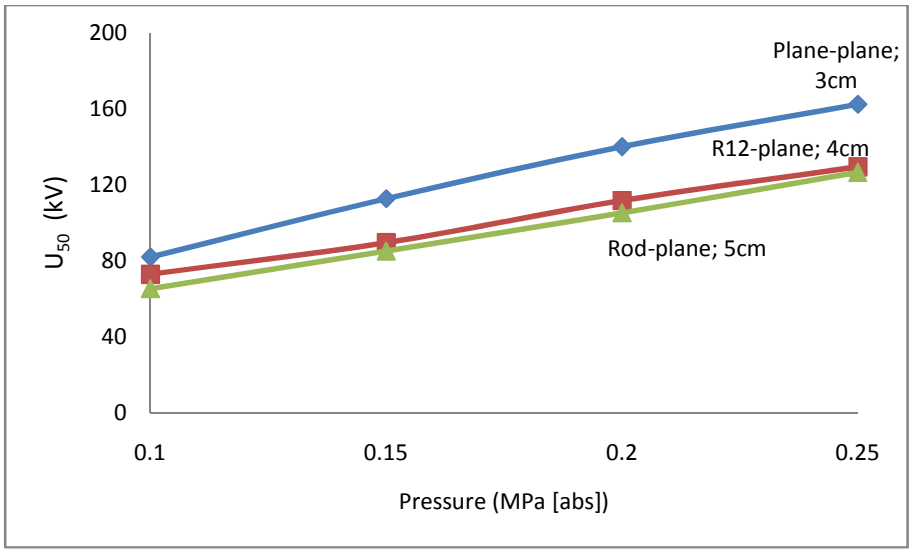

Figure 4.16: U_{50} for different electrode configurations

As depicted in Figure 4.16, although the rod-plane configuration has the biggest gap, the U_{50} values are the lowest for each given pressure, though only small differences

exist when compared with that of the R12-plane configuration. For the plane-plane configuration, although it has the smallest gap length, the highest U_{50} of all the pressures is noted. For all electrode configurations, the U_{50} increases almost linearly with the pressure, in this case, from 0.10 MPa up to 0.25 MPa.

Electric field behaviour is investigated using the experimentally obtained U_{50} values with the aid of the COMSOL Multiphysics software. For the rod-plane electrode configuration, the distribution of the electric field along the high voltage electrode is the same as in Figure 4.10, while for the plane-plane and R12-plane configurations, the numbers are shown in Figure 4.17 and Figure 4.18, respectively.

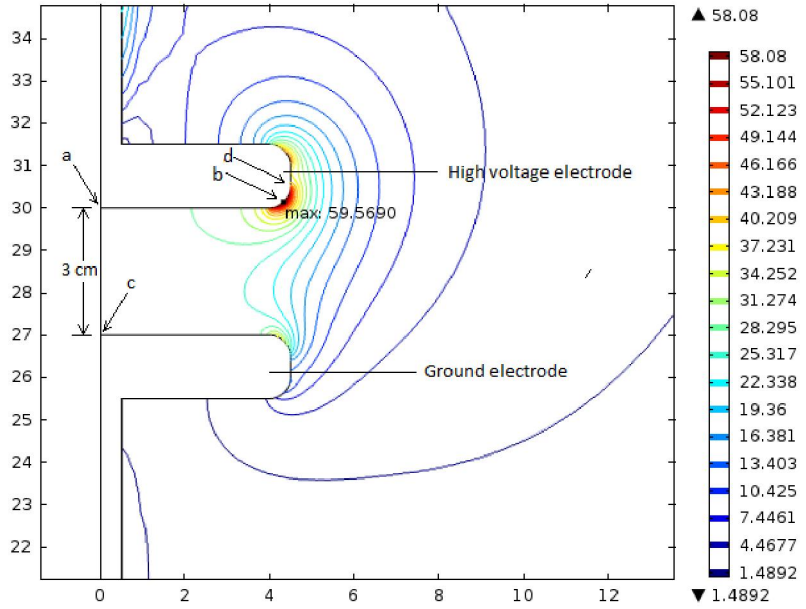

Figure 4.17: Lines of electric field with equal magnitudes with maximum electric field region at the edge of the electrode for plane-plane configuration (kV/cm)

As clearly shown in Figure 4.17, the maximum electric field, E_{max} occurs at the very edge of the high voltage plane electrode. This is the most likely location where the pre-discharges will occur, followed by air breakdown. This knowledge is very useful if recording using a high speed camera is desirable, since the camera can be focused on

this particular region. With a voltage of 81.8 kV (U_{50} at 0.10 MPa) the E_{max} at the highest stress part is shown as 60 kV/cm. It has to be noted that the E_{max} values are purely simulation, as they are not real electric field. This is due to the fact that breakdown occurs just before the electric field reaches the calculated E_{max} values.

Figure 4.18 shows that the E_{max} occurs at the tip of the R12 high voltage electrode, as expected for this kind of electrode configuration with positive impulse polarity. E_{max} is given as 65 kV/cm for a voltage of 72.8 kV (U_{50} at 0.10 MPa).

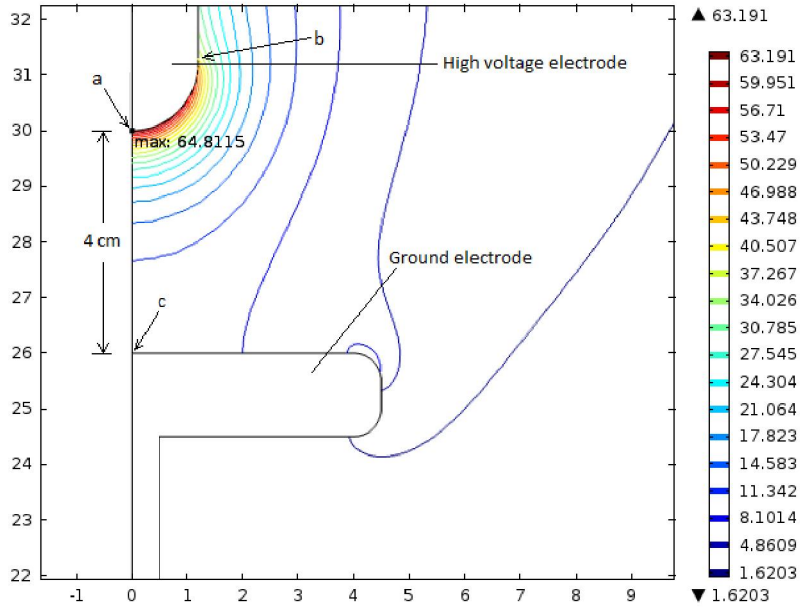

Figure 4.18: Lines of electric field with equal magnitudes with maximum electric field region at the edge of the electrode for a R12-plane configuration (kV/cm)

Figure 4.19 and Figure 4.20 show the electric field curve at the surface of the electrode for the plane-plane and R12-plane configurations, respectively. Figure 4.21, on the other hand, shows the electric field plot along the gap length.

Referring to Figure 4.19 the minimum electric field on the surface of the energized plane electrode occurs at the centre of the electrode, (point 'a' in Figure 4.17).

As the distance move towards the edge of the plane electrode (point 'b' in Figure 4.17), the electric field increases exponentially until at the very edge of the electrode, where the maximum electric field, E_{max} occurs. Moving towards point 'd' as in Figure 4.17, the electric field then decreases sharply. This electric field plot shows that although the electrode system in use is plane-plane configuration, this electrode system cannot be taken as a fully uniform field configuration as in the Rogowski or Bruce electrode profiles [104].

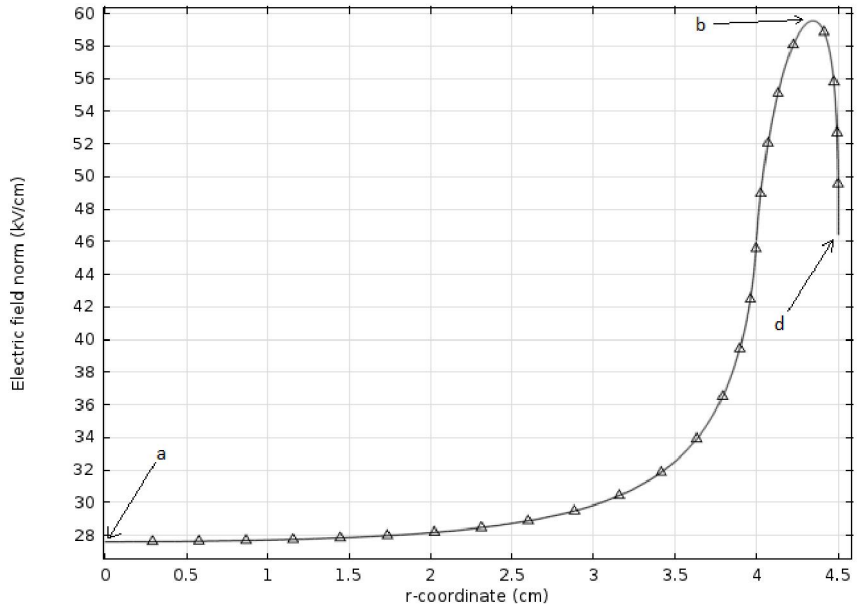

Figure 4.19: Electric field magnitude along the surface of the plane (energized) electrode in plane-plane configuration (refer to Figure 4.17)

At the centre of the plane-plane electrode, the electric field is given as

$$E = \frac{V}{d} \qquad (4.12)$$

For U_{50} = 81.8 kV and d = 3 cm, the calculated electric field is E = 27.3 kV/cm. This is in line with the electric field curve in Figure 4.19 at r-coordinate = 0 cm (at the centre of plane-plane electrode), shown as point 'a'.

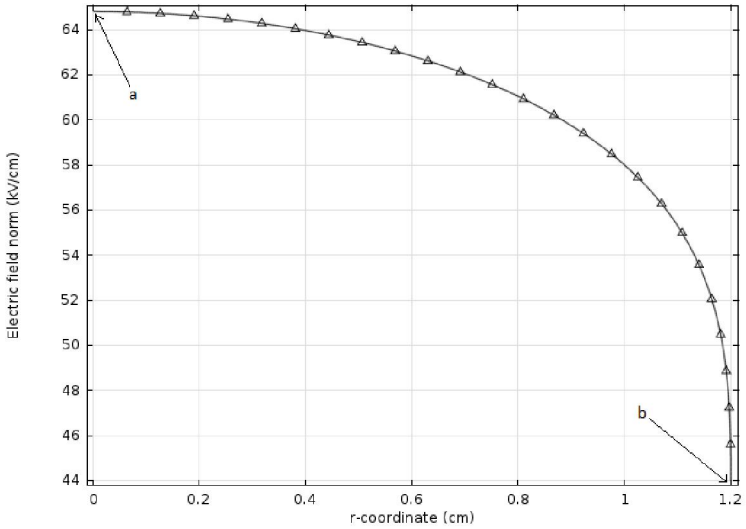

Figure 4.20: Electric field magnitude along the R12 electrode in R12-plane configuration (refer to Figure 4.18)

In Figure 4.20, the maximum electric field, E_{max} occurs at the tip of the R12 electrode (point 'a' in Figure 4.18). As the distance from the tip move towards point 'b' along the surface of the R12 electrode as in Figure 4.18, the electric field magnitude decreases steadily until at around 0.8 cm, whereas after that it decreases sharply with a faster rate as the distance increases.

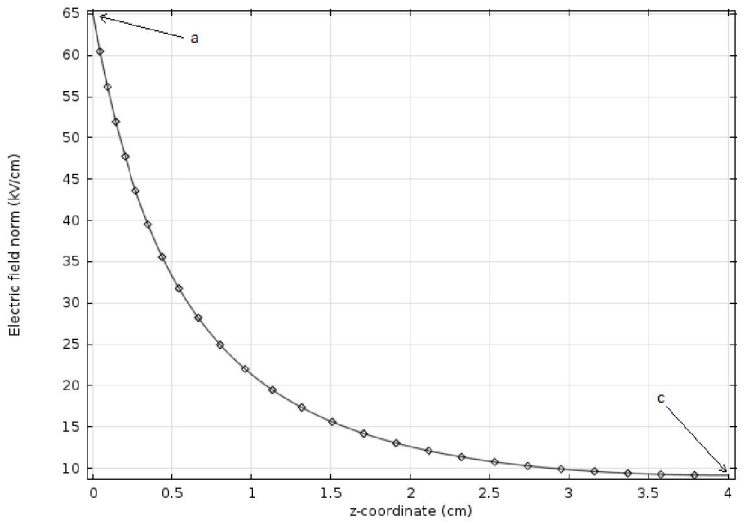

Figure 4.21: Electric field magnitude along the gap of the R12-plane electrode (refer to Figure 4.18)

As the R12-plane electrode configuration is almost identical to rod-plane electrode configuration, except that the latter has a significantly lower diameter at the tip of the rod, the electric field distribution along the gap length should give almost the same trend as well. Figure 4.21 shows that the electric field decreases exponentially from the tip of the R12 electrode towards the point 'c' as in Figure 4.18. E_{max} values corresponding with Table 4.5 are shown in Table 4.6.

Table 4.6: E_{max} for different electrode configurations (kV/cm)

Pressure (Mpa [abs])	Plane-plane; 3cm	R12-plane; 4cm	Rod-plane; 5cm
0.10	60	65	376
0.15	82	80	489
0.20	102	99	605
0.25	118	115	727

According to Table 4.6, there is not much difference in E_{max} values between a 3 cm gap plane-plane electrode configuration and a 4 cm gap, R12-plane electrode configuration. Although in terms of geometry these electrode configurations are very different from each other, the U_{50} values, as shown in Figure 4.16 through the results of computational works on the electric field, reveal that the E_{max} values are very close to each other. This is true for all pressures carried out during the experimental works. It can be said that, in this particular study, the R12-plane electrode configuration with a gap length of 4 cm will result in the same magnitude of E_{max} for the air to breakdown as in the plane-plane electrode configuration with a gap length of 3cm.

Field utilization factor, η, can be calculated for each electrode configuration using Eqn. (4.13) to give an idea of non-uniformity of the gap geometry, i.e. a higher value of η indicates a more uniform electric field

$$\eta = \frac{E_{mean}}{E_{max}} \qquad (4.13)$$

and E_{mean} can be calculated using Eqn. (4.14)

$$E_{mean} = \frac{V}{d} \qquad (4.14)$$

where

V: voltage applied

d: gap length

By taking applied voltage, V as 1 kV and using COMSOL to determine E_{max}, the field utilization factor, η, for each electrode configuration is shown in Table 4.7.

Table 4.7: Field utilization factors for each electrode configuration with V = 1 kV

Electrode configuration	E_{max} (kV/cm)	E_{mean} (kV/cm)	Field utilization factor, η
Rod-plane; 5 cm gap	5.75	0.20	0.035
R12-plane; 4 cm gap	0.89	0.25	0.281
Plane-plane; 3 cm gap	0.73	0.33	0.452

The *pd* curves for U_{50} and E_{max} on all the electrode configurations are shown in Figure 4.22 and Figure 4.23.

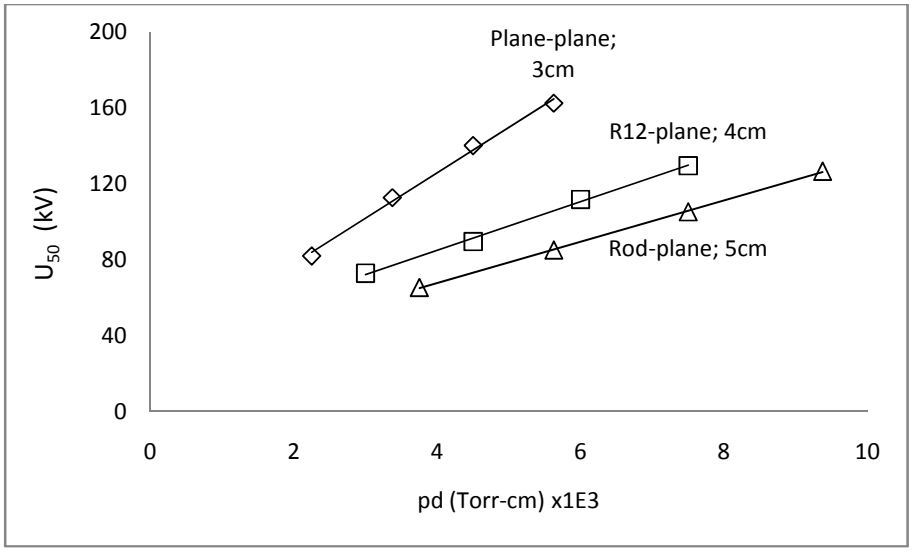

Figure 4.22: U_{50} curve in relation to the product of pressure and gap length, *pd,* for all electrode configurations

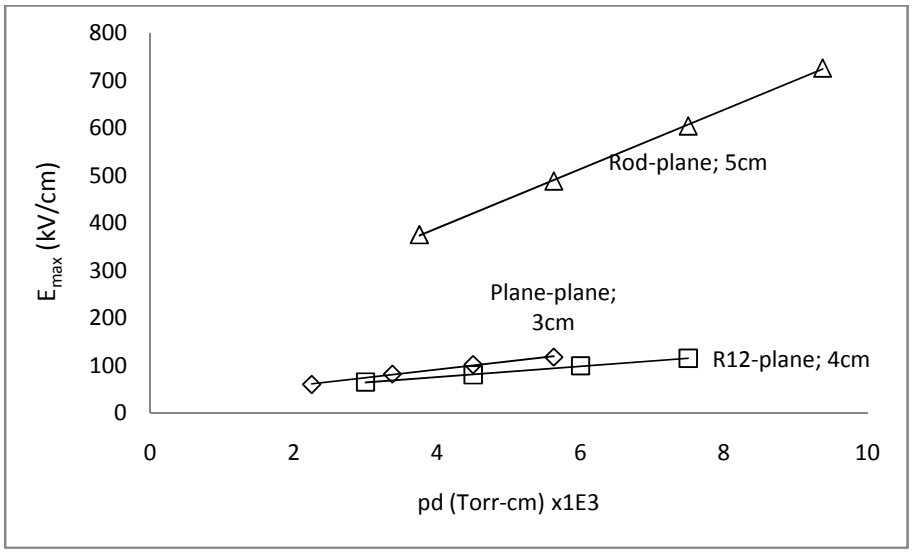

Figure 4.23: E_{max} curve in relation to the product of pressure and gap length, *pd*, for all electrode configurations (see also Table 4.6)

The *pd* curves in Figure 4.22 can be described as part of the Paschen characteristics for the given electrode system where the curves are linear at higher *pd* products, as reported by Heyley [103] and Naidu and Kamaraju [101]. Also, the above U_{50}-*pd* curves agree with an investigation carried out by Woo et al. [105] where it is concluded in general that the slope of breakdown voltage is decreased with the non-uniformity of the electric field. As have been discussed in section 4.4.1, the slope of the Paschen's Law is not necessarily linear due to the geometry of the electrode system. As the electrode configuration varies, the Paschen's curve also varies accordingly, which is unique to the electrode system.

4.5 Conclusion

The finite element model is essential in viewing the behaviour of electric fields under various circumstances, such as the effects of gap length between electrodes and the effects of the geometry of the electrodes themselves. In this study, a model for finite

element modelling has been developed. The fact that the real model of the test setup is cylindrical in shape makes the modelling more simplified by using the axial-symmetry features in the software packages.

Fundamental tests on air breakdown have been carried out to investigate the U_{50} behaviour of air in various test conditions. The results are corrected according to the correction factors defined by the standard in BS EN 60060-1 (2010) to ensure the accuracy of the results are reliable. The values of U_{50} are then used to determine the E_{max} using finite element modelling software. This is used to give a better understanding of the highest stress region inside the test chamber. Electric field lines can also be plotted along the surface of the high voltage electrodes if desired. It was found that although breakdown in rod-plane gaps occur within smaller voltage levels, the E_{max} at the breakdown level is the highest among all the electrode configurations.

CHAPTER 5: BREAKDOWN PROPERTIES OF CF_3I AND ITS MIXTURES UNDER LIGHTNING IMPULSE: EFFECT OF GAP GEOMETRY AND IMPULSE POLARITY

5.1 Introduction

In this study, the focus is given to the mixture of CF_3I-CO_2 with a ratio of 30%-70%. As was discussed in Chapter 2, the selection of partial pressure of CF_3I in the mixture is a trade off between three basic factors; boiling point of the gas mixture, insulation strength, and the by-products of the gas mixture upon each electrical discharge.

For CF_3I-CO_2 mixtures, 30%-70% is the most appropriate ratio to be used as an insulation medium. This ratio has also been suggested by Katagiri et al. [40] for gas-insulated switchgear (GIS) applications. Kasuya et al. [41] suggested the same for gas circuit breaker (GCB) applications. According to Katagiri et al. [40], for the same ratio, the interruption capability of CF_3I-CO_2 mixtures is far superior to that of CF_3I-N_2 mixtures. With only 30% of the CF_3I in the CF_3I-CO_2 mixtures the insulation performance is approximately 0.75 to 0.80 times that of SF_6.

In another report by Kasuya et al. [42], it is shown that CF_3I-CO_2 gas mixtures with a ratio of 30%-70% generates less iodine after current interruption, only 1/3 of which is pure CF_3I. This is essential as the lower the iodine, the lower the effects on CF_3I insulation performance, as reported by Takeda et al. [57].

5.2 Calculation of CF_3I-CO_2 Mixtures

CF_3I for this study was obtained from Apollo Scientific Limited. The CF_3I is supplied in liquid form, contained in a small cylinder bottle, weighs around 1 kg nett per bottle. Figure 5.1 shows the CF_3I bottle used in this study and Figure 5.2 provides the description.

Figure 5.1: 1 kg CF_3I bottle

Figure 5.2: CF_3I description on the bottle

As explained in section 2.5, the gas mixture can be determined by taking the partial pressure of each individual gas. Equation (2.2) demonstrates Dalton's Law and in this case, the mixture of CF_3I-CO_2 can be shown as

$$P_{total} = P_{CF3I} + P_{CO2} \qquad (5.1)$$

This means that for at total pressure of 1 bar (abs), or 0.10 MPa (abs), the partial pressures for CF_3I-CO_2 gas mixtures with ratio of 30%-70% are 0.30 bar (abs) and 0.70 bar (abs) for CF_3I and CO_2, respectively.

In order to fill up the pressure vessel or the test chamber, a calculation has to be made to ensure that 1 kg of CF_3I is enough for the application and if enough, how long the CF_3I will last. The dimensions of the pressure vessel are given as

height: 50 cm

diameter: 50 cm

Hence the volume, V, will be

$$V = \pi \times r^2 \times h \qquad (5.2)$$

$$= \pi \times (25\ cm)^2 \times 50\ cm$$

$$= 0.00982\ m^2;\ \text{or } 98.2\ \text{litre}$$

By considering only 0.30 bar for CF_3I (30%-70% ratio of CF_3I-CO_2 mixture), and by using the ideal gas law,

$$PV = nRT \qquad (5.3)$$

where in this case,

P: partial pressure of CF_3I, i.e. *0.30 bar*

V: volume of the pressure vessel, calculated as *98.2 litre*

n: number of moles of CF_3I

R: gas constant, i.e. *0.082 l.bar/mol.K*

T: temperature of CF_3I gas, assumed to be *20 ºC* (*293.15 K*)

For CF_3I, the molecular weight can be calculated as

$$MW_{CF3I} = MW_{Carbon} + 3\times MW_{Fluorine} + MW_{Iodine} \quad (5.4)$$

$$= 12.01 + 3\times 19 + 126.90$$

$$= 195.91 \text{ g}$$

Calculating, for 1 kg (1000 g) of CF_3I,

$$\text{Number of moles, n} = \frac{1000}{195.91}$$

$$= 5.1044$$

For 1 kg of CF_3I at a temperature of 293.15 K and a pressure of 0.30 bar,

$$\text{Volume, V} = \frac{nRT}{P}$$

$$= \frac{(5.1044)(0.082)(293.15)}{0.30}$$

$$= 409 \text{ litre}$$

For a pressure vessel with a volume of 98.2 litre,

$$\text{Number of fillings} = \frac{409}{98.2}$$

$$= 4.16$$

$$\approx 4 \text{ times}$$

From the above calculations, for a bottle of 1 kg of CF_3I, the pressure vessel used in this study can be filled 4 times with CF_3I-CO_2 gas mixtures with a ratio of 30%-70% at 1.0 bar (abs), or 0.10 MPa (abs). To mix the gases, CF_3I is first pumped in up to the calculated partial pressure, specifically 0.30 bar and then CO_2 is pumped into the vessel up to the total pressure of 1.0 bar. Using this method, CF_3I-CO_2 gas mixture has been achieved. Before any tests are carried out, the gas mixture is left for at least 24 hours so that the mixture truly blends together, as recommended by Ohtsuka et al [86], where the repeatability of the results can be achieved beyond 24 hours, as has been discussed in section 3.11.

5.3 Effects of Electrode Configuration and Impulse Polarity

The effects of electrode configuration and impulse polarity are investigated in this section. Both positive and negative polarities of standard lightning impulse 1.2/50 were used in the tests. There are three electrode configurations for the tests, namely rod-plane, plane-plane, and sphere gap as shown in Figure 5.3.

For rod-plane and plane-plane electrode configurations, the models used for finite element modelling and electric field lines behaviour are the same as shown in section 4.4. In this section, only the model for sphere gap and the corresponding electric field line behaviour will be shown. These are depicted in Figure 5.4 and Figure 5.5. Figure 5.6 shows the electric field distribution along the gap length between the two sphere electrodes.

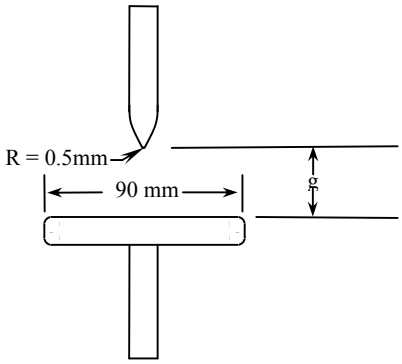

(a) rod-plane

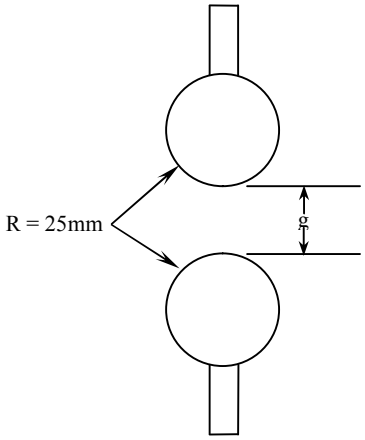

(c) sphere gap

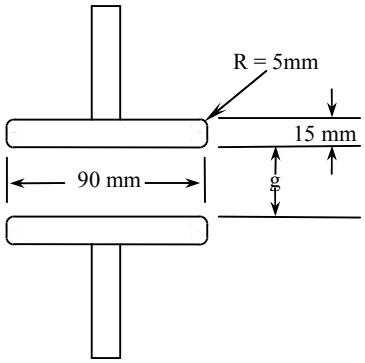

(b) plane-plane

Figure 5.3: Three configurations of electrodes for CF_3I gas mixtures breakdown tests

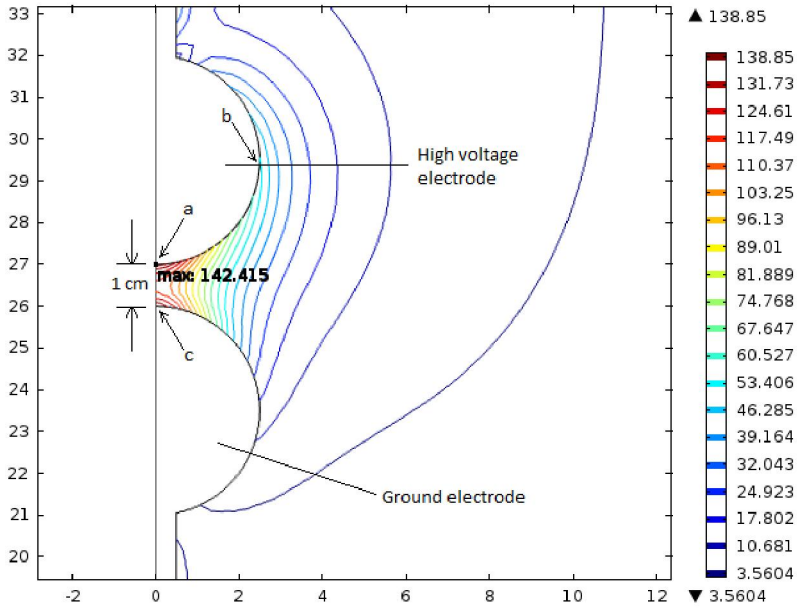

Figure 5.4: Lines of electric field with equal magnitudes with maximum electric field region at the tip of the sphere gap configuration (kV/cm)

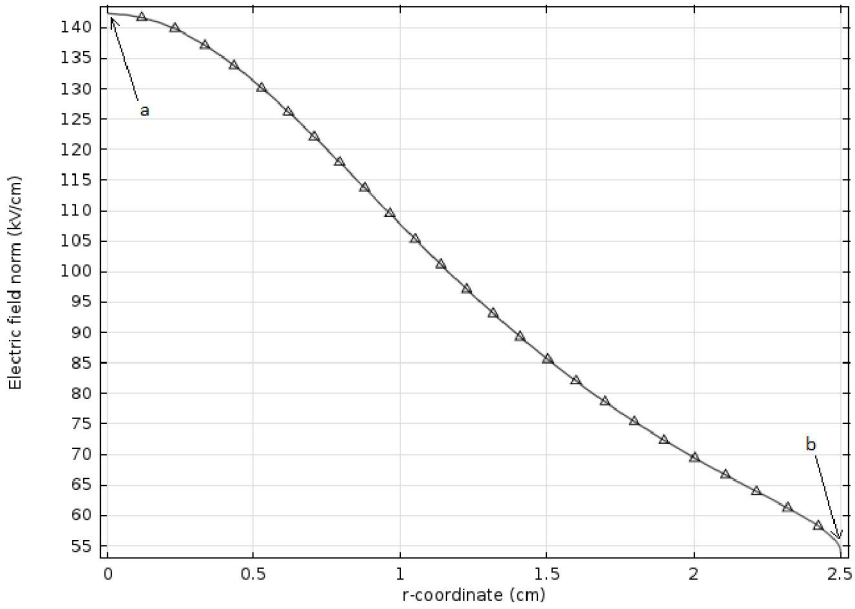

Figure 5.5: Electric field along the surface of high voltage sphere electrode for a voltage of 123.82 kV(refer to Figure 5.4)

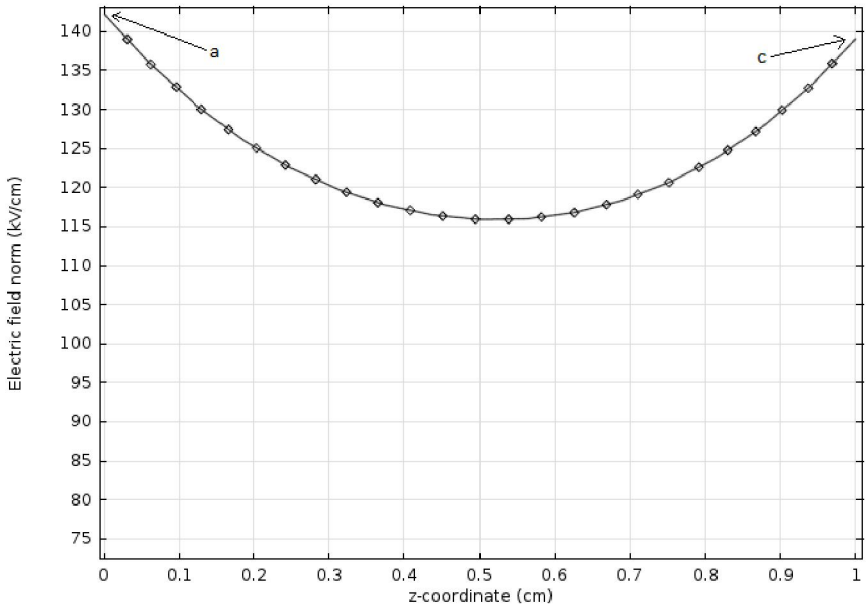

Figure 5.6: Electric field along the gap of the sphere gap electrode (refer to Figure 5.4)

Referring to Figure 5.5 and Figure 5.6, maximum electric field occurs at point 'a', which is at the tip of the sphere, as shown in Figure 5.4. As the distance moves away from point 'a' along the surface of the sphere, electric field magnitude decreases steadily until it reaches point 'b', i.e. side of the sphere as shown in Figure 5.4. Moving from point 'a' across the gap between the sphere electrodes to point 'c', the minimum electric field occurs at the centre of the gap length. This electric field plot agrees with a detailed explanation given in [106]. There is slight difference in E_{max} values between point 'a' and point 'c'. This is due to the electric flux is not fully transferred to the ground electrode, in which some of the electric flux moved to the walls of the pressure vessel (which is also grounded).

According to Howard [107], the electric field at the point of a rod-plane configuration can be assumed to be the same as that given by the formula for the field between a hyperboloidal point-plane electrode, as in Eqn. (5.5).

$$E = \frac{2V}{R \ln (4x/R)} \qquad (5.5)$$

where

R: radius of curvature of the point tip

x: point-to-plane spacing

V: point potential

By using Eqn. 5.2 and Table 5.2, the electric field for rod-plane configuration under a positive impulse in a 1 cm gap can be calculated as,

$$E = \frac{2(41.28\text{kV})}{0.5\text{mm} \ln[\frac{4(1\text{cm})}{0.5\text{mm}}]}$$

$$= 376.8 \text{ kV/cm}$$

From the above calculation, there is an 8.4% difference between calculated value (using Eqn. (5.5)) and E_{max} value from simulation in COMSOL for the rod-plane electrode configuration in a 1 cm gap.

For the sphere gap configuration, a formula given by Greason et a.l [108] can be used to calculate the E_{max}, as shown in Eqn. (5.6).

$$E = 0.9 \frac{V}{d} \frac{(r+d/2)}{r} \qquad (5.6)$$

where

V: potential

r: radii of the spheres

d: surface separation between spheres

By using Eqn. (5.5) and Table 5.2, E_{max} for the sphere gap configuration under a positive impulse in a 1 cm gap can be calculated as

$$E = 0.9 \frac{123.82\text{kV}}{1\text{cm}} \frac{(2.5\text{cm}+1\text{cm}/2)}{2.5\text{cm}}$$

$$= 133.7 \text{ kV/cm}$$

From the above calculation there is 5.8% difference between calculated value (using Eqn. (5.6)) and E_{max} value from simulation in COMSOL for the sphere gap electrode configuration in a 1 cm gap.

It is desirable to calculate the field utilization factor, η for each electrode configuration as depicted in Figure 5.3. The value of field utilization factor will provide a better understanding on the non-uniformity of the gap geometry. Using Eqn. (4.13) and Eqn. (4.14), and by taking applied voltage, V as 1 kV and gap length, g as 1 cm, the field utilization factor, η for each electrode configuration is given in Table 5.1.

Table 5.1: Field utilization factors for each electrode configuration with V = 1 kV

Electrode configuration	E_{max} (kV/cm)	E_{mean} (kV/cm)	Field utilization factor, η
Rod-plane; 1 cm gap	8.34	1.00	0.120
Plane-plane; 1 cm gap	1.31	1.00	0.763
Sphere gap: 1 cm gap	1.15	1.00	0.870

5.3.1 Magnitude of U_{50} and E_{max}

To determine the effects of the electrode configuration, it is essential to fix the gap length on the test, and the gap length, g, is selected to be 1 cm, in order to protect the bushing. Both impulse polarities are then injected, and the up-and-down method was used to determine U_{50} voltage for CF_3I-CO_2 gas mixtures, with at least 20 shots per electrode configuration. The results of the tests are shown in Table 5.2. All values of U_{50} are were used in COMSOL Multiphysics software to determine the corresponding maximum electric field (E_{max}).

As can be seen from Table 5.2, there are some variations in the U_{50} and E_{max} values for all electrode configurations, as well as for both polarities. A clearer view of the U_{50} and E_{max} can be seen in Figure 5.7(a) and Figure 5.7(b), respectively.

Table 5.2: U_{50} and E_{max} of CF_3I-CO_2 mixtures for each electrode configuration with a 1 cm gap at 1.0 bar

Electrode system	Rod-plane		Sphere gap		Plane-plane	
Impulse polarity	Positive	Negative	Positive	Negative	Positive	Negative
U_{50} (kV)	41.28	41.96	123.82	115.58	57.50	55.76
E_{max} (kV/cm)	345	350	142	133	75	73
E_{max}/E_{mean}	8.36	8.34	1.145	1.15	1.30	1.31
$E_{normalised}$ (cm^{-1})	8.36	8.34	1.145	1.15	1.30	1.31

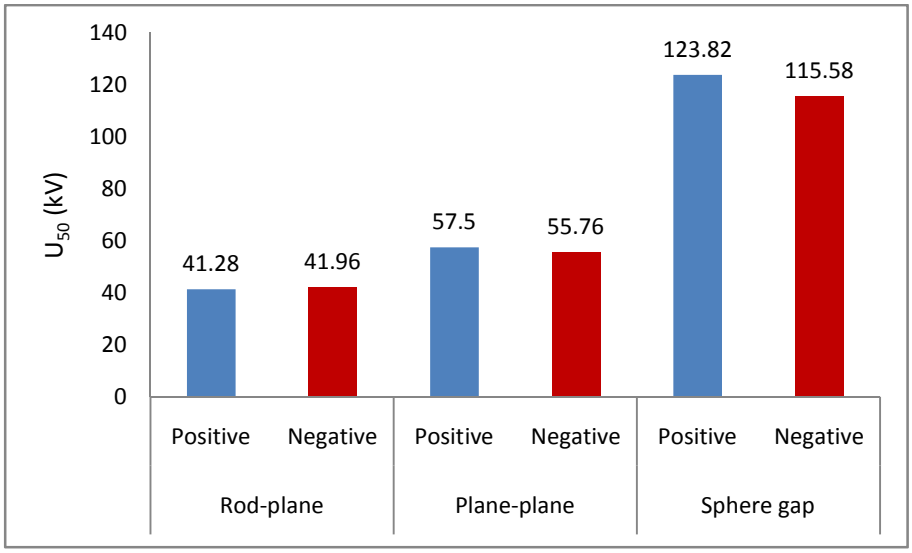

(a) U_{50}

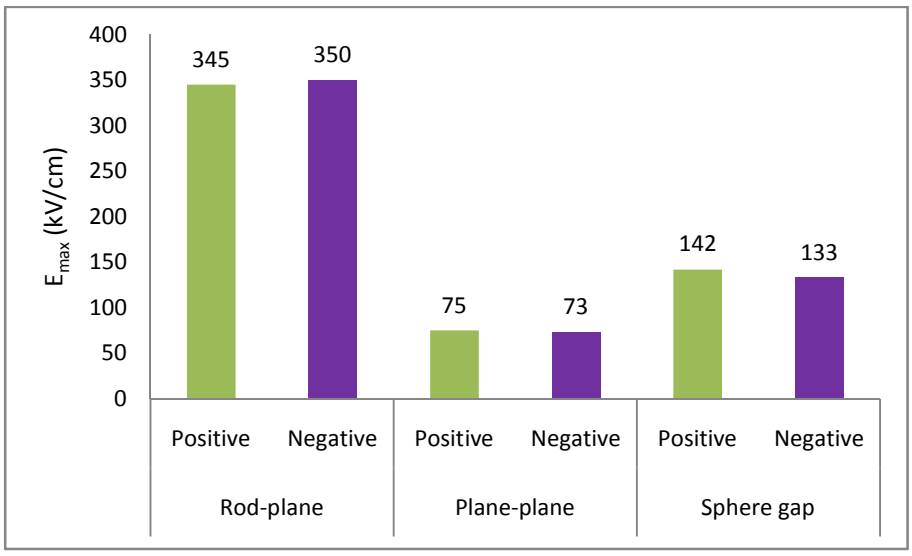

(b) E_{max}

Figure 5.7: Effects of electrode configuration on CF_3I-CO_2 (30%-70%) mixtures under positive and negative impulse polarities in a 1 cm gap

There is not much difference in the U_{50} values between positive and negative impulse polarity. This is mainly because the gap is only 1 cm. A bigger gap will provide a bigger difference in U_{50} as will be reported in the next section. This is due to the fact that a bigger gap provides a more non-uniform electric field between the electrodes. For negative impulses, there is only a 1.6% increase for rod-plane, 3.0% decrease for plane-plane, and 6.65% decrease in sphere gap configurations. The difference for E_{max} appears to be similar for all electrode configurations, which are at a 1.45% increase for rod-plane, 2.7% decrease for plane-plane, and 6.34% decrease for sphere gap. The differences in E_{max} seem to be related to differences in U_{50}.

A comparison can be made with the investigations carried out by Katagiri et al. [40] and Toyota et al. [46] as discussed in Chapter 2. Although the U_{50} value for CF_3I-CO_2 (30%-70%) gas mixtures in this study (41.28 kV) is a little bit higher than that pure CF_3I (35 kV) reported by Toyota, it is still acceptable since Toyota used a very fast rise time voltage waveform, i.e. 16 ns as compared with 1.2 μs for lightning impulse. U_{50} for SF_6, on the other hand, is given as 47 kV in [46].

Although the rod-plane configuration has the lowest U_{50}, it has the highest E_{max}. The lowest values of E_{max} occur in the plane-plane electrode and the highest stress location for this configuration, which reflects the $E_{max,}$ is at the edge of the plane electrode, as has been shown in Figure 4.17.

The relationship between U_{50}, E_{max} and field utilization factor with related electrode for both positive and negative impulse polarities are shown in Figure 5.8 and Figure 5.9.

As observed in Figure 5.8 and Figure 5.9, breakdown voltage initiation is not proportional to E_{max}. Maximum magnitude of U_{50} can be obtained with the sphere gap electrode configuration, i.e. highly uniform electric field, but with the rod-plane

electrode system, the highest magnitude of E_{max} is obtained with the lowest U_{50}. In short, the rod-plane electrode system will produce the highest electric field followed by plane-plane and the sphere gap electrode systems. In this investigation, U_{50} increases slightly with field utilization factor until around 0.8 (plane-plane electrode configuration), and then increases significantly towards higher field utilization factor, i.e. highly uniform electric field.

Also, for a low field utilization factor, as is the case with the rod-plane electrode configuration, U_{50} under negative lightning impulse polarity is higher than under positive polarity. As the field becomes more uniform, i.e. higher field utilization factor, U_{50} under positive lightning impulse polarity is higher than that under negative polarity. More significant results on the differences in U_{50} according to the impulse polarity are presented in section 5.4.

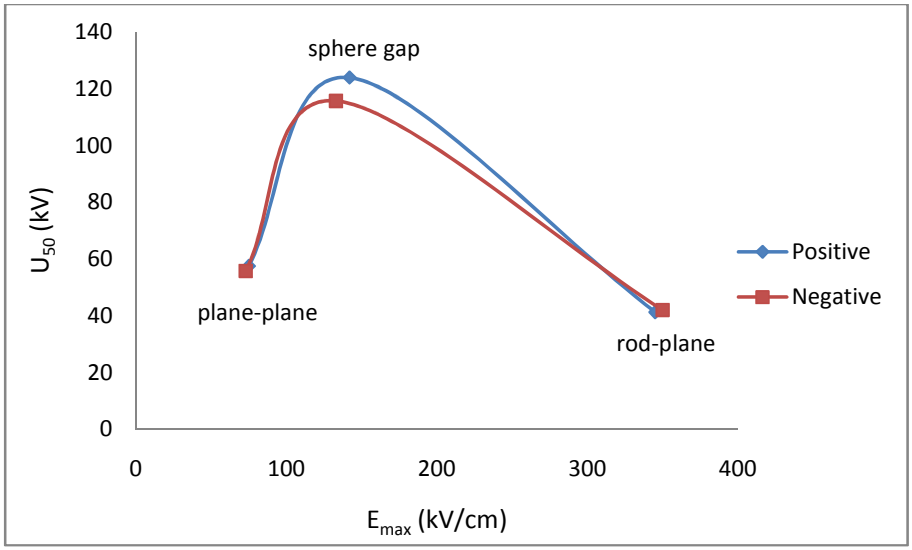

Figure 5.8: Relationship between U_{50} and E_{max} according to the electrode systems of CF_3I-CO_2 (30%-70%) gas mixture under positive impulse polarities

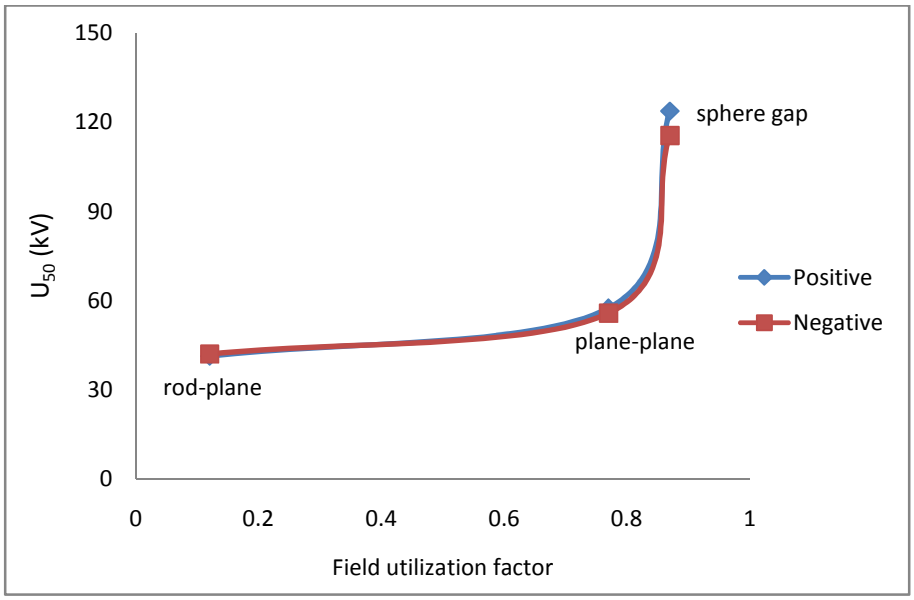

Figure 5.9: Effects of field utilization factor on U_{50} of CF_3I-CO_2 (30%-70%) gas mixture under positive impulse polarities

5.3.2 *V-t* Characteristics

Apart from investigating U_{50} and E_{max} values to get an overview of insulation performance of CF_3I-CO_2 gas mixtures, another characteristic to be considered is the voltage-time (*V-t*) characteristics, as has been explained in section 2.6.2. Every time a breakdown occurs within the CF_3I-CO_2 gas mixture, the voltage and time at the moment of breakdown are recorded. The *V-t* characteristic curves for these tests are shown in Figure 5.10.

As can be seen in Figure 5.10, *V-t* characteristics reflect the U_{50} values of CF_3I-CO_2 gas mixtures. The higher the *V-t* characteristic curve is, the higher the value of U_{50} will be. An interesting point is that the *V-t* characteristic for a rod-plane configuration under a positive impulse is concentrated around the very early period, less than 2 µs. This can be observed through the experimental works where most of the breakdown occurs around the peak voltage of the lightning impulse, which is between 1-2 µs.

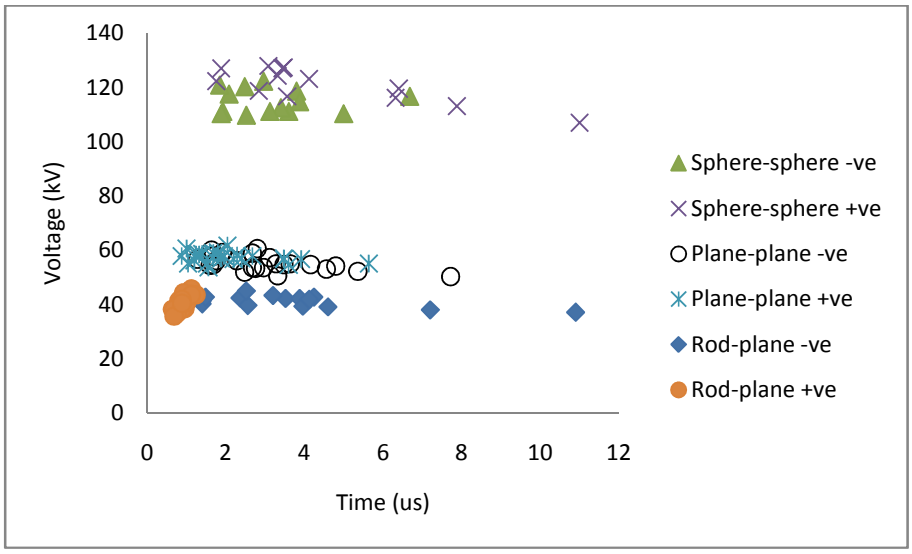

Figure 5.10: *V-t* characteristics for various electrode configurations; 1 cm gap

Apart from the rod-plane configuration under a positive impulse, all the *V-t* characteristics have almost flat curves. This is true as has been reported by Takuma [109] with a gap, a small electrode area, and lower pressures where a nearly flat *V-t* characteristic will be observed. These flat *V-t* curves also agree with the investigations by Hoshina et al. [110] which focused on CO_2 and N_2 gases.

5.4 Effects of Gap Length

There are many designs of gas-insulated switchgears (GIS) available in high voltage equipment. Which design is chosen depends on factors such as voltage level and type of insulation. A publication by Jones [111], on behalf of the CIGRE Task Force of Working Group B3-02, reported that future developments will be designed so that the GIS will be:

i. more compact
ii. simpler with fewer components
iii. increase in performance and reliability
iv. cheaper

SF_6 is expected to be replaced by other types of insulation gases in the future. It is essential to investigate all design possibilities for the alternative gases in order to provide a basic knowledge on how the behaviour of each given gas in any configuration. For that reason, with a view on various GIS designs, tests on electrode configurations as in the previous section have been carried out to examine the effects of gap length on the insulation behaviour of CF_3I-CO_2 mixtures, in particular, with 30%-70% ratios. This gap length also affects the field utilization factor. Normalised electric field, $E_{normalised}$ can also be calculated, as shown by Eqn. (5.7)

$$E_{normalised} = \frac{E_{max}}{U_{50}} \qquad (5.7)$$

Due to the limitation of the bushing, as explained in section 3.6, the highest voltage level for lightning impulse is approximately 170 kV at the peak [82]. Also, based on the results from the previous section, each electrode configuration will correspond to a different level of U_{50} for the same gap length. As a result, gap length for the rod-plane electrode configuration can go further up when compared to plane-plane and sphere gap configurations, but all will be limited to the defined voltage limitations. In these tests, the rod-plane configuration will have a maximum gap length of 5 cm, while for plane-plane and sphere gap configuration, the gap will be 3 cm and 1.5 cm, respectively.

5.4.1 Rod-plane Electrode Configuration

5.4.1.1 Magnitude of U_{50} and E_{max}

As previously mentioned, the highest gap length that can be achieved is through using a rod-plane electrode configuration. Table 5.3 shows the results for U_{50} and the associated E_{max} when a CF_3I-CO_2 gas mixture is subject to both positive and negative

lightning impulses within the mentioned electrode configuration. The results in Table 5.3 can be plotted to provide a clearer view of the behaviour of U_{50} and E_{max} under the specified test conditions as shown in Figure 5.11.

Table 5.3: U_{50} and E_{max} for CF_3I-CO_2 mixtures (30%-70%) in rod-plane gap

Gap length (cm)	Positive impulse			Negative impulse		
	U_{50} (kV)	E_{max} (kV/cm)	$E_{normalised}$ (cm^{-1})	U_{50} (kV)	E_{max} (kV/cm)	$E_{normalised}$ (cm^{-1})
1.0	41.28	345	8.36	41.96	350	8.34
2.0	55.91	385	6.89	66.09	456	6.90
3.0	63.41	399	6.29	94.30	593	6.29
4.0	70.08	417	5.95	112.04	667	5.95
5.0	74.69	429	5.74	124.62	717	5.75

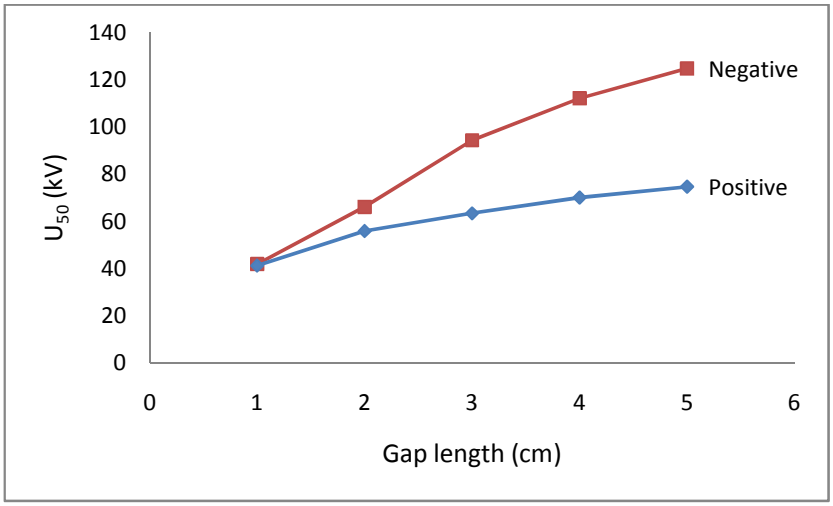

(a) U_{50}

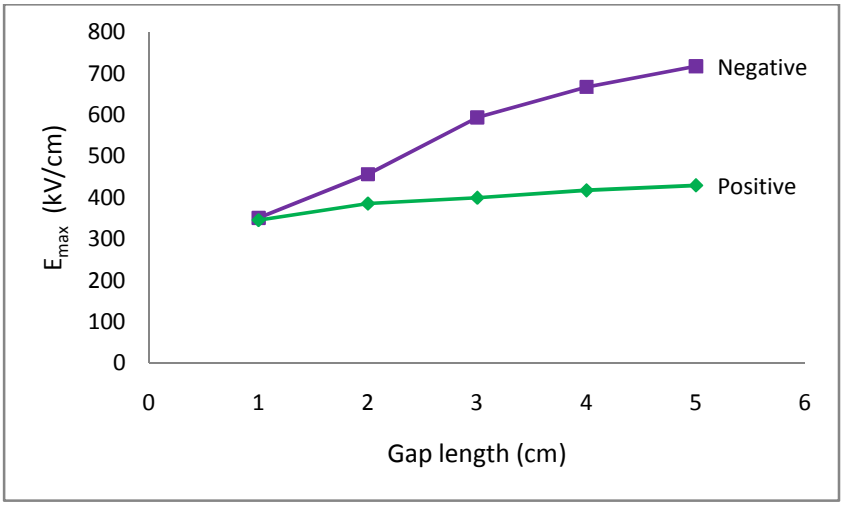

(b) E_{max}

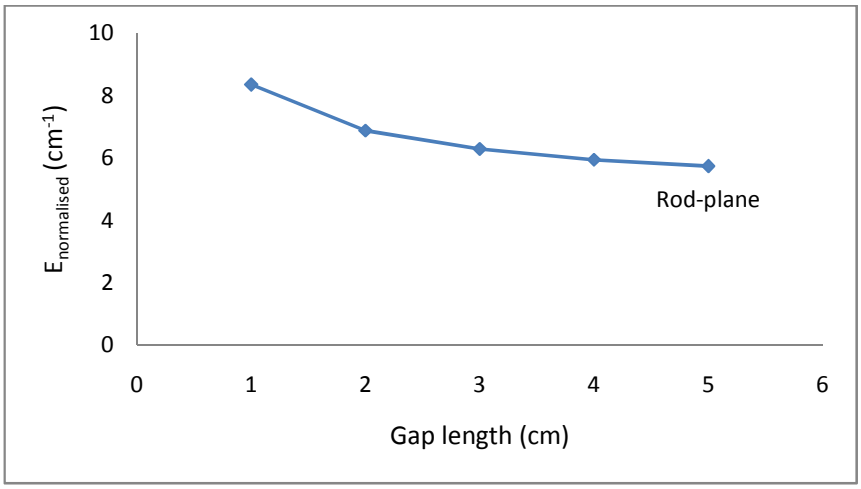

(c) $E_{normalised}$

Figure 5.11: Effects of gap length on CF_3I-CO_2 (30%-70%) gas mixtures in rod-plane electrode configuration under positive and negative impulse

As can be seen in Figure 5.11, at a 1 cm gap, there is not much difference in the U_{50} of the CF_3I gas mixture, particularly in smaller gaps. When the gap length between the electrodes is increased the U_{50} for both impulse polarities also increases. However, under a negative impulse, the increment in U_{50} is quite significant as compared to that under a positive impulse. At 5 cm, under a negative impulse, the U_{50} has increased to almost 3 times compared to U_{50} at 1 cm. Meanwhile, under a positive impulse, the increment is about 1.8 times. Although U_{50} and E_{max} increase over gap length, $E_{normalised}$, on the other hand, decreases with gap length. The trend is identical for both positive and negative polarities.

Generally, it can be said that for the rod-plane electrode configuration, the U_{50} voltage under a negative impulse voltage is higher than U_{50} under a positive impulse voltage. As discussed by Loeb and Kip [112], breakdown in the rod-plane electrode is due to the streamers. In negative streamers, the space charge build up impedes the negative avalanche, while the space charge in positive streamers propagates toward the

cathode. Due to this process, negative streamers require higher electric fields (and hence, higher voltages) than positive streamers. This breakdown mechanism which includes the role of the space charge has also been explained in detail by Works and Dakin [113].

5.4.1.2 *V-t* Characteristics

V-t characteristics for CF_3I-CO_2 gas mixtures with a 30%-70% gas mixture ratio under a rod-plane configuration are shown in Figure 5.12(a) and Figure 5.12(b) for both positive and negative impulses respectively.

As depicted in Figure 5.12, it can be seen that *V-t* characteristics for a given gap spacing under a negative impulse are higher than those under a positive impulse, particularly for bigger gap lengths. From these characteristics, it can be observed that under a positive impulse most of the sparkovers occur in an earlier parts of the lightning impulse wavetail. The breakdown under a negative impulse can take longer, up to 13 µs, as shown in Figure 5.12(b). However, under a positive impulse, most of the breakdown occurs in less than 4 µs with few occurrences of sparkovers, only those at around 6 µs.

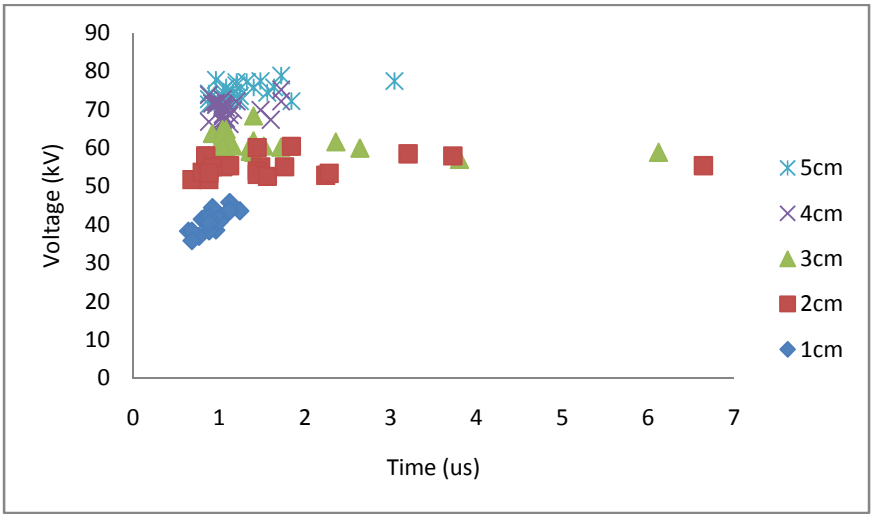

(a) Positive polarity

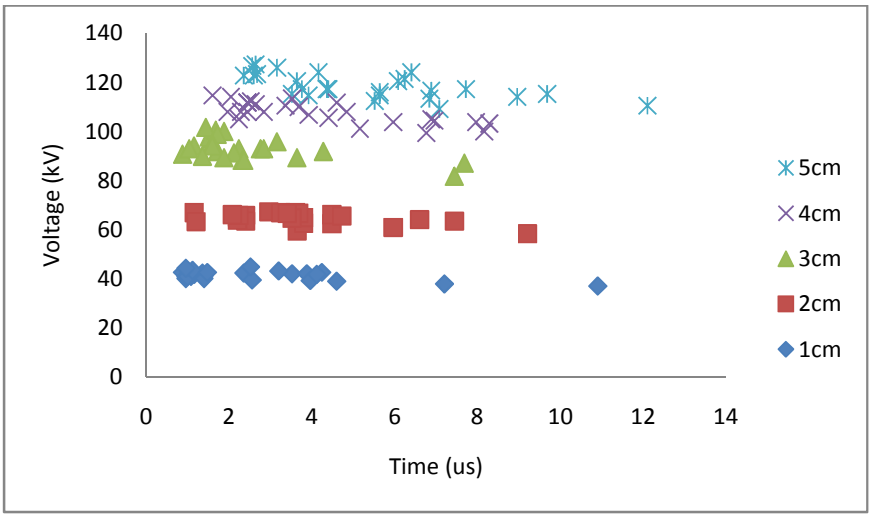

(b) Negative polarity

Figure 5.12: *V-t* characteristics for CF_3I-CO_2 (30%-70%); rod-plane electrode configuration

5.4.2 Plane-plane Electrode Configuration

5.4.2.1 Magnitude of U_{50} and E_{max}

In the plane-plane electrode configuration, it is expected that higher voltages are required in order for the CF_3I-CO_2 gas mixtures to breakdown across a gap length, when compared to a rod-plane configuration. It is essential to limit the gap length carefully so that the voltage is kept low in order to protect the bushing. For this reason, the gap length in this test is limited to 3 cm, and the results are shown in Table 5.4.

Table 5.4: U_{50} and E_{max} for CF_3I-CO_2 mixtures (30%-70%) in a plane-plane gap

Gap length (cm)	Positive impulse			Negative impulse		
	U_{50} (kV)	E_{max} (kV/cm)	$E_{normalised}$ (cm^{-1})	U_{50} (kV)	E_{max} (kV/cm)	$E_{normalised}$ (cm^{-1})
1.0	57.50	75	1.30	55.76	73	1.31
2.0	112.98	98	0.87	98.66	85	0.86
3.0	161.27	117	0.73	133.76	97	0.73

To compare the results between positive impulses with negative impulses easily, U_{50} and E_{max} curves are plotted in relation to gap length, as shown in Figure 5.13(a) and Figure 5.13(b) respectively.

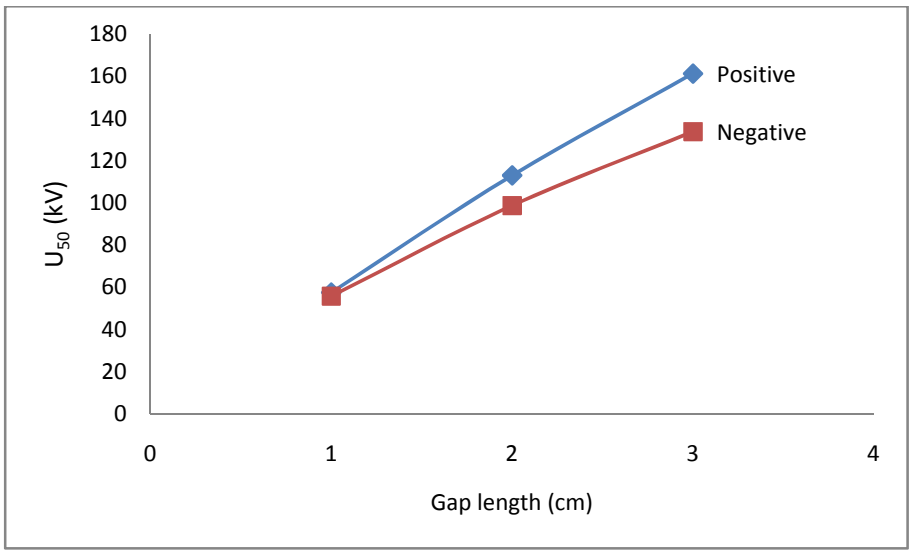

(a) U_{50}

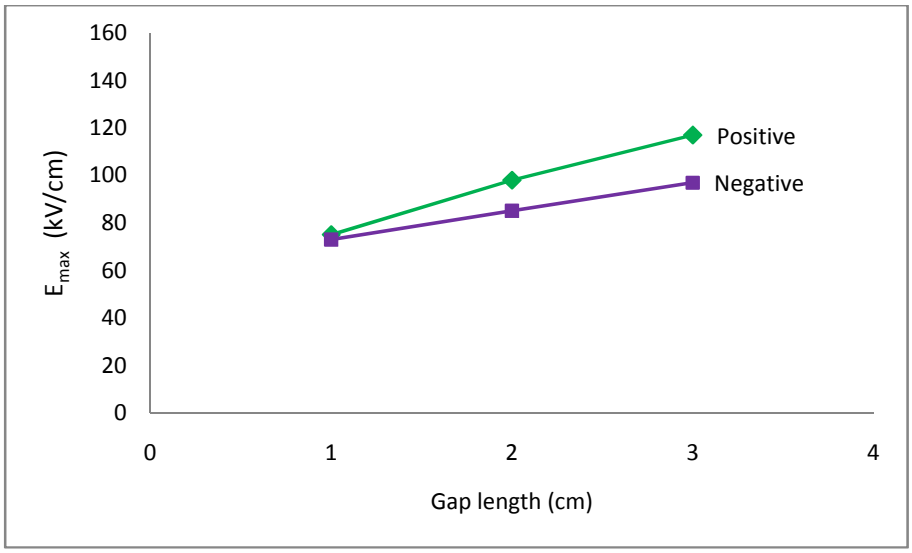

(b) E_{max}

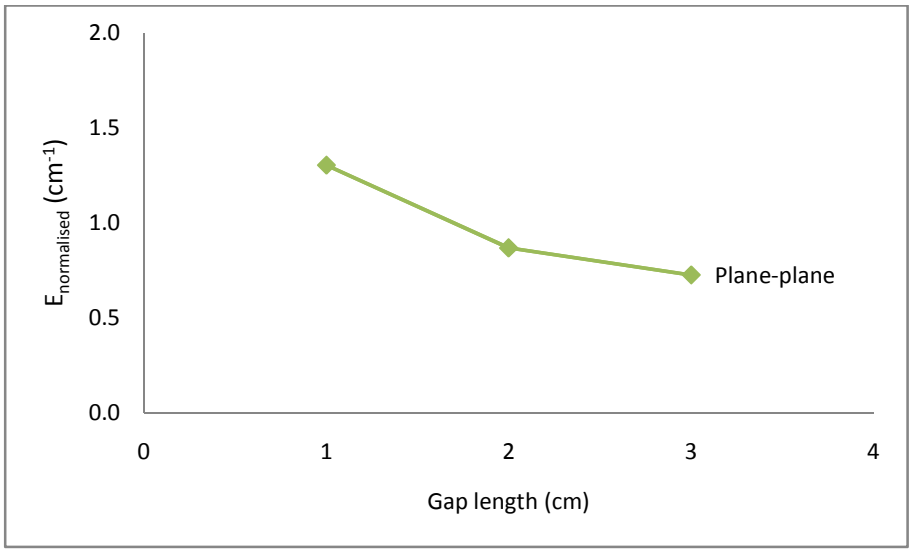

(c) $E_{normalised}$

Figure 5.13: Effects of gap length on CF_3I-CO_2 (30%-70%) mixtures in a plane-plane electrode configuration under positive and negative impulses

A closer investigation of the U_{50} characteristic of a plane-plane electrode configuration will now be explored. The behaviour is opposite from those that observed in a rod-plane configuration. In this plane-plane configuration, U_{50} under a positive impulse is a little bit higher than under a negative impulse, although for a 1 cm gap, the difference is very small, which has been reported in section 5.3. With a 1 cm gap, there is only a 3% difference between both polarities, and the difference increases with gap length, 12.7% and 29% for 2 cm and 3 cm gaps respectively. Also, in this study, U_{50} can be seen to increase quite linearly with gap length in a plane-plane configuration, up to 3 cm. Under a positive impulse, U_{50} increased to 2.8 times from a 1 cm gap to a 3 cm gap, and under negative impulse, the increment is approximately 2.4 times. As in rod-plane electrode configuration, $E_{normalised}$ in plane-plane electrode configuration decreases over gap length, with a same trend for both positive and negative polarities.

The trends in U_{50} curves reflect the behaviour in E_{max} curves, as can be seen in Figure 5.13. E_{max} is observed to increase linearly with gap length, although the increment is not as much as in U_{50}. For $E_{max,}$ the increment from a 1 cm to 3 cm gap is 1.56 times under a positive impulse and just 1.3 times under a negative impulse.

5.4.2.2 *V-t* Characteristics

V-t characteristics for CF_3I-CO_2 gas mixtures with a 30%-70% gas mixture ratio under plane-plane configuration are shown in Figure 5.14(a) and Figure 5.14(b) for both positive and negative impulses, respectively, to show the breakdown behaviour of the gas mixtures under such test condition.

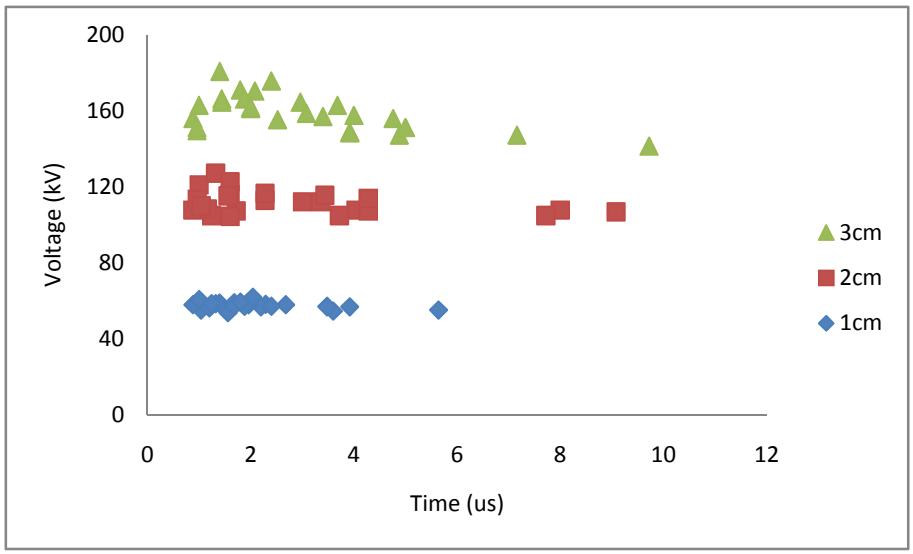

(a) Positive polarity

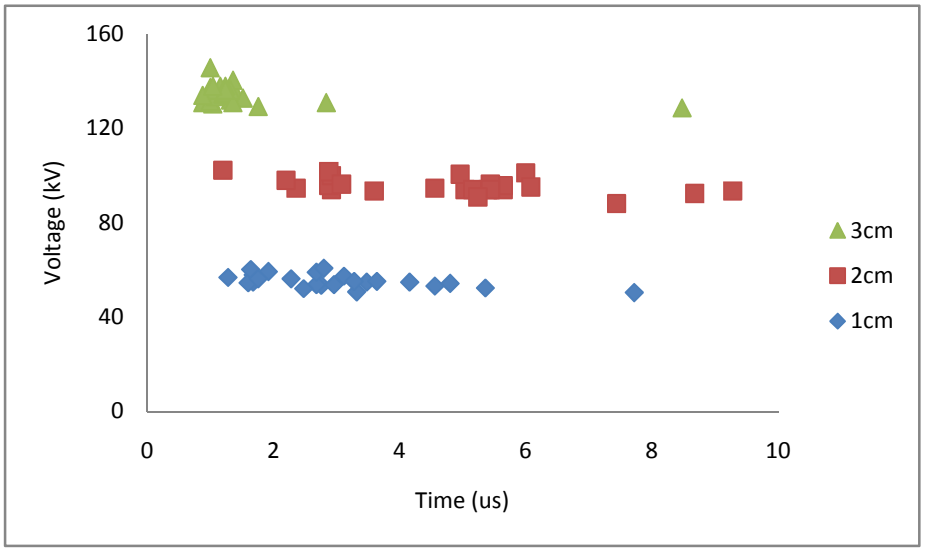

(b) Negative polarity

Figure 5.14: *V-t* characteristics for CF_3I-CO_2 (30%-70%); plane-plane electrode configuration

In contrast with the rod-plane electrode configuration, breakdown instants in the plane-plane configuration can be observed to be more distributed along the wavetail of the lightning impulse with both polarities having sparkovers at around 10 μs, as depicted in Figure 5.14. An almost flat *V-t* characteristic can be observed for a 1 cm gap for both polarities, while for a 3 cm gap the *V-t* characteristic tends to curve downward. This might be due to the waveshape of the lightning impulse itself. For a large gap length, a higher magnitude (and hence peak value) of lightning impulse is needed for breakdown, and the wavetail shape for such lightning impulse is more curved downward as compared to lower magnitude ones. Since most of breakdowns occurred along the wavetail, the resultant *V-t* characteristic tends to follow the curve.

5.4.3 Sphere Gap Electrode Configuration

5.4.3.1 Magnitude of U_{50} and E_{max}

In a sphere-sphere gap electrode configuration (refer Figure 5.3(c)), further reductions on the gap length need to be achieved in order to keep the impulse voltages at safe levels. In this configuration, only two gap lengths are covered, the 1cm and 1.5 cm. The results are shown in Table 5.5.

Table 5.5: U_{50} and E_{max} of CF_3I-CO_2 mixtures (30%-70%) in a sphere gap at 1 bar

Gap length (cm)	Positive impulse			Negative impulse		
	U_{50} (kV)	E_{max} (kV/cm)	$E_{normalised}$ (cm^{-1})	U_{50} (kV)	E_{max} (kV/cm)	$E_{normalised}$ (cm^{-1})
1.0	123.82	142	1.15	115.58	133	1.15
1.5	161.99	135	0.83	148.76	124	0.83

An interesting behaviour in U_{50} and E_{max} can be seen from the above table, as E_{max} is slightly decreased, albeit U_{50} is increased with gap length. This holds true for both positive and negative polarities, as depicted in Figure 5.15(a) and Figure 5.15(b), respectively.

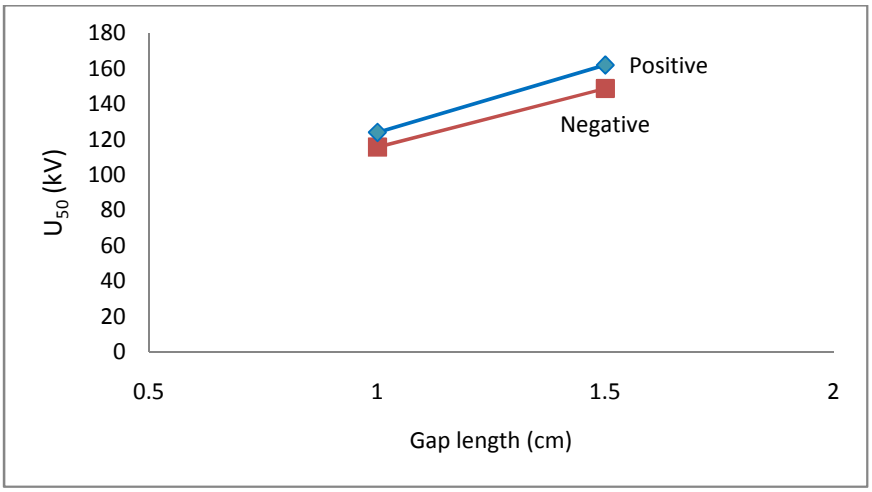

(a) U_{50}

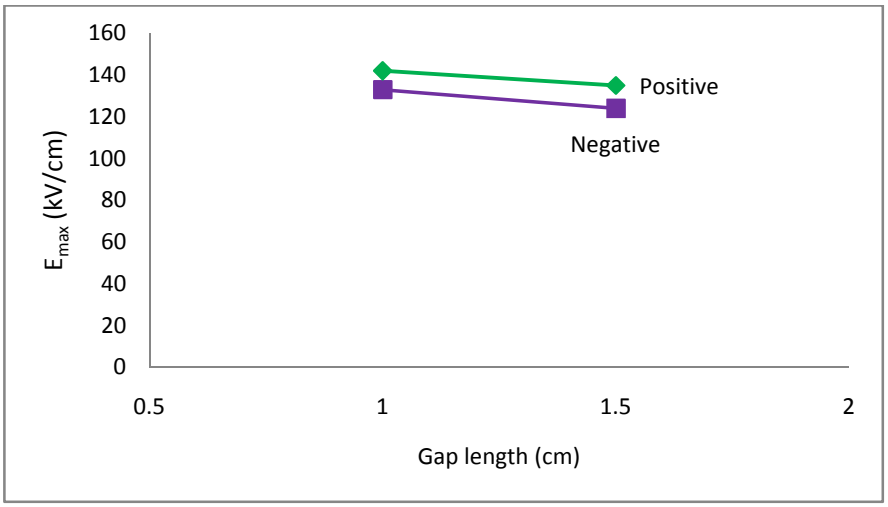

(b) E_{max}

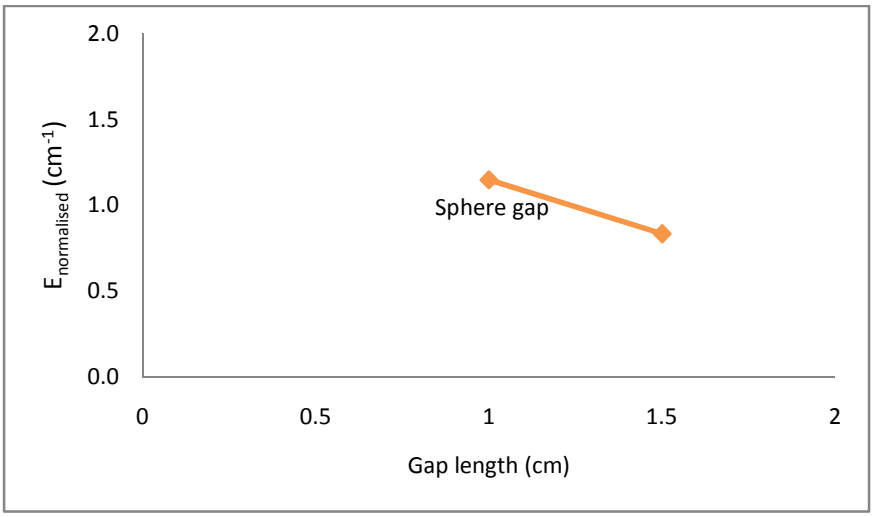

(c) $E_{normalised}$

Figure 5.15: Effects of gap length on CF_3I-CO_2 (30%-70%) mixtures in a sphere gap electrode configuration under positive and negative impulses

In the sphere gap configuration, the differences in U_{50} between the positive impulse and the negative impulse are about the same for both gap lengths, which are 6.7% and 8.2% for a 1 cm and 1.5 cm gap respectively. Meanwhile, for $E_{max,}$ the differences are 6.3% for a 1 cm gap and 8.1% for a 1.5 cm gap, which are almost the

same as in U_{50}. Compared to E_{max}, U_{50} increased significantly as E_{max} decreased slightly with gap lengths, in which for positive impulse, an increase in U_{50} by 1.3 times corresponds to a decrease in E_{max} by 0.95 times.

5.4.3.2 *V-t* Characteristics

Breakdown behaviour of a CF_3I-CO_2 (30%-70%) gas mixture can be observed by observing the results in the *V-t* characteristics, as shown in Figure 5.16 for both positive and negative impulses.

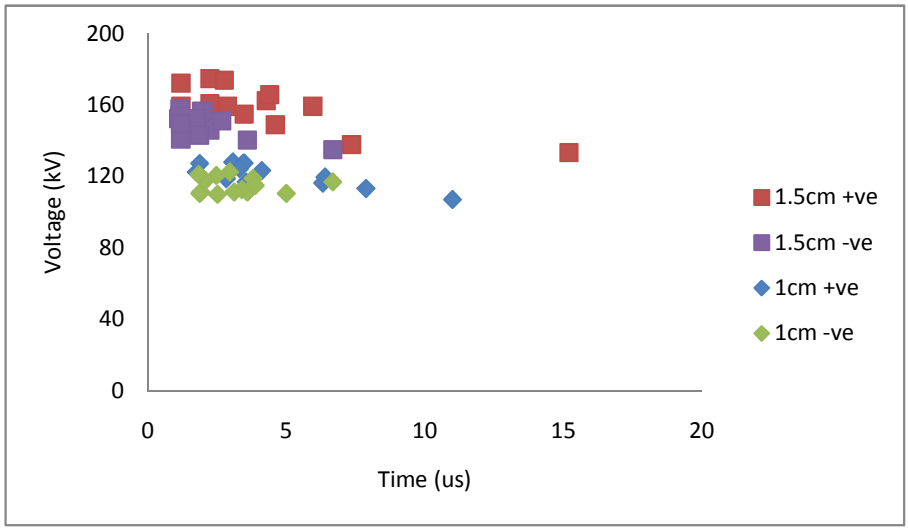

Figure 5.16: *V-t* characteristics for CF_3I-CO_2 (30%-70%); sphere gap electrode configuration for positive impulse and negative impulses

From Figure 5.16, breakdown of a CF_3I-CO_2 (30%-70%) gas mixture in a sphere gap configuration is more distributed along the wavetail of impulse lightning, particularly under a positive impulse, as compared to those in the rod-plane configuration. One breakdown did even occur at 15 μs in a 1.5 cm gap.

Considering all electrode configurations, the effects of gap length are summarized in Figure 5.17.

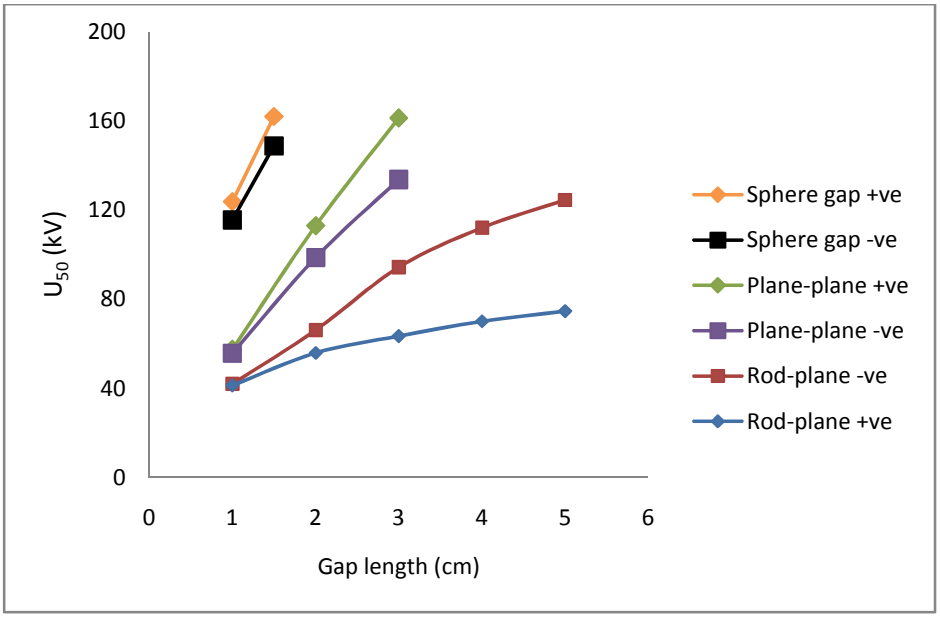

(a) U_{50}

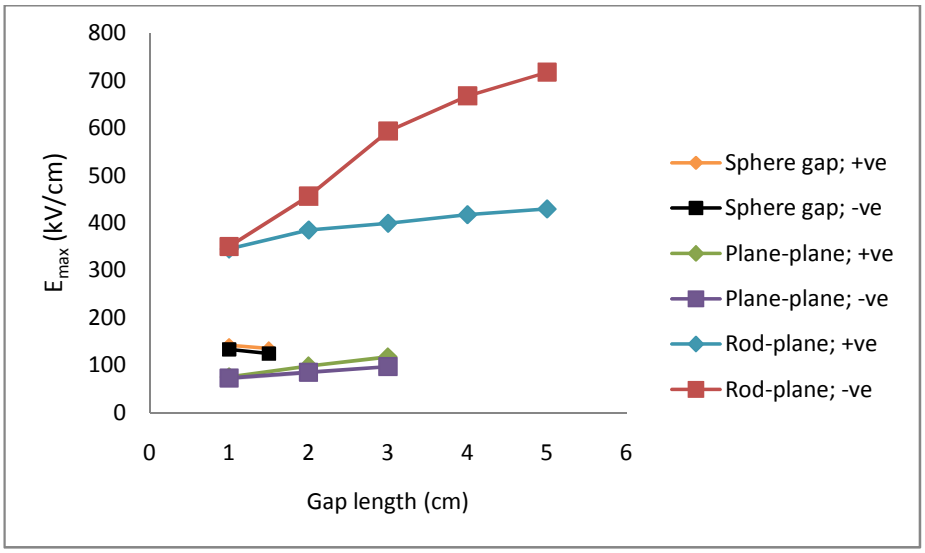

(b) E_{max}

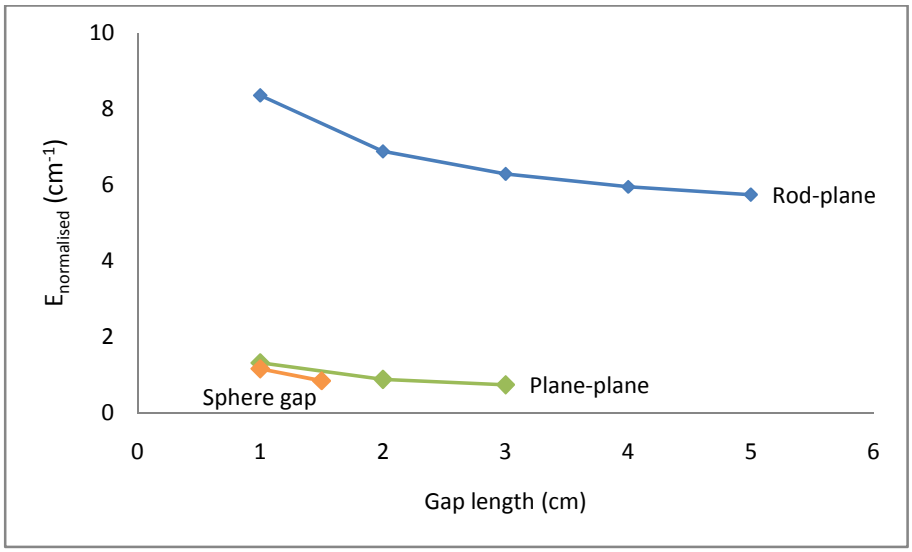

(c) $E_{normalised}$

Figure 5.17: Curves for CF_3I-CO_2 (30%-70%) in all electrode configurations under both positive and negative lightning impulses in relation with gap length

Figure 5.17 shows that under both positive and negative lightning impulse polarities, E_{max} is less affected by gap length when compared to U_{50}, with an exception for rod-plane configurations under negative impulses in which E_{max} increases significantly with gap length. In all electrode configurations, E_{max} increases with gap length, except in a sphere gap configuration whereby E_{max} decrease slightly for both positive and negative impulse polarities. Although E_{max} decreases with gap length for this configuration, it has the highest increment of U_{50} for such a small gap increase. In a sphere gap configuration an increase of 50% in gap length produces an increase of 31% in U_{50} under a positive impulse and 29% under negative impulse polarity. $E_{normalised}$, on the other hand, decreases over gap length for all electrode configurations. The trends are identical for each specific electrode system for both positive and negative polarity.

Although the rod-plane configuration has the highest E_{max} values, the U_{50} under positive impulse is the least affected with gap length, with only an 81% increment with

a 400% increment in gap length. The mechanism of breakdown does not over dependant on gap length. This has been discussed by Niemeyer et al. [114] where several leader channel development in electronegative gases can be achieved with different electrode configurations.

As this study is very unique for a given electrode system and gap length, it is very hard to make comparison (especially like for like comparison) with other available published investigation on other gases, particularly SF_6. However, the same investigation in this study can be replicated to compare with SF_6, air, or other gases, which include other CF_3I gas mixtures.

5.5 Conclusion

From this study, it can be concluded that electrode geometry, which includes electrode configuration and gap length, plays a big role in determining U_{50} values for CF_3I-CO_2 gas mixtures. A big difference in U_{50} between positive impulses and negative impulses can be seen under a low field utilization factor or a very non-uniform field, as in the rod-plane electrode configuration, particularly for a large gap length.

As it is important to investigate U_{50} behaviour of CF_3I-CO_2 mixtures under different electrode configurations, this study found that for electrode configurations with a field utilization factor of 0.8 and above, the gas mixture's U_{50} can be increased significantly. Although the U_{50} values are lower in a very non-uniform field, the gas mixture is able to withstand the highest E_{max}.

Behaviour of lightning impulse breakdown in CF_3I-CO_2 can be seen in *V-t* characteristics. Early breakdowns are very likely to occur in rod-plane electrode configurations under a positive impulse lightning.

CHAPTER 6: BREAKDOWN PROPERTIES OF CF_3I AND ITS MIXTURES UNDER LIGHTNING IMPULSE: EFFECTS OF GAS PRESSURE AND CF_3I CONTENT

6.1 Introduction

Several factors affecting CF_3I-CO_2 gas mixtures have been discussed in the previous chapter. These include the effects of gap length, impulse polarity, and electrode configuration. Equally important is to explore the effects of the gas pressure and other mixture ratios of CF_3I-CO_2 on breakdown characteristics.

Earlier studies in gas mixtures, especially the ones involving SF_6, have been carried out by Sharbaugh and Watson [115] in 1964, and Mulcahy [116] in 1966. While Sharbaugh and Watson were working on mixtures of SF_6 with perfluorocarbon, Mulcahy worked on SF_6-air mixtures. However, both were looking into various pressures of the gas mixtures. Another example of investigation on SF_6 mixture has been carried out by MacGregor et al. [117] in 1989, looking at SF_6-Helium mixture for repetitive switching applications.

It is common to use SF_6 at higher pressures, especially in gas insulated circuit breakers, as it is understood that more gas pressure will provide better insulation characteristics. Examples of such properties can be seen in the Elimsan Group gas circuit breaker, which normally has 3 bar (abs) of SF_6, but can go up to 5 – 6 bar [118], or the ABB Limited version that is using 7 bar (abs) in an indoor live tank SF_6 circuit breaker [119]. For this reason, it is essential to investigate the effects of pressure variations on insulation strength of the CF_3I-CO_2 mixtures.

6.2 *Effect of Gas Pressure*

In an effort to investigate the effect of gas pressure on the insulation performance of CF_3I-CO_2 gas mixtures used in this study, only the rod-plane electrode configuration is used for that purpose. This is to ensure that, for all gas pressures, tests that are carried out on the gap length between the electrodes can be extended to the maximum allowable length, while keeping the impulse voltage level at a safe value for the bushing.

As for this test, apart from 1.0 bar (abs) of CF_3I-CO_2 pressure which has been used in previous studies, the pressure is increased to 1.5 bar (abs) and 2.0 bar (abs). According to Dalton's Law as in Eqn. (5.1), the partial pressure of each CF_3I and CO_2 gas mixture is shown in Table 6.1, placed according to the corresponding total pressure of the gas mixtures.

Table 6.1: Partial pressures of CF_3I and CO_2 gases for mixture ratio of 30%-70%

Total Pressure (bar [abs])	Partial Pressure of CF_3I (bar [abs])	Partial Pressure of CO_2 (bar [abs])
1.0	0.30	0.70
1.5	0.45	1.05
2.0	0.60	1.40

6.2.1 Magnitude of U_{50} and E_{max}

Further tests were carried out with both positive and negative impulse polarities in a rod-plane electrode configuration, and the results are shown in Table 6.2. The corresponding E_{max} value for each U_{50} is shown in Table 6.3, while Table 6.4 shows the $E_{normalised}$ values. The results are plotted in Figure 6.1, Figure 6.2, Figure 6.3 and Figure 6.4. These figures show the curves of U_{50}, E_{max} and $E_{normalised}$ for all pressures.

Table 6.2: U_{50} for CF_3I-CO_2 (30%-70%) Mixtures for Various Pressures

	U_{50} (kV)					
Pressure	**1.0 bar**		**1.5 bar**		**2.0 bar**	
Gap length (cm)	**Positive**	**Negative**	**Positive**	**Negative**	**Positive**	**Negative**
1	41.28	41.96	51.06	52.94	64.79	67.23
2	55.91	66.09	66.47	83.02	75.03	96.69
3	63.41	94.30	74.81	108.68	81.74	124.95
4	70.08	112.04	79.04	127.59	88.47	137.03
5	74.69	124.62	84.99	143.84	90.47	149.79

Table 6.3: E_{max} for CF_3I-CO_2 (30%-70%) Mixtures for Various Pressures

	E_{max} (kV/cm)					
Pressure	**1.0 bar**		**1.5 bar**		**2.0 bar**	
Gap length (cm)	**Positive**	**Negative**	**Positive**	**Negative**	**Positive**	**Negative**
1	345	350	426	442	541	561
2	385	456	458	572	517	667
3	399	593	471	684	514	786
4	417	667	471	760	527	816
5	429	717	489	827	520	861

Table 6.4: $E_{normalised}$ for CF_3I-CO_2 (30%-70%) Mixtures for Various Pressures

	$E_{normalised}$ (cm^{-1})					
Pressure	**1.0 bar**		**1.5 bar**		**2.0 bar**	
Gap length (cm)	**Positive**	**Negative**	**Positive**	**Negative**	**Positive**	**Negative**
1	8.36	8.34	8.34	8.35	8.35	8.34
2	6.89	6.90	6.89	6.89	6.89	6.90
3	6.29	6.29	6.30	6.29	6.29	6.29
4	5.95	5.95	5.96	5.96	5.96	5.95
5	5.74	5.75	5.75	5.75	5.75	5.75

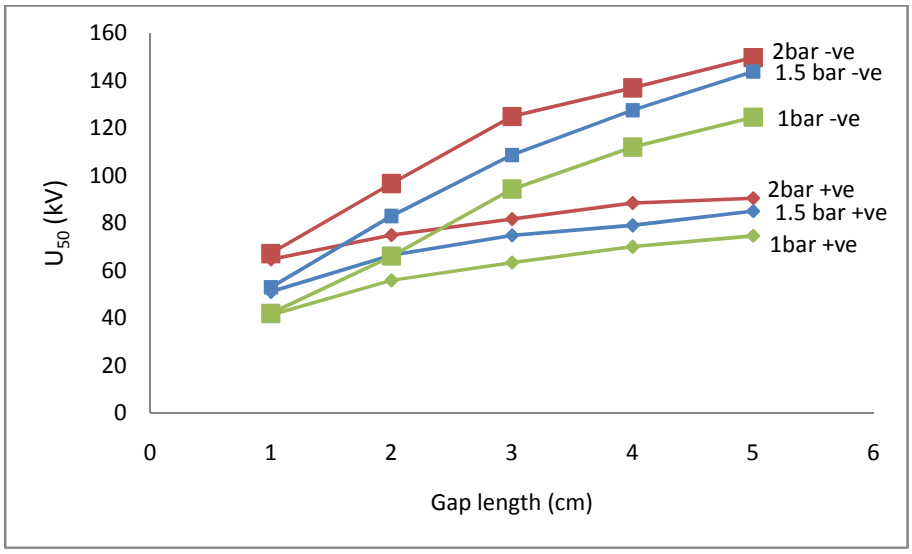

(a) U_{50}

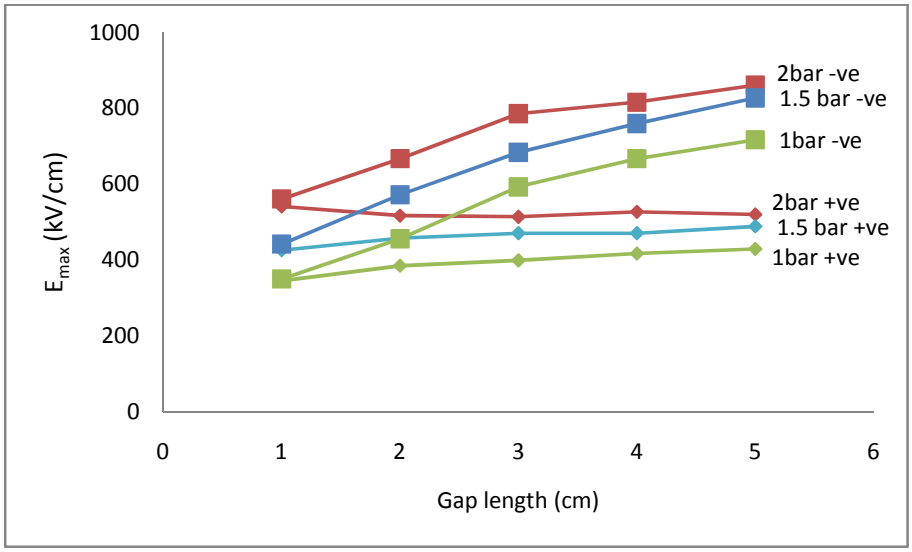

(b) E_{max}

Figure 6.1: Curves for various pressures in relation to gap length

Referring to Figure 6.1(a), as expected under a rod-plane configuration, U_{50} for the negative impulse is much higher than for the positive impulse. This is true for all pressures. It can be said that the U_{50} increases with the pressure of the CF_3I-CO_2 gas mixture. Careful examination of the difference between 1.0 bar (abs) with 2.0 bar (abs)

under a negative impulse reveals that there is an almost constant increment of U_{50} with pressure for all the gap lengths involved. An increment of 31 kV in U_{50} can be calculated for 2 and 3 cm gaps, whereas there is an increment of 25 kV for the remaining gap lengths.

However, under the positive impulse, the relative increase with pressure in U_{50} is seen to decrease from 1 cm to 5 cm, with 23.5 kV at 1 cm, 19 kV at 2 cm, and only 16 kV at 5cm. Generally, it can be said that U_{50} curves for a CF_3I-CO_2 (30%-70%) mixture in relation to gap length, under a rod-plane electrode configuration, are the same for a pressure of 1 – 2 bar.

Since U_{50} increases significantly with gap length under a rod-plane configuration (negative impulse polarity), which is true for all pressures studied, E_{max} will also be increased according to U_{50} depicted in Figure 6.1(b). From 1 cm to 5 cm, the increases in E_{max} are 367 kV/cm for 1.0 bar, 385 kV/cm for 1.5 bar, and 300 kV/cm for 2.0 bar. Considering the increase in E_{max} in terms of percentage provides more interesting results: At 1.0 bar of pressure, an increment of 105% in E_{max} can be calculated, whereas for 1.5 and 2.0 bar, there are 87% and 53% increments in E_{max} respectively. With this information, it can be noted that for 1.5 bar and from 1 cm to 5 cm gap, the increment in the absolute value of E_{max} is higher than at 1.0 bar. However, in terms of percentage, the increment is lower than that of 1.0 bar.

Under a positive impulse, E_{max} curves are almost flat throughout the gap length for all pressures. A slight increase can be observed at 1.0 and 1.5 bar, while a very small decrease is observed at 2.0 bar. An increase in pressure will increase the E_{max} value but the behaviour of the E_{max} will be almost the same value for all the gap lengths for all pressures. In general, as with U_{50}, it can be said that, for a CF_3I-CO_2 (30%-70%) gas

mixture, E_{max} curves are the same for pressures of 1 – 2 bar in relation to gap length under a rod-plane electrode configuration.

Changes in U_{50} and E_{max} in relation to varying pressures are shown in Figure 6.2 and Figure 6.3 respectively under both positive and negative impulses.

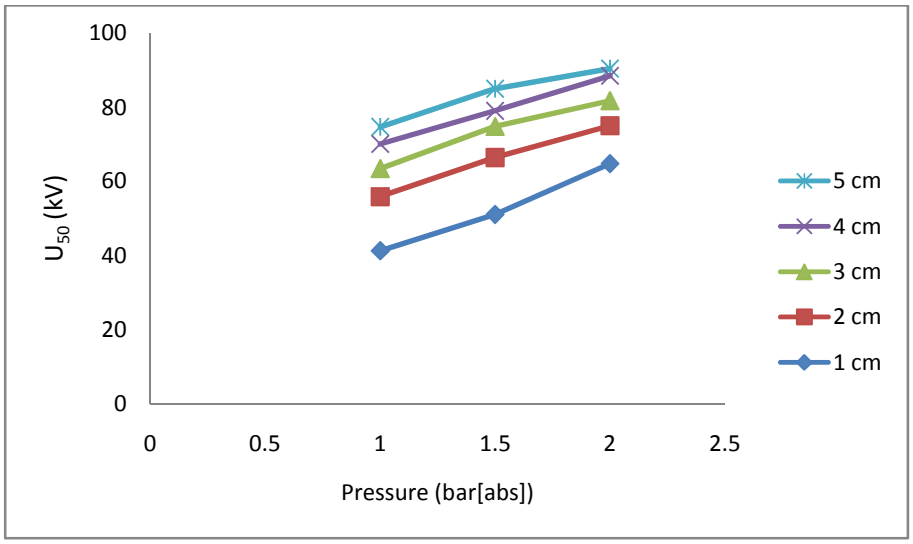

(a) Positive polarity

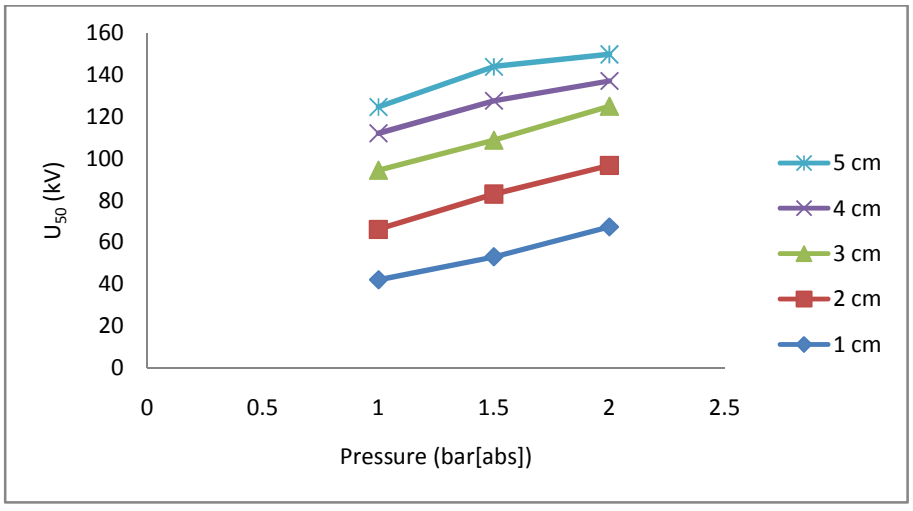

(b) Negative polarity

Figure 6.2: Effects of CF_3I-CO_2 pressures on U_{50} in a rod-plane electrode configuration

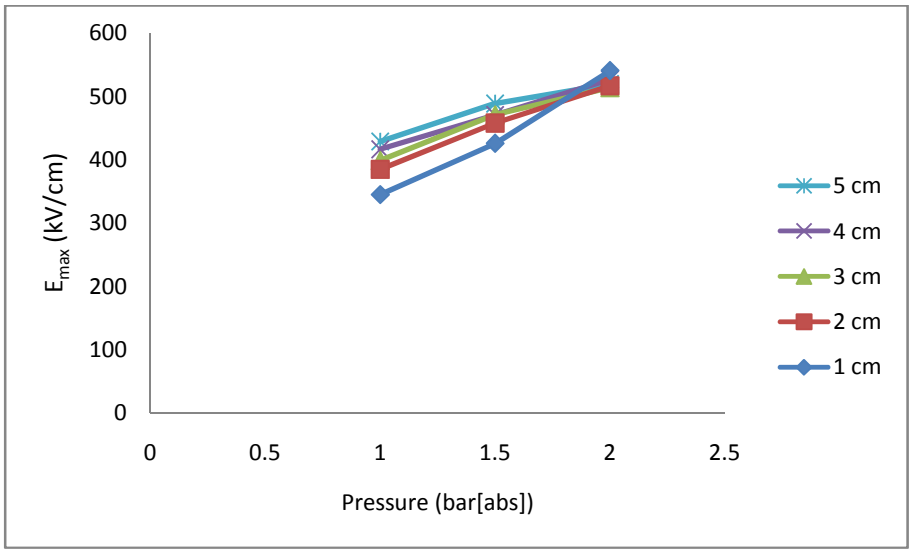

(a) Positive polarity

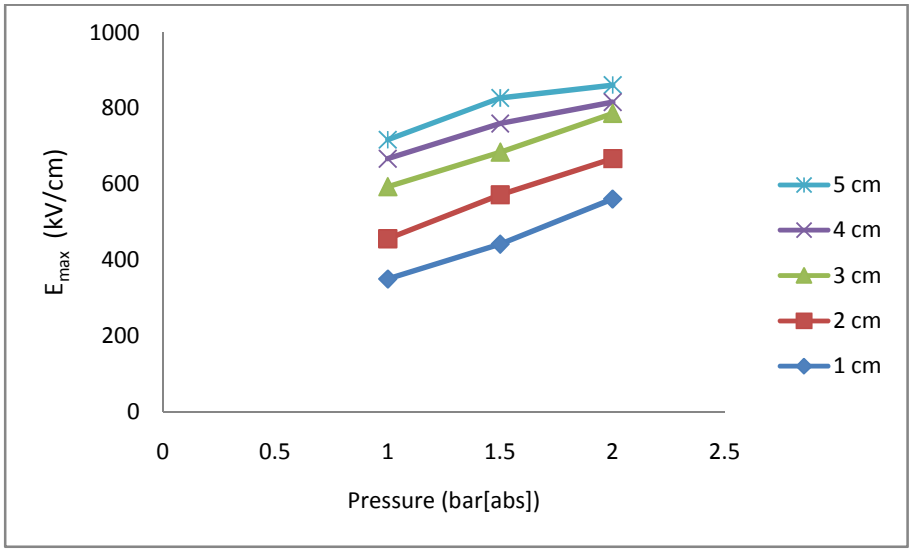

(b) Negative polarity

Figure 6.3: Effects of CF_3I-CO_2 pressures on E_{max} in a rod-plane electrode configuration

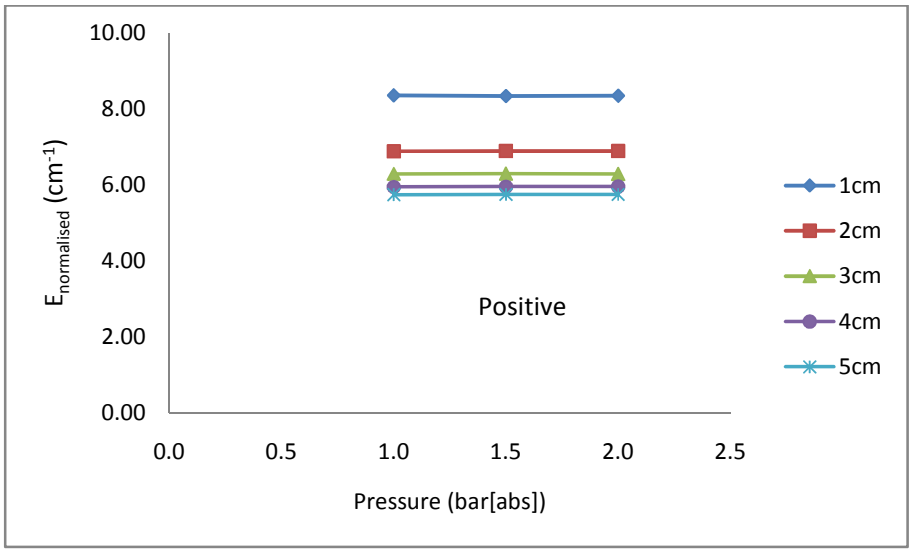

Figure 6.4: Effect of CF_3I-CO_2 pressures on $E_{normalised}$ in a rod-plane electrode configuration

Interestingly, from Figure 6.2 and Figure 6.3, an increase in pressure from 1 bar to 2 bar affects the changes in U_{50} and E_{max}. As can be seen from the figures, higher pressure leads to a smaller difference between a 1 cm gap and a 5 cm gap in both U_{50} and E_{max}. Figure 6.4, on the other hand, shows that $E_{normalised}$ values are the same throughout the pressure for each gap.

6.2.2 *V-t* Characteristics

The breakdown properties of CF_3I-CO_2 gas mixtures with a 30%-70% gas mixture ratio at different pressures under positive lightning impulses can be seen on the *V-t* characteristics, as depicted in Figure 6.5.

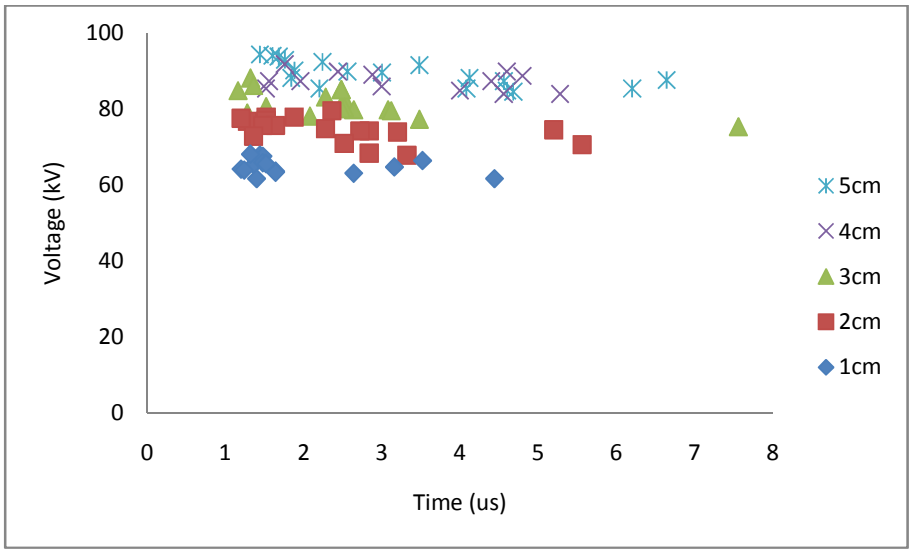

(a) 2.0 bar

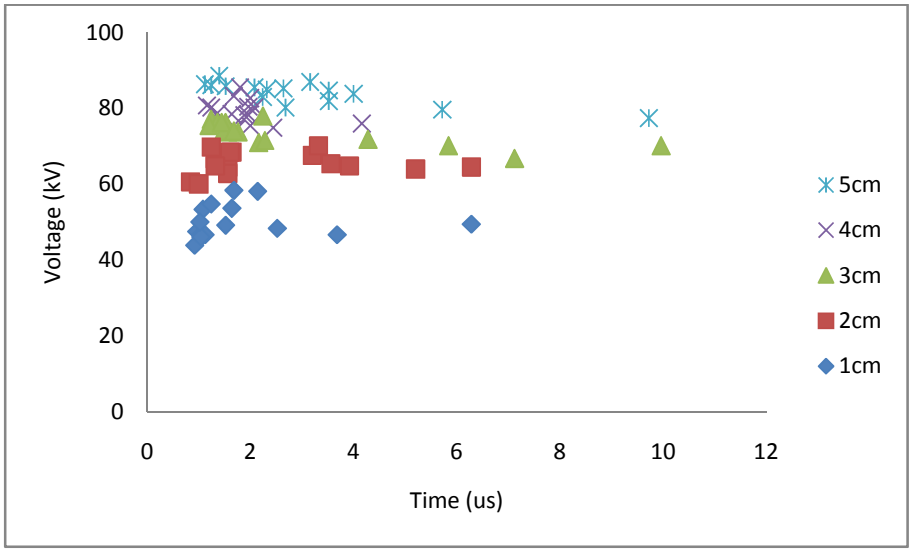

(b) 1.5 bar

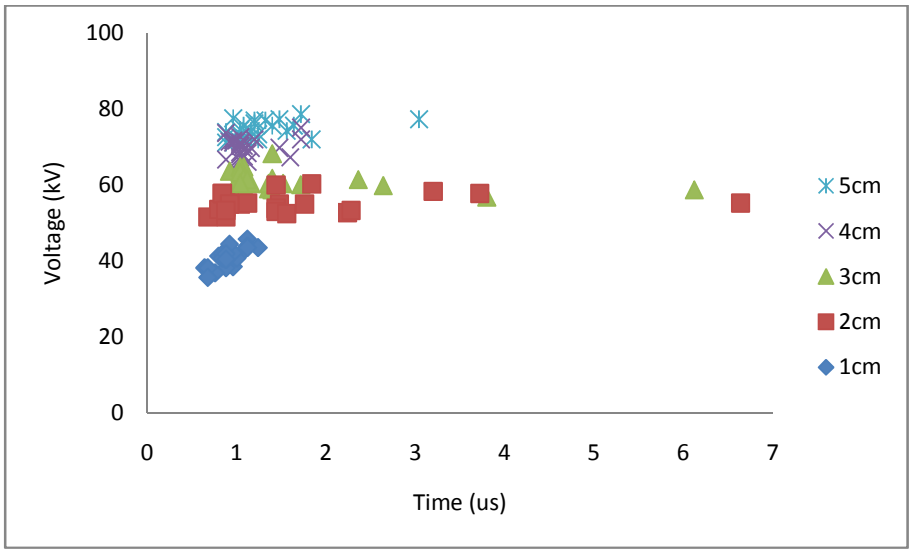

(c) 1.0 bar

Figure 6.5: *V-t* characteristics for CF_3I-CO_2 (30%-70%) with a rod-plane electrode configuration under a positive impulse

Closer examination of the above figures in all cases indicates that under a rod-plane configuration most of the breakdowns occur at less than 8 μs for all pressures. Although most of the breakdowns in a 1 cm gap at 1.0 bar occur around the peak of the lightning impulse, which is in the region of 1 – 2 μs at 1.5 and 2.0 bar, with the same gap length, the instants of breakdown are more distributed along the time scale, up to 6 μs. At a pressure of 2.0 bar, as shown in Figure 6.5(a), the *V-t* characteristics for a 5 cm gap can be seen to be slightly higher than that for a 4 cm gap. This behaviour reflects the small difference in U_{50} with only 2 kV, as can be seen in Table 6.2. The corresponding *V-t* characteristics under negative impulses are shown in Figure 6.6.

An investigation on *V-t* characteristics under lightning impulse for various pressures of SF_6 has been carried out by Yoshida et al. [120]. A sphere-plane configuration electrode system was used in the tests. As has been achieved in this study, Yoshida et al. also reported that *V-t* characteristics become higher as the gas pressure

increases. The *V-t* characteristics for SF_6 also exhibit similar curves with CF_3I, as depicted in Figure 6.5.

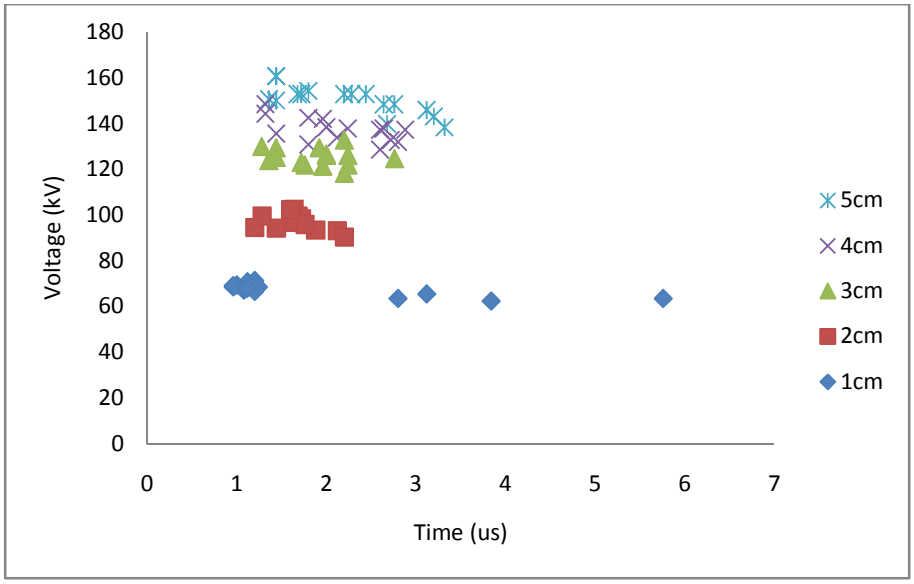

(a) 2.0 bar

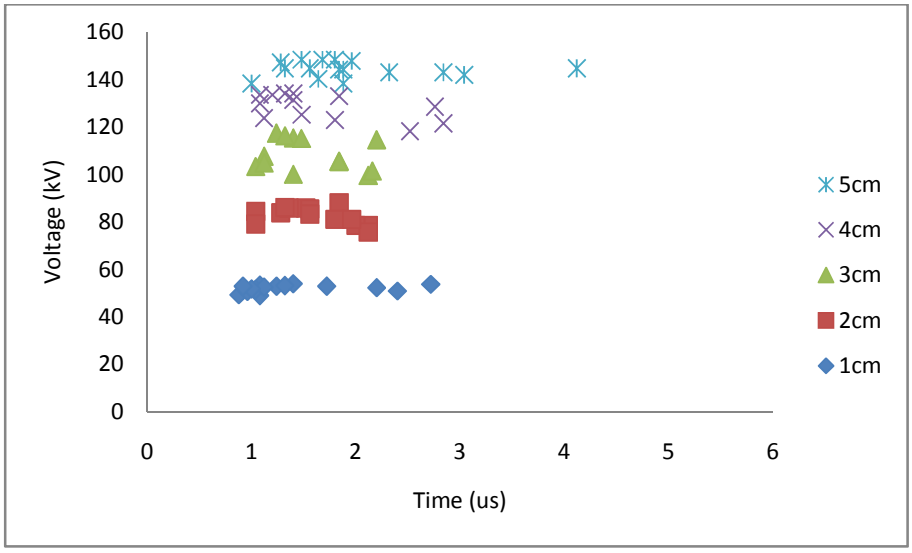

(b) 1.5 bar

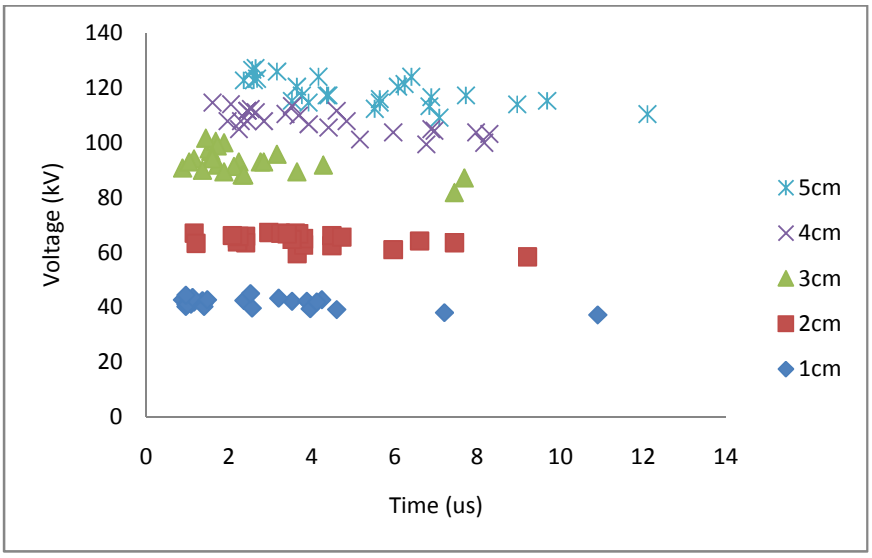

(c) 1.0 bar

Figure 6.6: *V-t* characteristics for CF_3I-CO_2 (30%-70%) mixture using a rod-plane electrode configuration under negative impulses at various pressures

As observed previously in Figure 6.1(a), U_{50} in a rod-plane electrode configuration under negative impulses are much higher than under positive impulses for all pressures, and the difference increases with gap length. Moreover, there is a significant increment in U_{50} throughout the gap length in all pressures. This increment can also be seen in Figure 6.6 as compared to Figure 6.5. Furthermore, it can be observed that at higher pressures, most of the breakdowns occur earlier than those for a 1.0 bar pressure, with a time frame of less than 6 µs.

U_{50}-*pd* curves for CF_3I-CO_2 (30%-70%) mixtures are shown in Figure 6.7 and are different from the U_{50}-*pd* curve for air, as depicted in Figure 4.14, which is linear. This is due to the fact that the U_{50}-*pd* curve reflects the U_{50} curve in relation to the gap length. For this reason, referring to Figure 6.1(a), a U_{50}-*pd* curve for CF_3I-CO_2 (30%-70%) under a positive impulse will be slightly more flat when compared to the curve under a negative impulse.

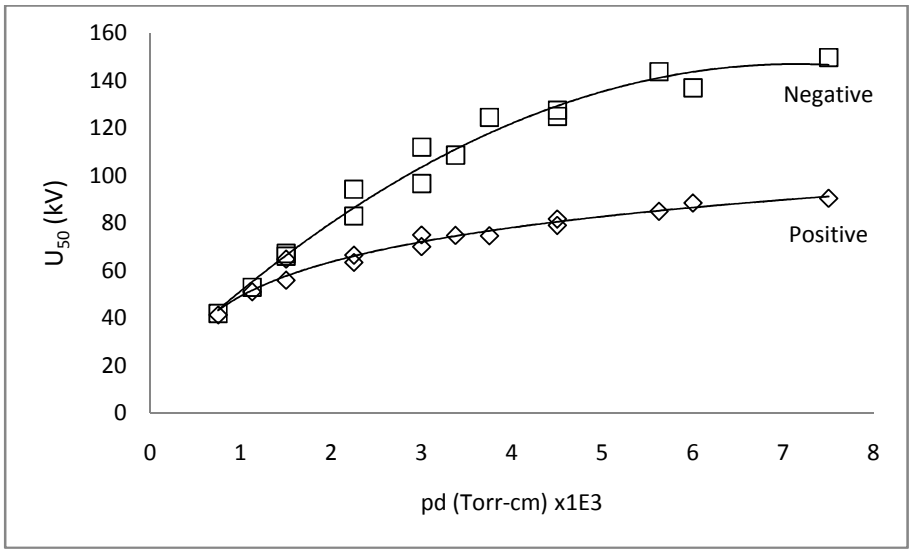

Figure 6.7: U_{50} curve for CF_3I-CO_2 (30%-70%) mixtures under a rod-plane electrode configuration in relation to the product of pressure and gap length, *pd*

6.3 Effect of CF_3I Content

In this section, further efforts are taken to carry out tests on different mixture ratios of CF_3I-CO_2 gases. As this study is focused on the investigations of CF_3I-CO_2 gas mixtures with ratios of 30%-70%, it will be interesting to investigate the variations of the mixture ratio and how it will affect the insulation performance of the mixtures.

Hypothetically, an increase in CF_3I content will provide an increase in insulation strength and vice versa. Thus, this study examines by how much the insulation strength of the gas mixture will be increased or whether the increase will occur. It should be emphasized that the selection of CF_3I content is basically due to three major factors: insulation strength, boiling point, and the by-products of the gas mixtures. Although an increase in CF_3I content might increase the insulation strength, the boiling point and by-products will also be increased, which is an undesirable outcome.

In this investigation, the tests are carried out with two different electrode configurations, these include the rod-plane and plane-plane electrode configurations, as

was shown in Figure 5.3(a) and Figure 5.3(b). These were completed with a field utilization factor of 0.12 and 0.77 respectively. The tests were carried out at an absolute pressure of 0.1 MPa (1 bar).

6.3.1 Effects of CF_3I Content in a Rod-Plane Electrode Configuration

In this section, the effects of CF_3I content in CF_3I-CO_2 gas mixtures will be examined under non-uniform electric fields, as in a rod-plane electrode configuration.

6.3.1.1 Magnitude of U_{50} and E_{max}

The tests were carried out for gap lengths between 1 – 5 cm. The test results are shown in Table 6.5. From these data E_{max} is obtained by using FEM software for each test condition and is presented in Table 6.6.

Table 6.5: U_{50} for different CF_3I content in CF_3I-CO_2 gas mixtures in rod-plane electrode configurations at 1.0 bar

Gap length (cm)	U_{50} (kV)					
	Positive Impulse			Negative Impulse		
	20%-80%	30%-70%	40%-60%	20%-80%	30%-70%	40%-60%
1	39.64	41.28	44.19	40.12	41.96	48.45
2	54.95	55.91	56.24	64.24	66.09	72.43
3	62.05	63.41	65.97	90.14	94.30	101.18
4	69.16	70.08	71.00	106.50	112.04	115.05
5	71.94	74.69	75.43	120.43	124.62	132.36

Table 6.6: E_{max} for different CF_3I content in CF_3I-CO_2 gas mixtures in a rod-plane electrode configuration

Gap length (cm)	E_{max} (kV/cm)					
	Positive Impulse			Negative Impulse		
	20%-80%	30%-70%	40%-60%	20%-80%	30%-70%	40%-60%
1	331	345	369	335	350	404
2	379	385	388	443	456	499
3	390	399	415	567	593	637
4	412	417	423	634	667	685
5	413	429	434	692	717	761

Table 6.7: $E_{normalised}$ for different CF_3I content in CF_3I-CO_2 gas mixtures in a rod-plane electrode configuration

Gap length (cm)	$E_{normalised}$ (cm^{-1})					
	Positive Impulse			Negative Impulse		
	20%-80%	30%-70%	40%-60%	20%-80%	30%-70%	40%-60%
1	8.4	8.4	8.4	8.4	8.3	8.3
2	6.9	6.9	6.9	6.9	6.9	6.9
3	6.3	6.3	6.3	6.3	6.3	6.3
4	6.0	6.0	6.0	6.0	6.0	6.0
5	5.7	5.7	5.8	5.7	5.8	5.7

The data of U_{50} and E_{max} curves are plotted as a function of gap length in Figure 6.8(a) and Figure 6.8(b) respectively. As expected in a rod-plane electrode configuration, both U_{50} and E_{max} under a negative impulse polarity are significantly higher than those under a positive impulse polarity. Comparing the three CF_3I-CO_2 gas mixtures (20%-80%, 30%-70% and 40%-60%) studied in this investigation, there is no significant difference that can be observed under positive impulse polarity, in contrast to negative impulse polarity. Generally, both U_{50} and E_{max} trends for CF_3I-CO_2 gas mixtures are the same independent of the mixture ratio in a rod-plane electrode configuration, in accordance to their respective impulse polarity.

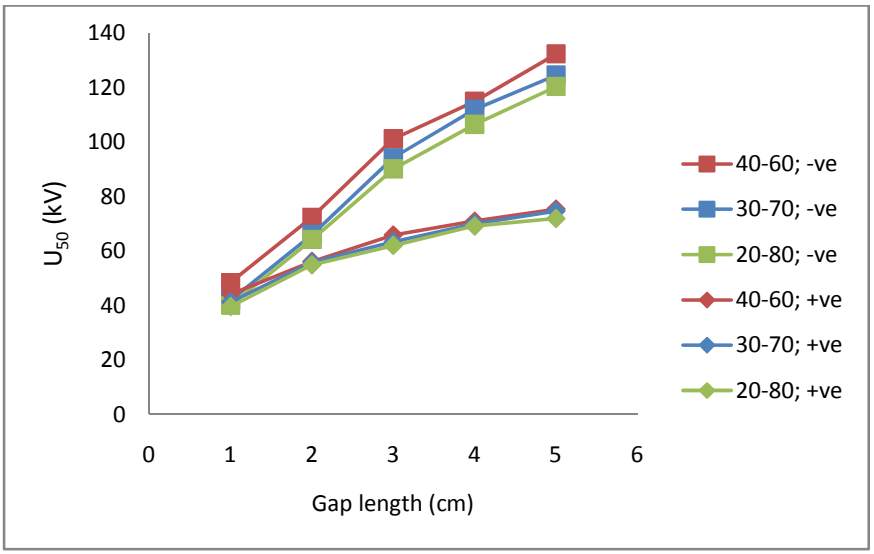

(a) U_{50}

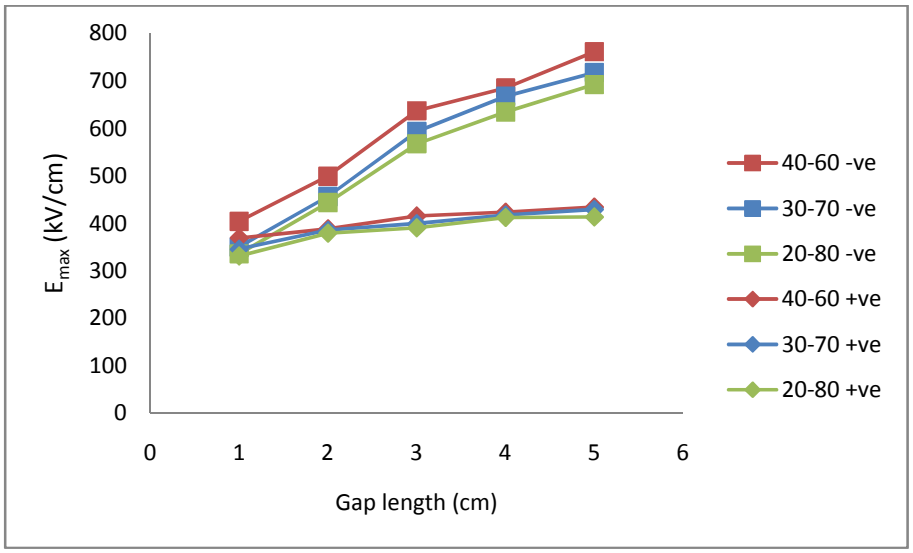

(b) E_{max}

Figure 6.8: Curves for different CF_3I-CO_2 mixtures in rod-plane electrode configurations, under both positive and negative lightning impulses, as a function of gap length

Figure 6.9(a) and Figure 6.9(b) show the relationship between U_{50} and E_{max} to CF_3I content. Due to the huge amount of data, and to avoid confusion, only three (3)

different gaps are plotted, specifically 1 cm, 3 cm, and 5 cm for both positive and negative impulses.

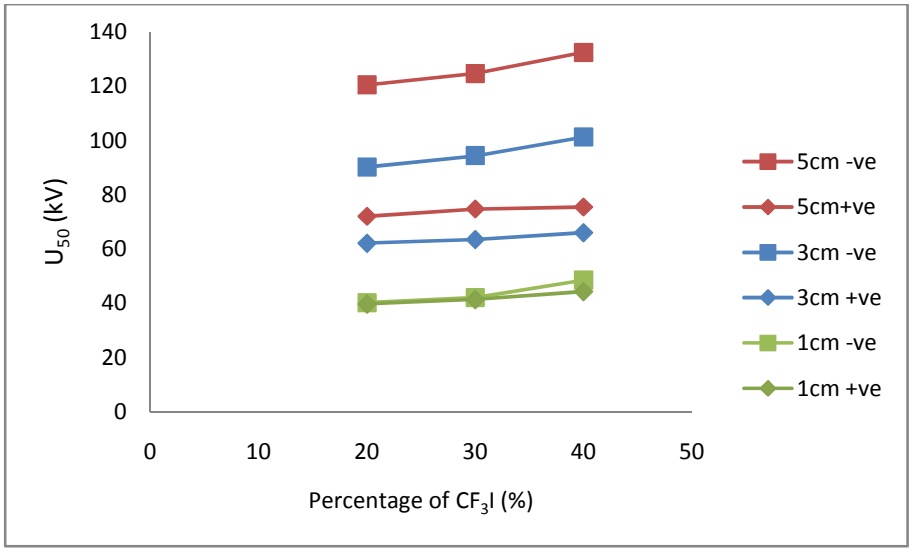

(a) U_{50}

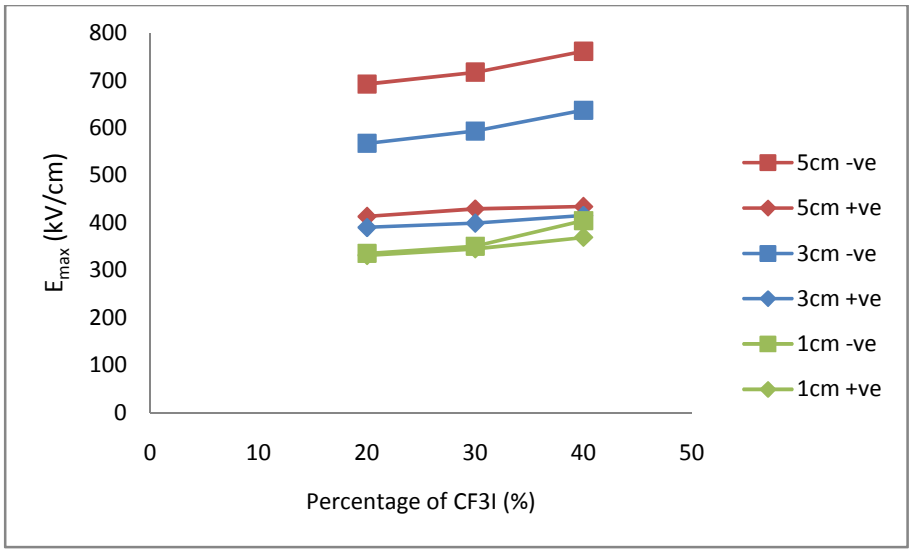

(b) E_{max}

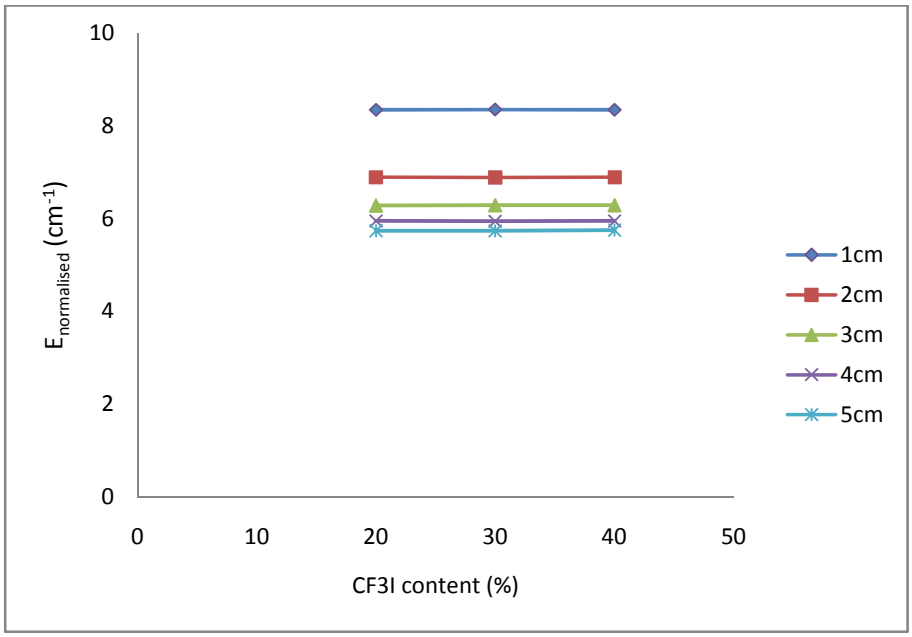

(c) $E_{normalised}$

Figure 6.9: Effects of CF_3I content in a rod-plane electrode configuration under positive and negative impulse polarities

It can be clearly seen from Figure 6.9 that, for both U_{50} and E_{max} magnitudes, the effect of CF_3I content is more significant under negative impulse polarity. For a change of CF_3I content from 20% to 40% in CF_3I-CO_2 gas mixtures, U_{50} increases by 8 kV (21%) for the 1 cm gap, 11 kV (12%) for the 3 cm gap, and 12 kV (10%) for the 5 cm gap. The same increment in terms of percentage can be seen for E_{max}, with a 69 kV/cm (21%) increment in a 1 cm gap, a 70 kV/cm (12%) with a 3 cm gap, and a 69 kV/cm (10%) with a 5 cm gap.

Under a positive impulse for the same increase in CF_3I content, only a 5 kV (11%) increase of U_{50} for the 1 cm gap, a 4 kV (6%) increase for the 3 cm gap, and a 3 kV (5%) increase for the 5 cm gap was noted. Meanwhile an increase in E_{max} can be calculated as 38 kV/cm (11%) for the 1 cm gap, 25 kV/cm (6%) for the 3 cm gap, and 21 kV/cm (5%) for the 5 cm gap. Based on these investigations, it can be said that, in a

rod-plane electrode configuration, the CF_3I content in a gas mixture of CF_3I-CO_2 will have more effect for smaller gaps, as compared to larger gaps, under both positive and negative impulse polarities. With rod-plane electrode configuration, $E_{normalised}$ maintains the same values for each gap length throughout for any CF_3I contents. Table 6.8 summarizes the effects of CF_3I content in a rod-plane electrode configuration.

Table 6.8: Effects of a 20% increase in CF_3I content on U_{50} and E_{max} in a rod-plane electrode configuration under positive and negative impulse polarities (1.0 bar)

Gap length (cm)	U_{50} (kV)		E_{max} (kV/cm)		E_{max} and U_{50} (%)	
	Positive	Negative	Positive	Negative	Positive	Negative
1	+5	+8	+38	+69	+11	+21
2	+1	+8	+9	+56	+2	+13
3	+4	+11	+25	+70	+6	+12
4	+2	+9	+11	+51	+3	+8
5	+3	+12	+21	+69	+5	+10

+ denotes increase in value

6.3.1.2 *V-t* Characteristics

Examples of *V-t* characteristics are shown in Figure 6.10(a) and Figure 6.10(b) under positive and negative impulses, respectively. The *V-t* characteristics are for a rod-plane electrode configuration with 1 cm gap.

As described in section 5.4.1, under a positive impulse in a rod-plane electrode configuration with a 1 cm gap, the instants of breakdown tend to happen earlier. This occurrence was observed for all CF_3I contents in CF_3I-CO_2 gas mixtures as can be seen in Figure 6.10(a). Under negative impulses, the time lags are more distributed along the wavetail of the lightning impulse as depicted in Figure 6.10(b). Under both polarities,

however, the *V-t*-characteristic for CF_3I-CO_2 (40%-60%) is the highest, while CF_3I-CO_2 (20%-80%) has the lowest *V-t* characteristic.

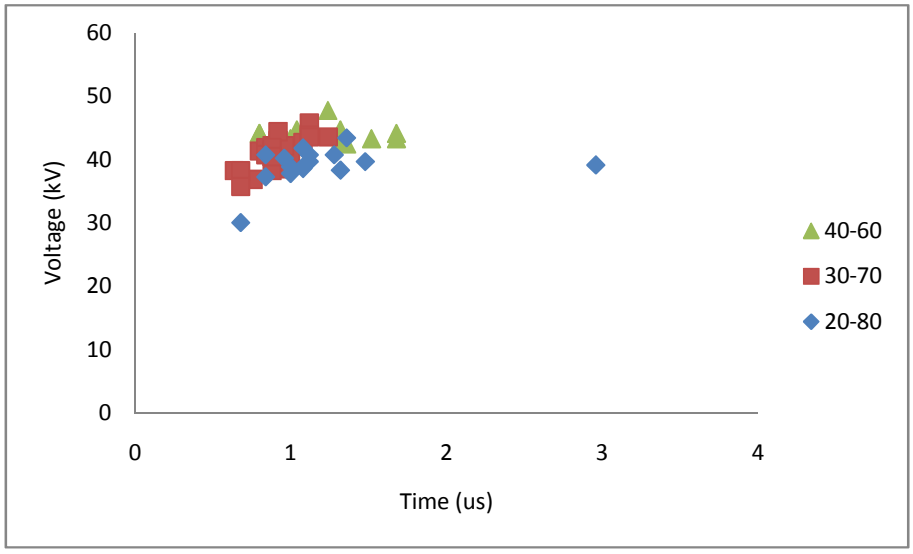

(a) Positive polarity

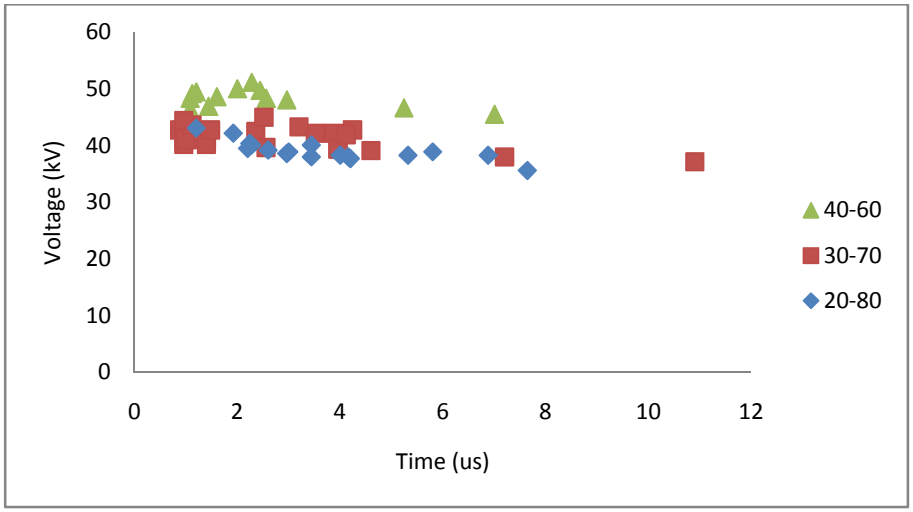

(b) Negative polarity

Figure 6.10: *V-t* characteristics for CF_3I-CO_2 gas mixtures in a rod-plane electrode configuration with 1 cm gap

6.3.2 Effects of CF_3I Content in Plane-Plane Electrode Configuration

6.3.2.1 Magnitude of U_{50} and E_{max}

In this section, the effects of CF_3I content in CF_3I-CO_2 gas mixtures will be examined under a more uniform electric field as compared with the previous section. The tests were carried out for gap lengths between 1 – 3 cm, and the results are shown in Table 6.9. As in the previous section, E_{max} is then obtained by using FEM software for each test condition and is presented in Table 6.10.

Table 6.9: U_{50} for different CF_3I content in CF_3I-CO_2 gas mixtures in a plane-plane electrode configuration

Gap length (cm)	U_{50} (kV)					
	Positive Impulse			Negative Impulse		
	20%-80%	30%-70%	40%-60%	20%-80%	30%-70%	40%-60%
1	53.74	57.50	64.75	52.52	55.76	60.14
2	100.51	112.98	122.94	95.76	98.66	108.89
3	149.79	161.27	182.87	125.00	133.76	145.85

Table 6.10: E_{max} for different CF_3I content in CF_3I-CO_2 gas mixtures in a plane-plane electrode configuration

Gap length (cm)	E_{max} (kV/cm)					
	Positive Impulse			Negative Impulse		
	20%-80%	30%-70%	40%-60%	20%-80%	30%-70%	40%-60%
1	70	75	85	69	73	79
2	87	98	106	83	85	94
3	109	117	133	91	97	106

Table 6.11: $E_{normalised}$ for different CF_3I content in CF_3I-CO_2 gas mixtures in a plane-plane electrode configuration

Gap length (cm)	$E_{normalised}$ (cm^{-1})					
	Positive Impulse			Negative Impulse		
	20%-80%	30%-70%	40%-60%	20%-80%	30%-70%	40%-60%
1	1.3	1.3	1.3	1.3	1.3	1.3
2	0.9	0.9	0.9	0.9	0.9	0.9
3	0.7	0.7	0.7	0.7	0.7	0.7

Comparisons of U_{50} and E_{max} curves for those mixtures in a plane-plane electrode configuration are shown in Figure 6.11(a) and Figure 6.11(b), for both positive and negative impulse polarities.

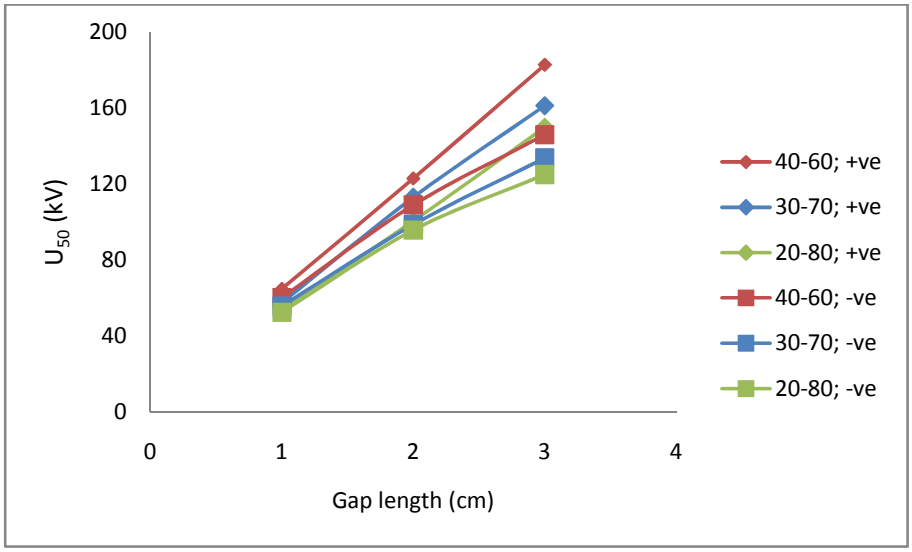

(a) U_{50}

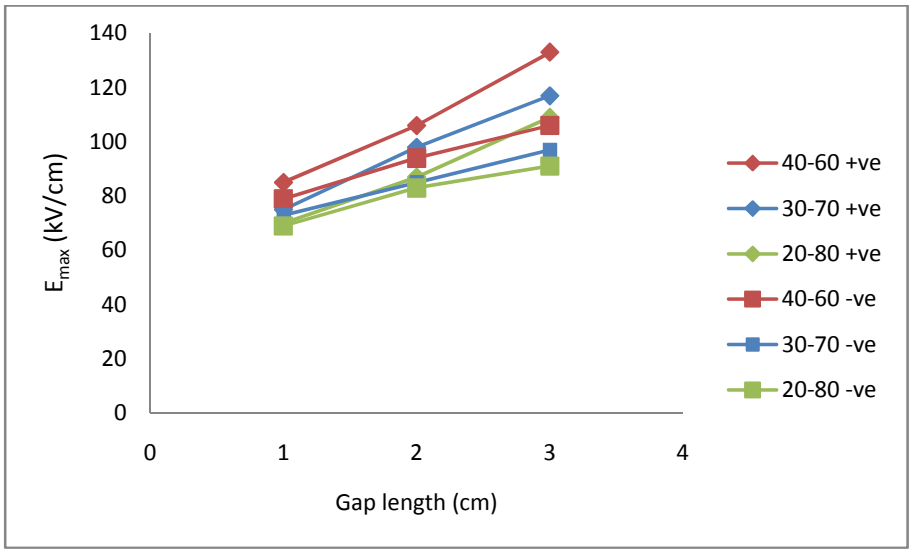

(b) E_{max}

Figure 6.11: Curves for different CF_3I-CO_2 mixtures in a plane-plane electrode configuration, under both positive and negative lightning impulses in relation to gap length

In plane-plane electrode configurations, it is expected that both U_{50} and E_{max} under a positive impulse polarity will be higher than under a negative impulse polarity, as has been investigated and presented in section 5.4.2 for CF_3I-CO_2 gas mixture of 30%-70%. This is opposite to those in a rod-plane electrode configuration. In all mixtures, E_{max} increases with gap length and the same applies to U_{50} values. From Figure 6.11, it can be seen that, in general, U_{50} and E_{max} trends for all CF_3I-CO_2 mixtures are the same in a plane-plane electrode configuration, according to the respective impulse polarities.

The relationship between U_{50} and E_{max} to CF_3I content in this configuration is shown in Figure 6.12(a) and Figure 6.12(b), for both positive and negative impulse polarities.

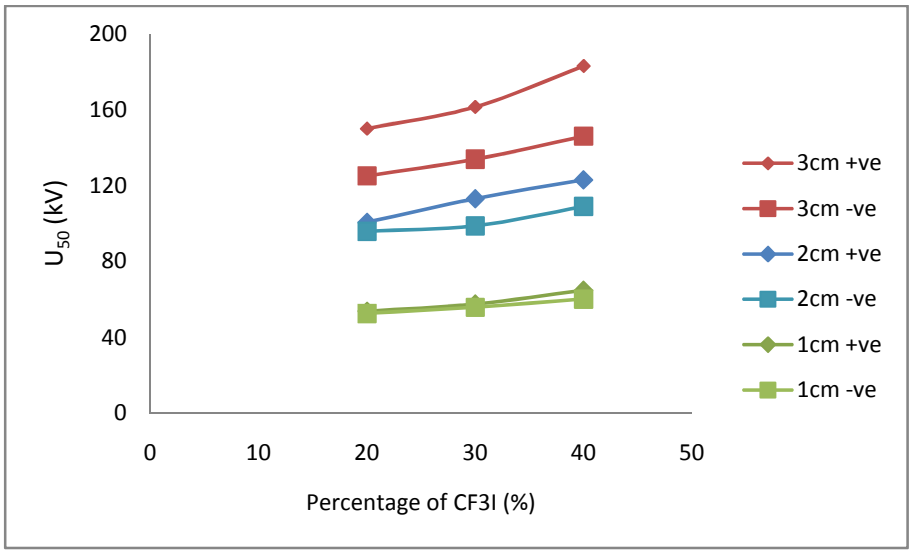
200
160
120
80
40
0
U50 (kV)
0
10
20
30
40
50
Percentage of CF3I (%)
3cm +ve
3cm -ve
2cm +ve
2cm -ve
1cm +ve
1cm -ve

(a) U_{50}

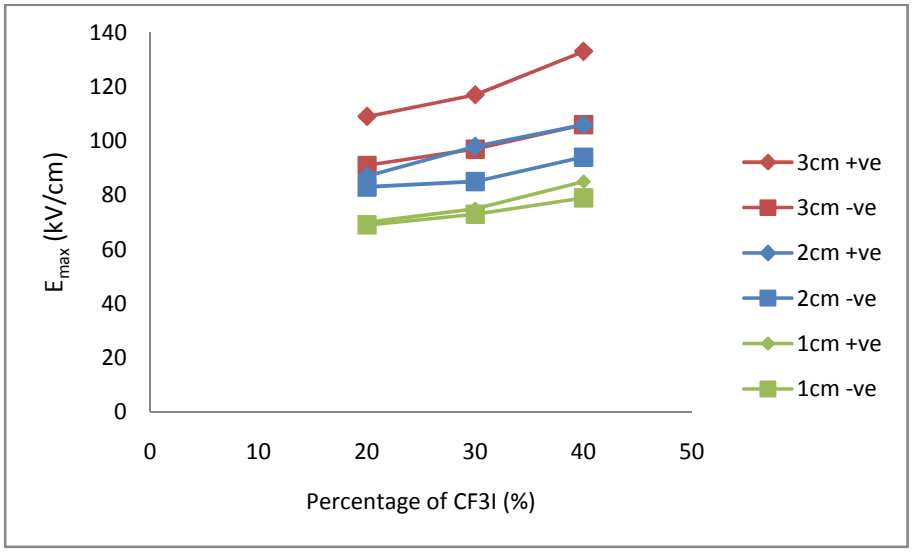
140
120
100
80
60
40
20
0
Emax (kV/cm)
0
10
20
30
40
50
Percentage of CF3I (%)
3cm +ve
3cm -ve
2cm +ve
2cm -ve
1cm +ve
1cm -ve

(b) E_{max}

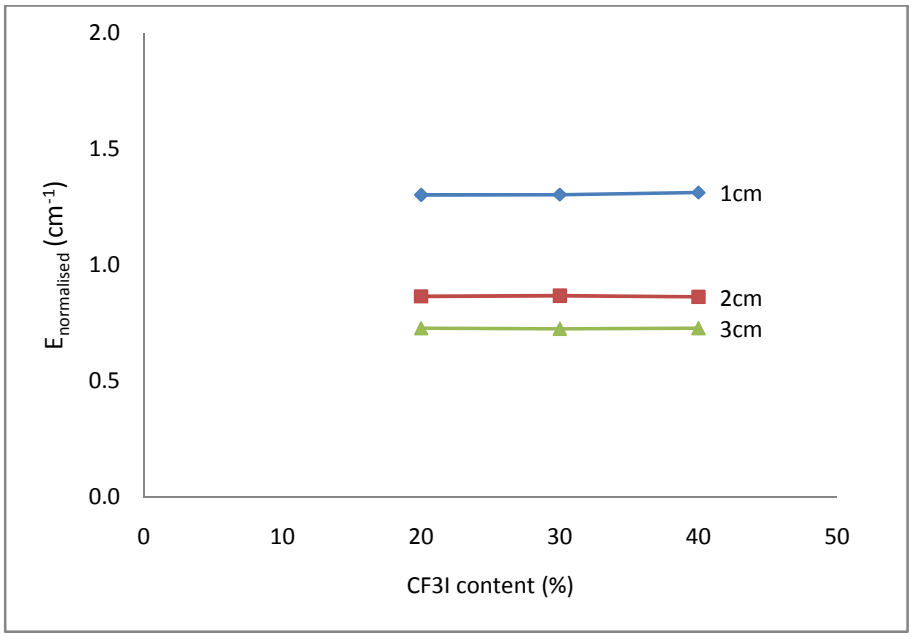

(c) $E_{normalised}$

Figure 6.12: Effects of CF_3I content on in a plane-plane electrode configuration under positive and negative impulse polarities

It can be observed in Figure 6.12 that, with an increase in CF_3I content, the differences between positive and negative values of U_{50} and E_{max} are also increased slightly. Under positive polarity, an increase from 20% of CF_3I to 40% of CF_3I in CF_3I-CO_2 gas mixtures leads to an increase in U_{50} of 11 kV (20%) in a 1 cm gap, 22 kV (22%) in a 2 cm gap, and 33 kV (22%) in a 3 cm gap. The same increment in terms of percentage is also seen in E_{max} with 15 kV/cm (21%) increases in a 1 cm gap, 19 kV/cm (22%) with a 2 cm gap, and 24 kV/cm (22%) with a 3 cm gap. From the above data, it is interesting to note that, in a plane-plane electrode configuration, a 20% increase in CF_3I content gives almost the same amount of percentage increase in U_{50} and E_{max} under positive impulse polarity in the range of 20%-22%.

Analysing the changes in U_{50} under negative impulses reveals that, for the same increase in CF_3I content, there is a 7.6 kV (15%) increase in a 1 cm gap, 13 kV (14%)

increase in a 2 cm gap, and a 21 kV (17%) increase in a 3 cm gap. Increases in E_{max}, on the other hand, was estimated as 10 kV/cm (14%) in a 1 cm gap, 11 kV/cm (13%) in a 2 cm gap, and 15 kV/cm (16%) in a 3 cm gap. As well as in rod-plane electrode configuration, $E_{normalised}$ in plane-plane electrode configuration stays flat for each gap for all CF_3I contents.

Table 6.12: Effects of 20% increase in CF_3I content on U_{50} and E_{max} in a plane-plane electrode configuration under positive and negative impulses (1 bar)

Gap length (cm)	U_{50} (kV)		E_{max} (kV/cm)		E_{max} and U_{50} (%)	
	Positive	Negative	Positive	Negative	Positive	Negative
1	+11	+8	+15	+10	+20	+15
2	+22	+13	+19	+11	+22	+14
3	+33	+21	+24	+15	+22	+17

+ denotes increase in value

6.3.2.2 *V-t* Characteristics

Example of *V-t* characteristics are shown in Figure 6.13(a) and Figure 6.13(b) under positive and negative impulses respectively. The *V-t* characteristics are for a plane-plane electrode configuration with a 1 cm gap.

As opposed to the rod-plane configuration in a positive polarity, instants of sparkovers in a plane-plane electrode configuration are more distributed along the wavetail of the lightning impulse. In all three mixtures, CF_3I-CO_2 (40%-60%) has the highest *V-t* characteristic, while *V-t* characteristic for CF_3I-CO_2 (20%-80%) is the lowest. Generally, it can be seen that *V-t* characteristic increases with CF_3I content.

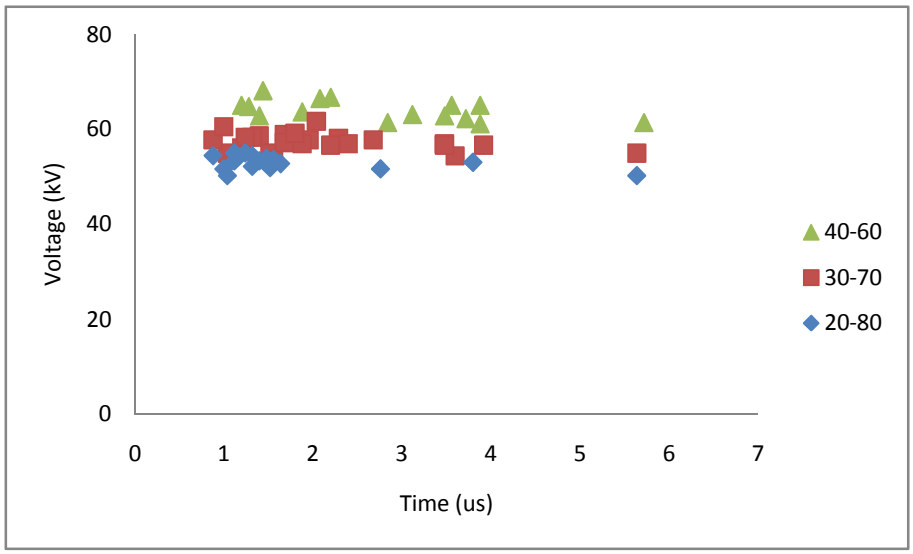

(a) Positive polarity

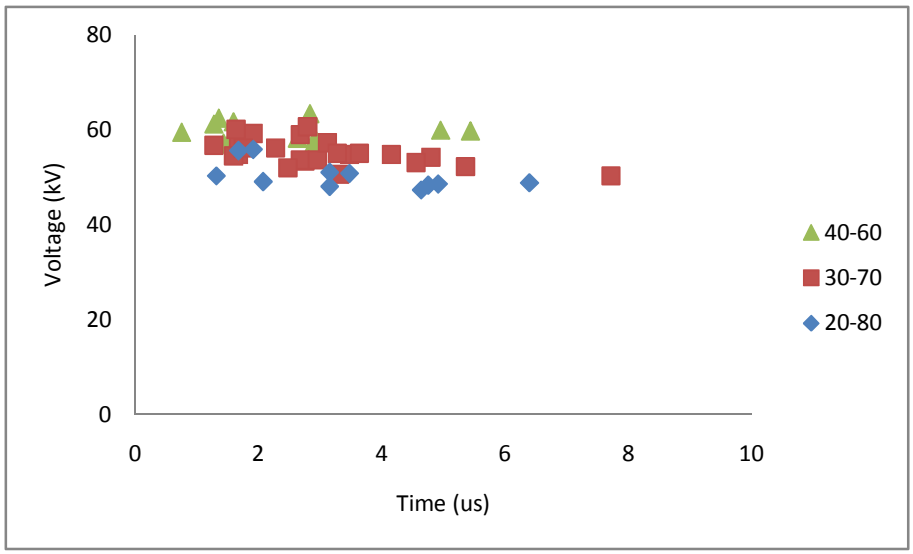

(b) Negative polarity

Figure 6.13: *V-t* characteristics for CF_3I-CO_2 mixtures in a plane-plane electrode configuration with a 1 cm gap

This experimental investigation confirms that CF_3I content affects the insulation strength of CF_3I-CO_2 gas mixtures, as reported from previous works for other CF_3I mixtures. Effects of CF_3I content in CF_3I-N_2 and CF_3I-Air mixtures have been studied

by Toyota et al. [49] using steep front square voltage. It is reported that *V-t* characteristics for characteristics for CF_3I-Air and CF_3I-N_2 gas mixtures increase with CF_3I content. Meanwhile, Kasuya et al. [41] and Taki et al. [44] have studied the effects of CF_3I content in CF_3I-CO_2 and CF_3I-N_2 gas mixtures for current interruption capability properties. In both gas mixtures, current interruption capabilities increase with CF_3I content.

In this study, U_{50} and E_{max} of CF_3I-CO_2 mixtures can be increased by increasing the content of CF_3I. However, in terms of increase in percentage, an increase in CF_3I content gives more benefit to insulation properties in a plane-plane electrode rather than a rod-plane electrode. Meanwhile, for a rod-plane electrode, it is only under negative impulses, and in particular in smaller gaps, that the insulation properties of CF_3I-CO_2 will benefit by increasing the CF_3I content.

6.3.3 Relation of CF_3I Content with Liquefaction Temperature (T_{mb})

It is very important to develop the relationship between CF_3I content in its mixtures with the boiling point of the mixtures, since it will be one of the key points in determining the ratio of the mixtures. Although until now there was no report on a complete experimental work on developing the relation of gas mixtures to the boiling point under several pressures, efforts have been made theoretically for this relation.

Deng and Xiao [34], Yamamoto et al. [121], and Xing et al. [122] have all worked out the relation of boiling temperature for different gas mixtures, albeit most are N_2 mixtures. The researchers reported that for a gas mixture with one gas that has a relatively low boiling temperature compared to other gases, then the former can be assumed as an ideal gas [34], [121], [122]. The mixtures used are c-C_4F_8-N_2 mixture by

Yamamoto, C_4F_8-N_2 mixture by Xing, and CF_3I-N_2 mixture by Deng and Xiao. In each case, the researchers assumed N_2 as the ideal gas.

In order to develop the relationship of boiling temperature point with CF_3I content on a CF_3I-CO_2 gas mixture, the methods used by Yamamoto and Deng are considered. According to Yamamoto et al. [121], the vapour pressure P_v (MPa) of a gas with boiling point T_b is dependent on temperature T and can be approximated as

$$P_v = \frac{1}{10}\exp\frac{A(1-\frac{T_b}{T})}{R} \qquad (6.1)$$

where A: constant, 87 J/mol.K

R: gas constant, 8.3 J/mol.K

Using the assumption made on the ideal gas condition, the liquefaction temperature, T_{mb}, of a gas mixture is given by

$$T_{mb} = \frac{T_b}{1-\frac{\ln(10kP_v)}{10.5}} \qquad (6.2)$$

where k is the ratio (partial pressure) of the other gas.

As for CF_3I-CO_2 gas mixtures, by assuming CO_2 as the ideal gas, the relation of T_{mb} with CF_3I content is depicted in Figure 6.14 for a pressure range of 1 – 5 bar.

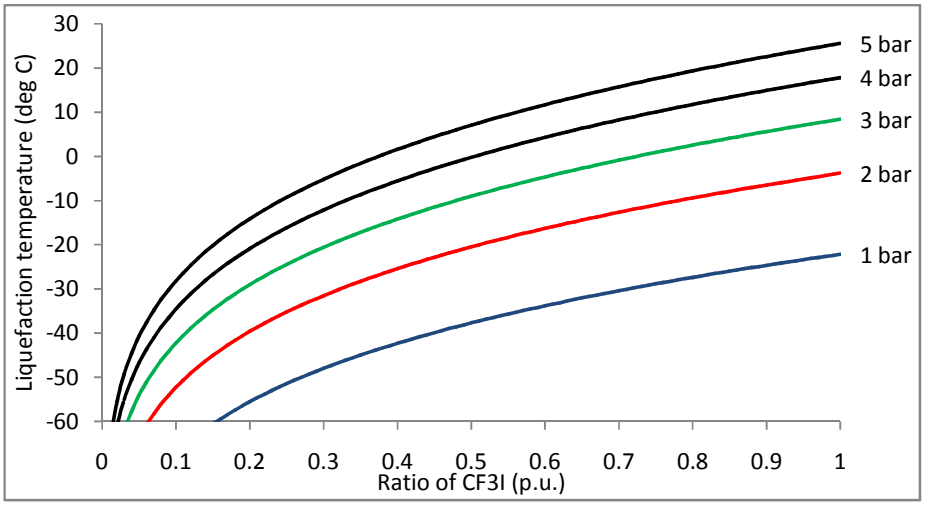

Figure 6.14: Relation of liquefaction temperature with CF_3I content at different gas pressures (Yamamoto method)

Meanwhile, according to Deng and Xiao [34], the relation between T_{mb} and CF_3I content of CF_3I-CO_2 gas mixture can be developed by using vapour pressure equation (Eqn. (2.1)) as reported by Duan et. al. [36] with Van der Waals equation (equation of state for gases), as notated

$$\left(P + \frac{a}{V^2}\right)(V - b) = RT \qquad (6.3)$$

where

P: pressure of the gas

V: volume of the gas

R: gas constant

T: absolute temperature

a: Van der Waals constant for CF_3I ~ 1.1967 Pa·$(m^3/mol)^2$

b: Van der Waals constant for CF_3I ~ 1.0626 × 10^4 m^3/mol

By assuming T_0 as the temperature of the gas, namely 25 ºC, P_0 as the primary pressure, namely 1 – 5 bar, and T_{mb} as the liquefaction temperature with corresponding pressure of P_{mb}, the state of the gas mixture meets the following equations:

$$\ln\left(\frac{P_{mb}}{P_c}\right) = (A_1\tau + A_2\tau^{1.25} + A_3\tau^3 + A_2\tau^{1.25}A_4\tau^7)\frac{T_c}{T_{mb}} \qquad (6.4)$$

$$\left(kP_{mb} + \frac{a}{V^2}\right)(V - b) = RT_{mb} \qquad (6.5)$$

$$\left(kP_0 + \frac{a}{V^2}\right)(V - b) = RT_0 \qquad (6.6)$$

Solving the above three equations yields

$$k = \frac{T_0}{P_0} \times \frac{P_{mb}}{T_{mb}} \qquad (6.7)$$

which is the same equation (and hence might be the same method) as reported by Xing et al. [122]. Using this method, assuming CO_2 as an ideal gas, the relation between T_{mb} with CF_3I content for CF_3I-CO_2 mixture is shown in Figure 6.15.

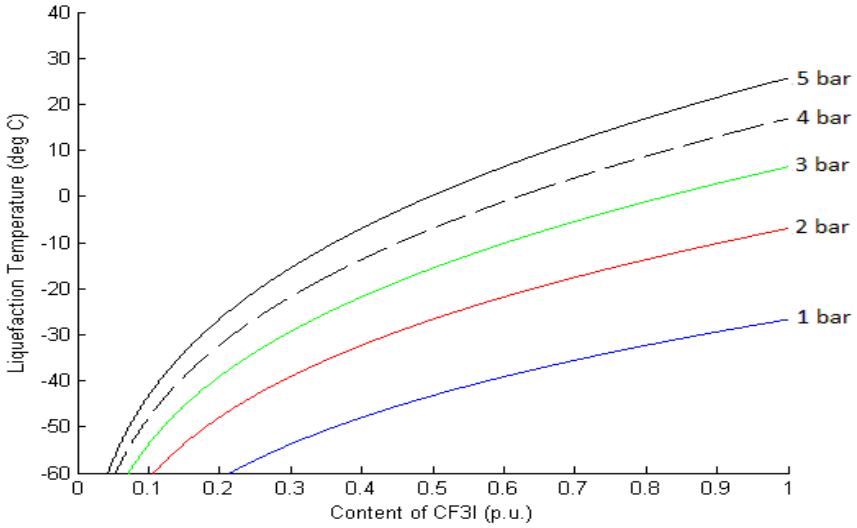

Figure 6.15: Relation of liquefaction temperature to CF_3I content at different gas pressures (Duan method)

Additional information is then taken from Kasuya et al. [41], [42], and Katagiri et al. [40], [43] which reported "*the boiling point of CF_3I-CO_2 (40%-60%) is about –5 ºC at 0.5 MPa*" and "*when the mixing ratio of CF_3I-CO_2 is 30%-70%, the boiling point is about –12 ºC at 0.5 MPa*". By cross-referencing this additional information with Figure 6.14 and Figure 6.15, it seems that the method introduced by Duan et al. is closer to the information provided. This might be due to differences of the CF_3I properties considered in both methods. In the first method, the CF_3I property considered by Yamamoto is only the boiling point (T_b) at a given pressure; while in the second method, Deng considers the CF_3I constants which are obtained experimentally by Duan et al. [36], as well as Van der Waals constants for CF_3I. This makes the curves obtained by Deng's method more likely to represent CF_3I-CO_2 mixtures.

6.4 Observation on Solid By-Products of CF_3I-CO_2 Mixtures

There are two major categories of by-products of CF_3I-CO_2 gas mixtures. These include solid by-products and gaseous by-products. In gaseous by-products, it has been reported and analysed by Kamarol et al. [58], Takeda et al. [57], [47] and Katagiri et al. [42] that the highest proportion comes from C_2F_6 gas (hexafluoroethane). In solid by-products, brownish material has been detected and reported by Takeda et. al. [47], [55], [60] and Katagiri et al. [40]. It is verified that this brownish material is indeed iodine.

In this investigation, two samples of electrodes, the rod electrode and plane (ground) electrode have been studied to examine the solid by-products. Figure 6.16 shows the brownish material on each electrode. In all observations, the solid by-product is more likely to be deposited on the high voltage or energized electrode rather than the ground electrode. The pattern of the solid deposits on both high voltage and ground electrodes are very similar to the damage caused by dc corona in SF_6 gas. Figure 6.16(a) shows the solid deposits are much clearer on the surface where the field line is the highest (near the tip of the rod), as explained by Yanallah and Pontiga [123]. This similarity with the dc corona effects has also been reported by Anis and Srivastava [48]. The pre-breakdown phenomena under observed under dc voltage is also generally true under impulse voltages [48].

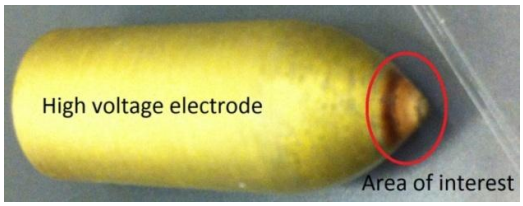

(a) rod

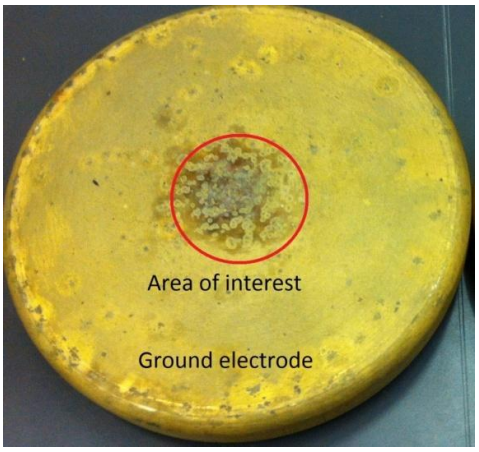

(b) plane (ground)

Figure 6.16: Solid by-product on electrodes

To analyse the solid by-product deposited on the electrodes, two methods are involved, image magnification is carried out using a Scanning Electron Microscope (SEM) and element analysis is done using an Energy Dispersive X-Ray (EDX) Spectrometer. By using these two methods, any element that exists on the surface of the electrodes can be analysed and confirmed.

SEM works by scanning an electron beam on the sample being studied [124] to produce a magnified image. The magnification of the image can be controlled by setting the electron beam to scan a smaller area of the sample, and by doing so, SEMs are capable of magnification at 300,000 times the size of the sample studied [125].

EDX, on the other hand, is an analytical technique used to analyse the elements that exist on a solid sample. When a sample is bombarded with an electron beam as in SEM, the x-ray spectrum will be omitted, and EDX makes use of this spectrum to investigate the element. In principle all, elements can be detected, from Beryllium (Be ~ atomic number 4) to Uranium (U ~ atomic number 92) [126]. Figure 6.17 shows a diagram of an electron beam that is focused on a specimen.

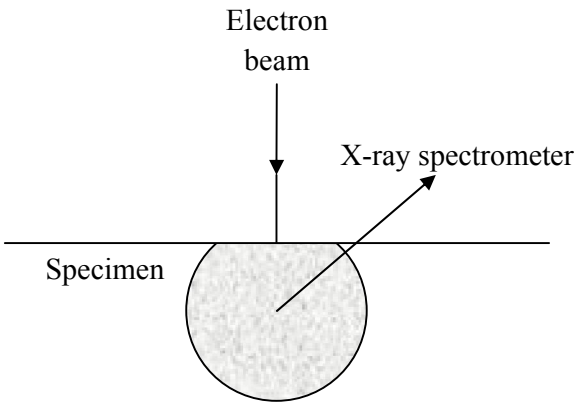

Figure 6.17: Specimen bombarded with an electron beam (reproduced from [126]**)**

Figure 6.18 shows the rod electrode ready to be placed inside an SEM, and Figure 6.19 shows the view from the camera inside the SEM.

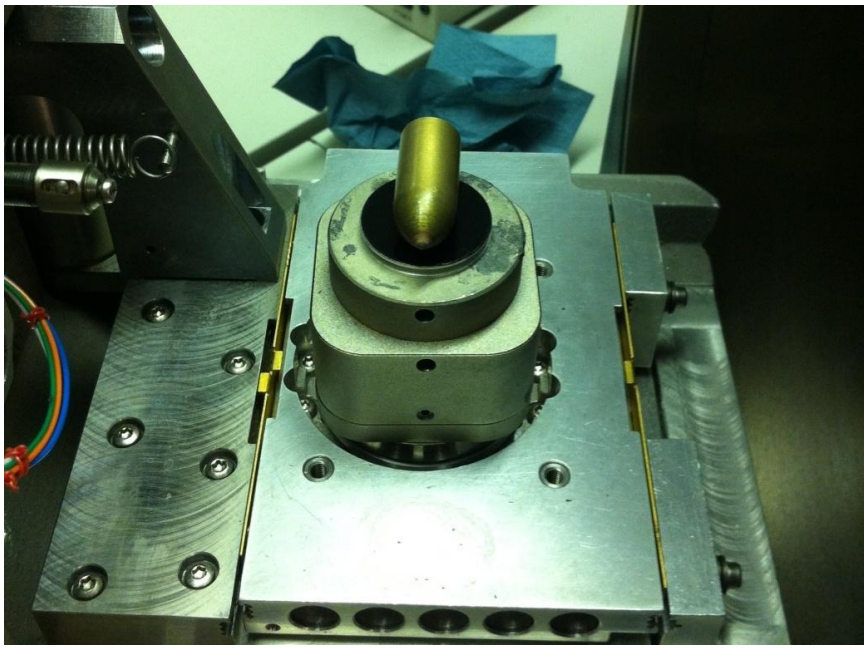

Figure 6.18: Rod electrode placed on the SEM tray

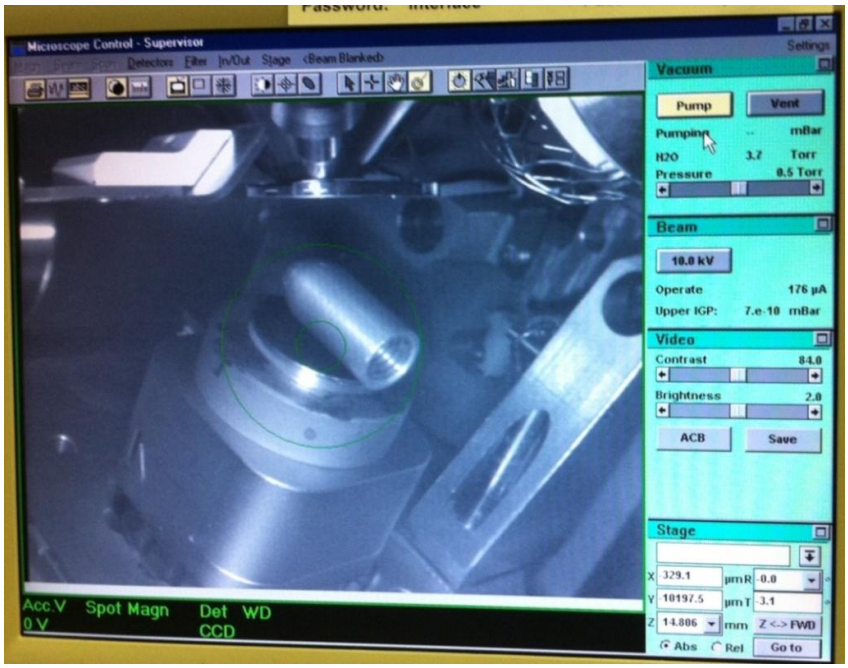

Figure 6.19: View from one of the cameras inside the SEM

Scanning electron microscope image for a rod electrode and plane electrode are shown in Figure 6.20(a) and Figure 6.20(b) respectively. The effects of sparkovers can be seen on both electrodes, in the form of rough surfaces.

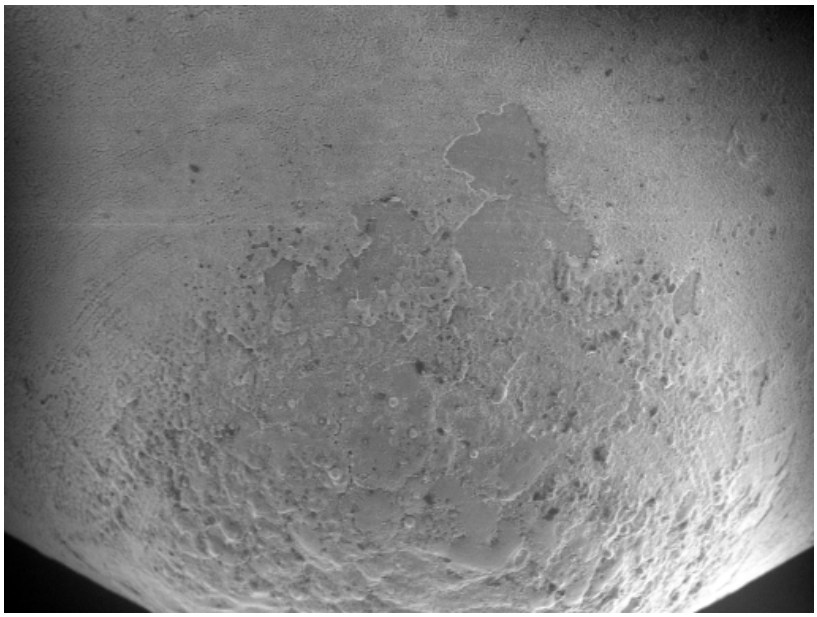

(a)

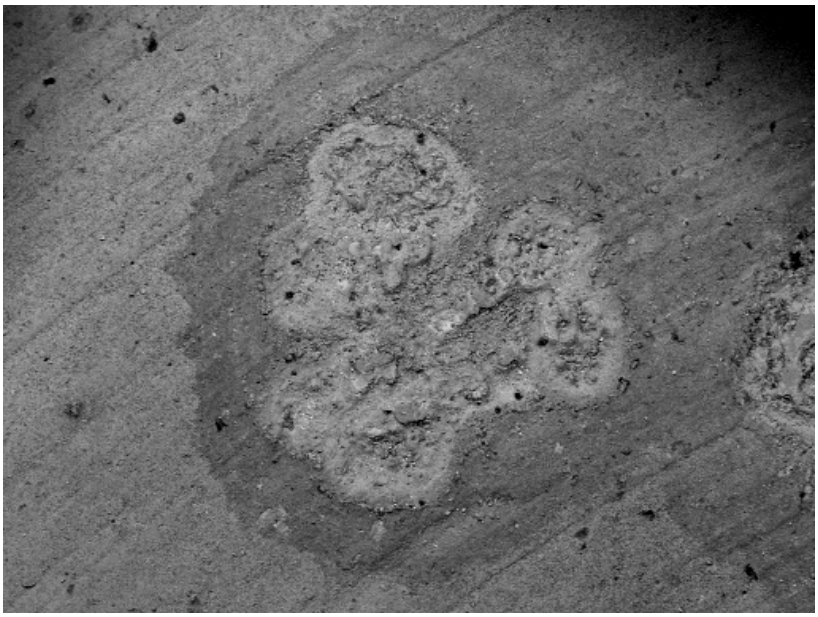

(b)

Figure 6.20: Electron image of (a) rod electrode, and (b) plane electrode

Figure 6.21 shows the spectrum analysis on the rod electrode, and Table 6.13 shows the detected elements in the weight and atomic percentage. Meanwhile, Figure 6.22 and Table 6.14 show the results from the plane electrode analysis.

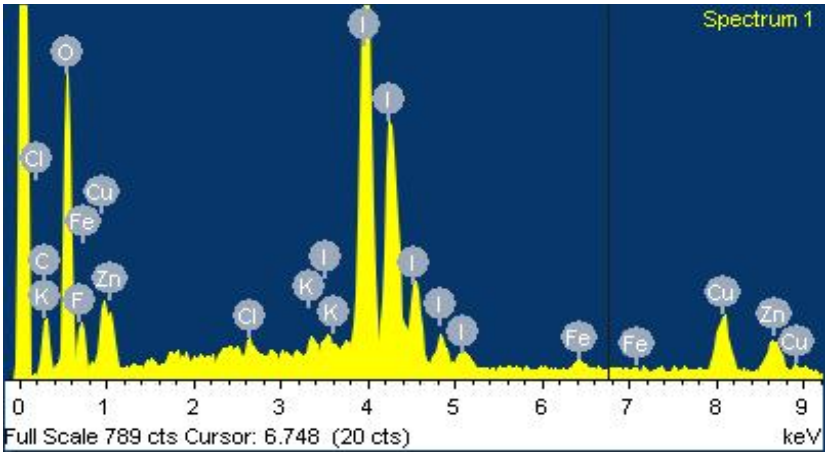

Figure 6.21: EDX spectrum on a rod electrode

Table 6.13: Element analysis from an EDX spectrum on a rod electrode

Element	Weight%	Atomic%
Carbon (C)	6.62	22.11
Oxygen (O)	13.54	33.98
Fluorine (F)	6.80	14.37
Chlorine (Cl)	0.48	0.54
Potassium (K)	0.53	0.54
Iron (Fe)	0.81	0.59
Copper (Cu)	9.73	6.15
Zinc (Zn)	7.69	4.72
Iodine (I)	53.80	17.01
Totals	100	100

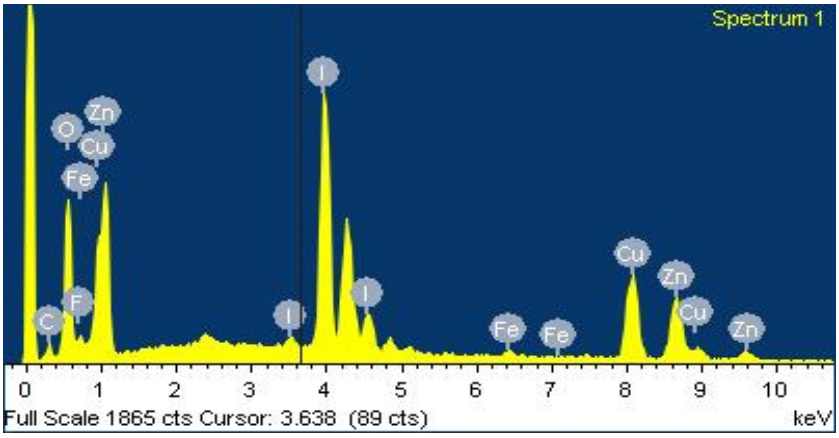

Figure 6.22: EDX spectrum on a plane electrode

Table 6.14: Element analysis from an EDX spectrum on a plane electrode

Element	Weight%	Atomic%
Carbon (C)	3.97	15.96
Oxygen (O)	10.93	32.98
Fluorine (F)	1.46	3.71
Iron (Fe)	0.71	0.61
Copper (Cu)	21.54	16.36
Zinc (Zn)	19.64	14.50
Iodine (I)	41.74	15.87
Totals	100	100

As can be seen from the above figures and tables, both rod and plane electrodes contain iodine as the main element. More iodine is deposited on the rod electrode contributing as much as 53.80% of the overall weight, while on a plane electrode, iodine is contributing 41.74%. If there is a solid dielectric between the high voltage electrode and ground electrode, iodine may deposit on the surface of the electrode and will significantly affect the insulation strength of the CF_3I gas, as was reported by Takeda et al. [47], [55]. An example of such deposition is shown in Figure 6.23.

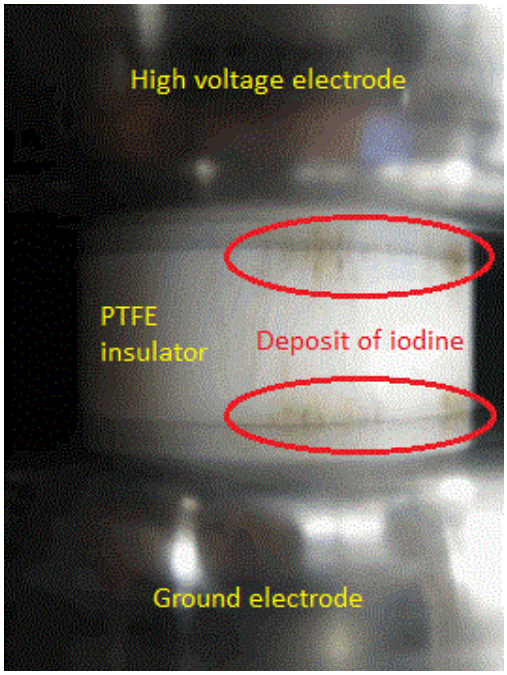

Figure 6.23: Surface condition of a PTFE insulator after flashover in CF_3I [47]

Based on the above analysis, it is important that efforts towards reducing the amount of iodine are carried out to ensure the insulation strength of the CF_3I gas and its mixtures are kept at the highest level. Other distinctive elements detected by the EDX include carbon and oxygen, which come from CO_2 gas, as well as copper and zinc, which are the elements in the electrode material consisting of brass.

6.5 Conclusion

This investigation concludes that higher pressures of CF_3I-CO_2 mixtures provide better insulation strength. The study in the rod-plane electrode configuration shows that U_{50} and E_{max} curves along the increasing gap length are the same in accordance with the impulse polarity. However, a smaller standard deviation is observed and calculated for higher pressure, particularly under a positive impulse polarity.

Although an increase in CF_3I content generally will increase the insulation properties of CF_3I-CO_2 gas mixtures, this study shows that the increment in insulation strength is more obvious in the plane-plane electrode configuration. In a rod-plane electrode configuration, the increase in insulation properties is more obvious only in the small gap at 1 cm.

Observation on solid by-products of CF_3I-CO_2 gas mixtures reveals that iodine is deposited on the electrode along with carbon and oxygen. However, iodine is more of a concern as it takes around 50% of the total weight and as has been proven to affect the insulation strength of CF_3I gas mixtures by previous research.

CHAPTER 7: GENERAL CONCLUSIONS AND FUTURE WORKS

The present work has been directed toward a better understanding of the CF_3I-CO_2 gas mixtures' insulation properties under standard lightning impulse stress. In order to achieve this, the work has focused on the development of an experimental test rig which included a test chamber integrated with some control measures and recovery system of the gas mixtures. The investigation has been successfully carried out to examine the effects of several factors on the insulation properties of the gas mixtures. The results from the experimental investigations are taken further to be used in computational modelling in order to get a better understanding of electric field effects under certain test conditions. Here, an overview of the research work findings and major conclusions are drawn, along with recommendations for future research work.

7.1 General Conclusions

An extensive review of previous work on CF_3I and its mixtures has been presented. The review highlights the need for a stronger understanding of the insulation characteristics of CF_3I gas mixtures in order to be employed as an insulation medium in high voltage applications. The topics covered include physical and chemical properties of CF_3I, electron interaction properties, thermal properties, electrical properties, by-products of CF_3I, and a toxicity review of the gas and by-products.

A new test rig has been developed specifically for gas research work, which includes a pressure chamber, control measures, and a recovery system of CF_3I gas mixtures. The air-tight pressure chamber was designed and tested to withstand pressures

of up to 5 bar (abs). Through help from a reliable sealing gland, wires were passed through the pressurised gas inside the vessel to the outside to provide a means of controlling the gap length of the electrodes, without the need of removing the gas. Other control measures include humidity, temperature, and pressure readings. The humidity and temperature are read wirelessly and from the readings, the necessary atmospheric corrections can be made according to standards.

Safety measures are equally important and were achieved by using a pressure relief valve. The valve is set to release the gas at 6 bar. Although the lifetime of pure CF_3I in the atmosphere is only around 1 day and the mixture under study is CF_3I-CO_2 (30%-70%) – which contain a lot less of CF_3I and a lot of CO_2, a recovery system of the gas mixture was used so that after each test, the gas was properly stored in cylinder bottles and not being released into the atmosphere. As it is important to study the 'deteriorated' gas mixture for future works, this recovery process provided a means of obtaining the deteriorated gas to be investigated.

In order to investigate behaviour under electric field, finite element modelling was used in computational works. A simulation model was developed based on each test condition, which includes electrode configurations, gap length, material used, and the voltage applied. The computational modelling made use of axis-symmetric features of the test rig, which consumed less time in computing and although it is in 2D, the results of the simulation were accurate. Only small discrepancies were noted between simulated results and calculated results. The electric field effects were quantified and the influence of electrode geometry and configuration can be further investigated.

Lightning impulse (1.2/50) tests were carried out to examine the breakdown performance of air and to test the reliability and calibration of the constructed test rig before further tests on CF_3I and its mixtures were performed. Atmospheric corrections

in dry tests, in accordance to BS EN 60060-1 standard, were carried out. As it is important to validate all test results, humidity and temperature controls were placed inside the test chamber. U_{50} of air was determined for various test conditions by using the up-and-down method.

Three different electrode configurations were used in the air breakdown tests, which simulated three different electric fields. The results from the up-and-down method were taken to determine the electric field, based on models for each electrode configuration. With a proper model in the computational works, the location of the maximum electric field was determined for each electrode configuration and the sparkover locations were easily anticipated if recording using a high speed camera is desirable.

Before any tests on CF_3I-CO_2 mixtures were carried out, a calculation was made to ensure enough CF_3I was available according to the desired pressure. This was important as to prevent shortage of CF_3I while filling it into the test chamber. By making use of Dalton's Law, partial pressure of one gas was determined according to the ratio of the CF_3I-CO_2 gas mixture. As a gas evacuation and filling system had been successfully developed, the gas mixing process was carried out carefully. To ensure a good mixture of gases were in place, the gas mixture was left for at least 24 hours prior to any tests.

A selection of three main electrode configurations was used in the tests, namely the sphere gap, rod-plane, and plane-plane electrode configurations. The effects of electrode geometry and gap lengths between the electrodes were also investigated. As expected, breakdown under negative polarity of lightning impulses were much higher in very non-uniform electric fields as compared to those under positive impulses. The difference increased with the electrode gap length. This was attributed to the space

charge build up which impeded the negative avalanche in negative streamers and required higher fields for the avalanche to occur. However, in this study, the highest breakdown level occurred in the sphere gap configuration and a small increase in gap length provided a significant increase in U_{50} values. Considering the effects of field utilization factor, which was based on different electrode configurations, CF_3I-CO_2 gas mixture performed better under a much more uniform field, as compared to non-uniform field.

An interesting finding was observed in the breakdown behaviour of CF_3I-CO_2 mixture by observing the *V-t* characteristics of each test condition. It was found that under a positive impulse, in a small gap rod-plane electrode configuration, namely a 1 cm gap, most of the breakdowns occurred very early, around the peak of the lightning impulse, approximately 1 – 2 μs. It is due to the appearance of leader discharges within small gaps. While for other test conditions, the breakdowns were more distributed along the wavetail of the lightning impulse, up to 15 μs.

The effects of pressures of CF_3I-CO_2 mixtures were also investigated with the same amount of mixture ratio, 30%-70%, and pressures of 1.0, 1.5, and 2.0 bar. It was found that an increase in pressure would increase the breakdown strength of the gas mixture. However, as the gas mixture was tested in a 1 – 5 cm gap of a rod-plane configuration, the standard deviation of E_{max} along the gap length became significantly smaller at a 2.0 bar, compared to those at a 1.0 bar. This means for higher pressure, a difference in U_{50} between a 1 cm and 5 cm gap became smaller.

To provide a better understanding on the effects of CF_3I content, further tests were carried out on CF_3I-CO_2 with 20%-80% and 40%-60% mixture ratios and compared to a 30%-70% ratio that was already under study. The tests were carried out under two different field conditions, represented by plane-plane and rod-plane electrode

configurations at 1 bar. Although the insulation strength of the CF_3I-CO_2 mixtures were increased with CF_3I content, there was no significant effect for the case of the rod-plane configuration under a positive impulse. The trends of U_{50} and E_{max} were the same for all mixtures under tests. It was found that the effects of CF_3I content were more obvious in the plane-plane electrode configuration compared with the rod-plane electrode configuration and it could be taken from the fact that CF_3I performs better under a more uniform field stress.

An interesting comparison was observed between the effects of pressure and the effects of CF_3I content in a rod-plane electrode configuration. If 1.0 bar of CF_3I-CO_2 (30%-70%) is taken as reference, an increase of pressure from 1.0 bar to 1.5 bar will provide an increase of partial pressure in CF_3I from 0.30 bar to 0.45 bar. On the other hand, at the same total pressure (1.0 bar), an increase in CF_3I content, namely from 30%-70% to 40%-60%, will provide an increase of partial pressure in CF_3I from 0.30 bar to 0.40 bar. If only the amount of CF_3I is taken into consideration, such that there is little difference between 0.40 bar and 0.45 bar, a more significant increase in insulation properties can be achieved with an increase in pressure of the CF_3I-CO_2 mixture, rather than an increase in CF_3I content. This is particularly beneficial if the cost of CF_3I considered too high.

The relationship between liquefaction temperatures of the CF_3I-CO_2 mixtures in relation to CF_3I content was developed building on two methods obtained from literature, by assuming CO_2 as an ideal gas. For low CF_3I content, such as a 30%-70% mixture, changes in CF_3I content were more affected than mixtures at high pressures. As was discussed, at 1.0 bar, a change in CF_3I content will affect more of the insulation performance in a plane-plane electrode configuration compared with a rod-plane electrode configuration. It is suggested that in a rod-plane configuration, CF_3I content

could be decreased, as it will not have an effect on insulation strength, but by doing that more benefit can be obtained in reduction liquefaction temperature. Also, the relationship is useful in determining the mixture ratio under various pressures for a given temperature. As an example, to maintain the liquefaction temperature at –50 ºC, around 35% of CF_3I is needed in 1.0 bar of CF_3I-CO_2 mixture, while less than 20% of CF_3I is needed in 2.0 bar of CF_3I-CO_2 mixture for that temperature.

For microscopic observation, SEM and EDX analysis were useful in investigating the elements of solid by-products. An observation into the electrodes under test revealed iodine as a main solid by-product of discharge in CF_3I gas. Both high voltage and ground electrodes are deposited with iodine after discharges. Upon closer microscopic observations, more iodine was found to be deposited on the high voltage electrodes. It is possible that iodine conducts current as carbon does in tracking phenomena, and thus contributes to a decreased CF_3I insulation property.

7.2 Future Work

Based on the work carried out in this study, the following areas have been identified for related future investigations:

a) *Investigations on more electrode profiles*: As it is important to understand properly the behaviour of CF_3I mixtures under various electric fields, other electrode configurations can be adopted in future investigations to represent more field utilization factors. Rod gap electrode configurations and Rogowski profile electrodes are suggested for future work.

b) *Extension of CF_3I content effects*: Tests on the effects of CF_3I content have shown different effects for rod-plane and plane-plane electrode configurations.

Work on other CF_3I-CO_2 mixture ratios, such as 10%-90% and 50%-50% could be interesting for future investigations.

c) *Extension of pressure effects*: As SF_6 has been used in higher pressures in high voltage equipment, such as 5 bar in gas circuit breakers, CF_3I mixtures should be tested at the same pressures to provide a like for like comparison with SF_6 in terms of insulation strength.

d) *Investigations on other CF_3I mixtures*: Other possibilities of gases that can be mixed with CF_3I are nitrogen (N_2) and tetrafluoromethane (CF_4). Although N_2 has a lower boiling point, it is known as a non-electron attaching gas. On the other hand, CF_4 has weak electron attaching properties with a boiling point slightly higher than N_2.

e) *Investigations on CF_3I by-products*: Since iodine is thought to have some effects on lowering the insulation strength of the CF_3I gas, it is important to put some effort into reducing the amount of iodine when a discharge occurs. Investigations on maintaining the insulation properties of CF_3I after some sparkovers deserve further consideration.

REFERENCES

[1] Commons Select Committees, "House of Commons - The Future of Britain's Electricity Networks - Energy and Climate Change," *Parliamentary*, 2010. [Online]. Available: http://www.publications.parliament.uk/pa/cm200910/cmselect/cmenergy/194/19404.htm. [Accessed: 30-Jul-2013].

[2] United States Environmental Protection Agency (EPA), "SF_6 Emission Reduction Partnership for Electric Power Systems," 2008. [Online]. Available: http://www.epa.gov/electricpower-sf6/basic.html.

[3] Environmental News Service, "Potent New Greenhouse Gas Discovered," 2000. [Online]. Available: http://www.fluoridealert.org/news/potent-new-greenhouse-gas-discovered/.

[4] Environment News Service, "California Limits SF_6, World's Most Potent Greenhouse Gas," 2010. [Online]. Available: http://www.ens-newswire.com/ens/mar2010/2010-03-02-091.html.

[5] J. Witkin, "California to Regulate 'Most Potent' Greenhouse Gas," 2010. [Online]. Available: http://green.blogs.nytimes.com/2010/03/10/california-to-regulate-most-potent-greenhouse-gas/.

[6] T. Takuma, O. Yamamoto, and S. Hamada, "Gases as a Dielectric," in in *Gaseous Dielectrics X*, L. G. Christophorou, J. K. Olthoff, and P. Vassiliou, Eds. New York: Springer Science + Business Media, Inc., 2004, pp. 195–204.

[7] Schneider Electric, "Innovation for MV distribution," 2012.

[8] Mitsubishi Electric, "Dry Air Inulated Switchgear," 2013. [Online]. Available: http://www.mitsubishielectric.com/company/environment/ecotopics/technologies/prod/switchgear/index.html. [Accessed: 11-May-2013].

[9] X. Q. Qiu, I. D. Chalmers, and P. Coventry, "A Study of Alternative Insulating Gases to SF_6," *Journal of Physics D: Applied Sciences*, vol. 32, pp. 2918–2922, 1999.

[10] Y. Qiu and E. Kuffel, "Comparison of SF_6/N_2 and SF_6/CO_2 Gas Mixtures as Alternatives to SF_6 Gas," *IEEE Transactions on Dielectrics and Electrical Insulation*, vol. 6, no. 6, pp. 892–895, 1999.

[11] Y. Qiu and Y. P. Feng, "Investigation of SF_6-N_2, SF_6-CO_2 and SF_6-Air as Substitutes for SF_6 Insulation," in *IEEE International Symposium on Electrical Insulation*, 1996, no. 2, pp. 766–769.

[12] M. Hikita, S. Ohtsuka, S. Okabe, and S. Kaneko, "Insulation Characteristics of Gas Mixtures including Perfluorocarbon Gas," *IEEE Transactions on Dielectrics and Electrical Insulation*, vol. 15, no. 4, pp. 1015–1022, 2008.

[13] M. Hikita, S. Ohtsuka, S. Okabe, and G. Ueta, "Breakdown Mechanism in C_3F_8/CO_2 Gas Mixture under Non-Uniform Field on the Basis of Partial Discharge Properties," *IEEE Transactions on Dielectrics and Electrical Insulation*, vol. 16, no. 5, pp. 1413–1419, Oct. 2009.

[14] N. Koshino, Y. Yoshitake, N. Hayakawa, and H. Okubo, "Partial Discharge and Breakdown Characteristics of CO_2-Based Gas Mixtures as SF_6 Substitutes," in in *Gaseous Dielectrics X*, L. G. Christophorou, J. K. Olthoff, and P. Vassiliou, Eds. New York: Springer Science + Business Media, Inc., 2004, pp. 217–222.

[15] K. Mochizuki, T. Ueno, H. Mizoguchi, S. Yanabu, S. Yuasa, and S. Okabe, "Evaluation of Interruption Capability on Various Gases," in in *Gaseous Dielectrics X*, L. G. Christophorou, J. K. Olthoff, and P. Vassiliou, Eds. New York: Springer Science + Business Media, Inc., 2004, pp. 265–270.

[16] H. Okubo and N. Hayakawa, "Dielectric Characteristics and Electrical Insulation Design Techniques of Gases and Gas Mixtures as Alternatives to SF_6," in in *Gaseous Dielectrics X*, L. G. Christophorou, J. K. Olthoff, and P. Vassiliou, Eds. New York: Springer Science + Business Media, Inc., 2004, pp. 243–252.

[17] U.S. Environmental Protection Agency, "SF_6 Gas Handling Procedure."

[18] ICF Consulting, "Byproducts of SF_6 Use in the Electric Power Industry," 2002.

[19] U.S. National Library of Medicine, "Hazardous Substances Data Bank (HSDB)," 2011. [Online]. Available: http://toxnet.nlm.nih.gov/cgi-bin/sis/htmlgen?HSDB. [Accessed: 11-May-2013].

[20] D. R. James, I. Sauers, G. D. Griffin, R. J. Van Brunt, J. K. Olthoff, K. L. Stricklett, Y. F. Chu, J. R. Robins, and H. D. Morrison, "Investigation of S_2F_{10} Production and Mitigation in Compressed SF_6-insulated Power Systems," *IEEE Electrical Insulation Magazine*, vol. 9, no. 3, pp. 29–41, 1993.

[21] The British Standard, "Gaseous Fire-Extinguishing Systems — Physical Properties and System Design," vol. 3. 2006.

[22] T. A. Moore, S. R. Skaggs, M. R. Corbitt, R. E. Tapscott, D. S. Dierdorf, and C. J. Kibert, "The Development of CF_3I as a Halon Replacement," The University of New Mexico, 1994.

[23] L. G. Christophorou, J. K. Olthoff, D. S. Green, U. S. G. P. Office, and E. D. and P. M. Division, "Gases for Electrical Insulation and Arc Interruption: Possible Present and Future Alternatives to pure SF_6," National Institute of Standards and Technology, 1997.

[24] E. Onal, “Breakdown Characteristics of Gases in Non-Uniform Fields,” *Journal of Electrical and Electronics Engineering - Istanbul University*, vol. 4, no. 2, pp. 1177–1182, 2004.

[25] National Institute of Standards and Technology, “Methane, trifluoroiodo-,” *NIST Reference Standard Data*, 2011. [Online]. Available: http://webbook.nist.gov/cgi/cbook.cgi?Formula=cf3i&NoIon=on&Units=SI. [Accessed: 14-May-2013].

[26] Molecular Spectroscopy Group of Ca’Foscari University, “Molecules Investigated.” [Online]. Available: http://venus.unive.it/molspectragroup/Molecules/MoleculesBody.htm. [Accessed: 13-May-2013].

[27] Subcommittee on Iodotrifluoromethane, Committee on Toxicology, Board on Environmental Studies and Toxicology, and Division on Earth and Life Studies, *Iodotrifluoromethane: Toxicity Review*. Washington, D.C.: National Academic Press, 2004.

[28] United Nations, “Kyoto Protocol to the United Nations Framework Convention on Climate Change,” 1998.

[29] IPCC Core Writing Team, R. K. Pachauri, and A. Reisinger, “Addendum-Errata of Climate Change 2007 Synthesis Report,” 2008.

[30] A. Haddad and D. Warne, “Advances in High Voltage Engineering,” *IEE Power & Energy Series 40*. The Institution of Electric Engineers, 2004.

[31] J. de Urquijo, A. M. Juarez, E. Basurto, and J. L. Hernandez-Avila, “Electron Impact Ionization and Attachment, Drift Velocities and Longitudinal Diffusion in CF_3I and CF_3I-N_2 Mixtures,” *Journal of Physics*, vol. D, no. 40, pp. 2205–2209, 2007.

[32] J. L. Hernandez-Avila, A. M. Juarez, E. Basurto, and J. de Urquijo, “Electron Interactions in CF_3I and CF_3I-N_2,” in *XXVIII International Conference on Phenomena in Ionized Gases*, 2007, pp. 139–142.

[33] J. de Urquijo, “Is CF_3I a good gaseous dielectric? A comparative swarm study of CF_3I and SF_6,” *5th EU-Japan Joint Symposium on Plasma Processing*, pp. 1–10, 2007.

[34] Y.-K. Deng and D.-M. Xiao, “The Effective Ionization Coefficients and Electron Drift Velocities in Gas Mixtures of CF_3I with N_2 and CO_2 obtained from Boltzmann Equation Analysis,” *Chinese Physics B*, vol. 22, no. 3, p. 035101, Mar. 2013.

[35] Y.-Y. Duan, L. Shi, M.-S. Zhu, and L.-Z. Han, “Critical Parameters and Saturated Density of Trifluoroiodomethane (CF_3I),” *Journal of Chemistry & Engineering Data*, vol. 44, pp. 501–504, 1999.

[36] Y.-Y. Duan, M.-S. Zhu, and L.-Z. Han, “Experimental vapor pressure data and a vapor pressure equation for trifluoroiodomethane (CF_3I),” *Fluid Phase Equilibria*, vol. 121, pp. 227–234, 1996.

[37] Air Liquide, “Sulfur Hexafluoride Vapor Pressure,” 2013. [Online]. Available: http://encyclopedia.airliquide.com/images_encyclopedie/VaporPressureGraph/Sulfur_hexafluoride_Vapor_Pressure.GIF. [Accessed: 13-May-2013].

[38] Air Liquide, “Carbon Dioxide Vapor Pressure,” 2013. [Online]. Available: http://encyclopedia.airliquide.com/images_encyclopedie/VaporPressureGraph/Carbon_dioxide_Vapor_Pressure.GIF. [Accessed: 13-May-2013].

[39] Air Liquide, “Nitrogen Vapor Pressure,” 2013. [Online]. Available: http://encyclopedia.airliquide.com/images_encyclopedie/VaporPressureGraph/nitrogen_vapor_pressure.gif. [Accessed: 13-May-2013].

[40] H. Katagiri, H. Kasuya, H. Mizoguchi, and S. Yanabu, “Investigation of the Performance of CF_3I Gas as a Possible Substitute for SF_6,” *IEEE Transactions on Dielectrics and Electrical Insulation*, vol. 15, no. 5, pp. 1424–1429, 2008.

[41] H. Kasuya, Y. Kawamura, H. Mizoguchi, Y. Nakamura, and S. Yanabu, “Interruption Capability and Decomposed Gas Density of CF_3I as a Substitute for SF_6 Gas,” *IEEE Transactions on Dielectrics and Electrical Insulation*, vol. 17, pp. 1196–1203, 2010.

[42] H. Kasuya, H. Katagiri, Y. Kawamura, D. Saruhashi, Y. Nakamura, H. Mizoguchi, and S. Yanabu, “Measurement of Decomposed Gas Density of CF_3I-CO_2 Mixture,” in *16th International Symposium on High Voltage Engineering*, 2009, pp. 744–747.

[43] H. Katagiri, H. Kasuya, and S. Yanabu, “Measurement of Iodine Density Generated from CF_3I-CO_2 Mixture after Current Interruption,” in *10th Japan-Korea Joint Symposium on Electrical Discharge and High Voltage Engineering*, 2007, pp. 295–298.

[44] M. Taki, D. Maekawa, H. Odaka, H. Mizoguchi, and S. Yanabu, “Interruption Capability of CF_3I Gas as a Substitution Candidate for SF_6 Gas,” *IEEE Transactions on Dielectrics and Electrical Insulation*, vol. 14, no. 2, pp. 341–346, 2007.

[45] European Committe for Electrotechnical Standardization, “BS EN 60060-1 : 2010 BSI Standards Publication High-voltage test techniques Part 1 : General definitions and test requirements,” 2010.

[46] H. Toyota, S. Nakauchi, S. Matsuoka, and K. Hidaka, “Voltage-time Characteristics in SF_6 and CF_3I Gas within Non-uniform Electric Field,” in *Proceedings of the 14th International Symposium on High Voltage Engineering*, 2005, p. 466.

[47] T. Takeda, S. Matsuoka, A. Kumada, and K. Hidaka, “Sparkover and Surface Flashover Characteristics of CF_3I Gas under Application of Nanosecond Square Pulse Voltage,” in *16th International Symposium on High Voltage Engineering*, 2009, pp. 812–817.

[48] H. Anis and K. Srivastava, “Pre-Breakdown Discharges in Highly Non-Uniform Fields in Relation to Gas-Insulated Systems,” *IEEE Transactions on Electrical Insulation*, vol. EI-17, no. 2, pp. 131–142, Apr. 1982.

[49] H. Toyota, S. Matsuoka, and K. Hidaka, “Measurement of Sparkover Voltage and Time Lag Characteristics in CF_3I-N_2 and CF_3I-Air Gas Mixtures by using Steep-Front Square Voltage,” *Electrical Engineering in Japan*, vol. 157, no. 2, pp. 1–7, 2006.

[50] T. Takeda, S. Matsuoka, A. Kumada, and K. Hidaka, “Insulation Performance of CF_3I and Its By-Products by Spark-over Discharge,” in *International Conference on Electrical Engineering*, 2008, pp. 1–6.

[51] T. Takeda, S. Matsuoka, A. Kumada, and K. Hidaka, “Breakdown Characteristics of CF_3I Gas in Uniform and Non-Uniform Field Gap Under Various Voltage Applications of Nanosecond Pulse to AC,” in *Fifteenth International Symposium on High Voltage Engineering*, 2007, pp. 7–10.

[52] S. Nakauchi, D. Tosu, S. Matsuoka, A. Kumada, and K. Hidaka, “Breakdown Characteristics Measurement of Non-uniform Field Gap in SF_6/N_2, CF_3I/N_2 and CF_3I/CO_2 Gas Mixtures by Using Square Pulse Voltage,” in *The XVI International Conference on Gas Discharge and Their Applications*, 2006, vol. 2, pp. 365–368.

[53] H. Toyota, S. Matsuoka, and K. Hidaka, “Voltage-Time Characteristics of SF_6-N_2 and CF_3I-N_2 Gas Mixtures in Nanosecond Range,” in *The XV International Conference on Gas Discharge and Their Applications*, 2004, no. September, pp. 395–398.

[54] H. Katagiri, H. Kasuya, H. Mizoguchi, and S. Yanabu, “BTF Interruption Capability of CF_3I-CO_2 Mixture,” in *Proceedings of XVII International Conference on Gas Discharges and Their Applications*, 2008, pp. 105–108.

[55] T. Takeda, S. Matsuoka, A. Kumada, and K. Hidaka, “Flashover Characteristics of CF_3I on the Dielectric Surface,” in *Proceedings of XVIII International Conference on Gas Discharges and Their Applications*, 2010, pp. 268–271.

[56] M. Dayah, “Dynamic Periodic Table,” 1997. [Online]. Available: http://www.ptable.com/. [Accessed: 05-Jun-2013].

[57] T. Takeda, S. Matsuoka, A. Kumada, and K. Hidaka, “By-products of CF_3I produced by Spark Discharge,” in *10th Japan-Korea Joint Symposium on Electrical Discharge and High Voltage Engineering*, 2007, pp. 157–160.

[58] M. Kamarol, Y. Nakayama, T. Hara, S. Ohtsuka, and M. Hikita, "Gas Decomposition Analysis of CF_3I under AC Partial Discharge of Non-Uniform Electric Field Configuration," in *10th Japan-Korea Joint Symposium on Electrical Discharge and High Voltage Engineering*, 2007, pp. 161–164.

[59] S. M. Webb, D. Jaksch, R. a. McPheat, E. Drage, E. Vasekova, P. Limão-Vieira, N. J. Mason, and K. M. Smith, "High-Resolution, Temperature Dependant, Fourier Transform Infrared Spectroscopy of CF_3I," *Journal of Quantitative Spectroscopy and Radiative Transfer*, vol. 94, no. 3–4, pp. 425–438, Sep. 2005.

[60] T. Takeda, S. Matsuoka, A. Kumada, and K. Hidaka, "Breakdown Characteristics of CF_3I on Dielectric Surface," in *2009 Korea-Japan Joint Symposium on Electrical Discharge and High Voltage Engineering*, 2009, pp. 104–107.

[61] M. N. Ngoc, A. Denat, N. Bonifaci, O. Lesaint, W. Daoud, and M. Hassanzadeh, "Electrical breakdown of CF_3I and CF_3I-N_2 gas mixtures," in *IEEE Conference on Electrical Insulation and Dielectric Phenomena*, 2009, pp. 557–560.

[62] N. M. Nguyen, A. Denat, N. Bonifaci, O. Lesaint, and M. Hassanzadeh, "Impulse Partial Discharges and Breakdown of CF_3I in Highly Non-Uniform Field," in *Eighteenth International Conference on Gas Discharges and Their Applications*, 2010, pp. 330–333.

[63] L. L. Burger and R. D. Scheele, "HWVP Iodine Trap Evaluation," Pacific Northwest National Laboratory, 2004.

[64] Sigma-Aldrich Co., "Sigma-Aldrich United Kingdom," 2013. .

[65] Sigma-Aldrich Co., "Pentafluoroiodoethane Safety Data Sheet," 2012.

[66] Sigma-Aldrich Co., "Hexafluoroethane Safety Data Sheet," 2012.

[67] Sigma-Aldrich Co., "Hexafluoropropene Safety Data Sheet," 2012.

[68] Sigma-Aldrich Co., "Trifluoroiodomethane Safety Data Sheet," 2012.

[69] Sigma-Aldrich Co., "Trifluoromethane Safety Data Sheet," 2012.

[70] Sigma-Aldrich Co., "Carbon Dioxide Safety Data Sheet," 2012.

[71] Sigma-Aldrich Co., "Sulfur Hexafluoride Safety Data Sheet," 2012.

[72] Sigma-Aldrich Co., "Air Safety Data Sheet," 2012.

[73] European Standard, "European Structural Steel Standard EN 10024-2 : 2004," *Grade designations, properties and nearest equivalent*. Corus UK Ltd., 2004.

[74] PlasticsEurope, "The Plastic Portal - Polycarbonate," 2010. [Online]. Available: http://www.plasticseurope.org/what-is-plastic/types-of-plastics/polycarbonate.aspx. [Accessed: 17-Jun-2013].

[75] HighLine Polycarbonate, “FDA and NSF Standard 51 Grades and UV Absorbers,” 2011. [Online]. Available: http://highlinepc.blogspot.co.uk/2011/05/fda-and-nsf-standard-51-grades-and-uv.html. [Accessed: 20-Sep-2013].

[76] City Plastics, “Polycarbonate Technical Data and Information Sheet,” 2005.

[77] Copper Development Association, “Types of Brass,” 2012.

[78] CCOHS, “Non-Sparking Tools : OSH Answers.” [Online]. Available: http://www.ccohs.ca/oshanswers/safety_haz/hand_tools/nonsparking.html. [Accessed: 07-May-2013].

[79] Firgelli Technologies Inc., “Miniature Linear Motion Series • L12,” vol. 1, no. 206, 2008.

[80] Phidgets Inc., “Product Manual 1066 - PhidgetAdvancedServo 1-Motor,” 2009.

[81] ANSI/IEEE, “IEEE Standard General Requirements and Test Procedure for Outdoor Apparatus Bushings,” 1976.

[82] International Electrotechnical Commission, “IEC 60137 - Insulated Bushing for Alternating Voltages Above 1000 V,” 2003.

[83] Oregon Scientific, “Advanced Weather Station with Atomic Time Model : BAR208HGA USER MANUAL,” pp. 3–4, 2000.

[84] Concept Engineering Ltd, “Concept CO_2 Heater,” 2000. [Online]. Available: http://www.concept-smoke.co.uk/concept_co2_heater_for_vicount_vulcan_smoke_generators.aspx. [Accessed: 06-Jun-2013].

[85] DILO Armaturen und Anlagen GmbH, *Operating Manual for Z579R03*, vol. 0, no. 49. 2012.

[86] S. Ohtsuka, M. Koumura, M. Cho, Y. Hashimoto, M. Nakamura, and M. Hikita, “Insulation Properties of CO_2/N_2 Gas Mixture with a Small Amount of SF_6,” in in *Gaseous Dielectrics IX*, Springer US, 2001, pp. 295–300.

[87] J. Wolf, *Manual Instruction of Impulse Voltage Generator Type SGS*. Haefely Test AG, 2002.

[88] J. Wolf, *Manual Instructions of the Charging Rectifier*. Haefely Test AG, 1998.

[89] J. H. Cloete and J. van der Merwe, “The Breakdown Electric Field between Two Conducting Spheres by the Method of Images,” *IEEE Transactions on Education*, vol. 41, no. 2, pp. 141–145, May 1998.

[90] P. G. Slade and E. D. Taylor, “Electrical Breakdown in Atmospheric Air Between Closely Spaced (0.2pm-40pm) Electrical Contacts,” in *Proceedings of*

the Forty-Seventh IEEE Holm Conference on Electrical Contacts, 2001, pp. 245–250.

[91] K. J. Bathe, *Finite Element Procedures*. Prentice Hall, 2006.

[92] P. B. Zhou, *Numerical Analysis of Electromagnetic Fields*. Berlin: Springer-Verlag, 1993.

[93] E. Kuffel and W. S. Zaengl, "Finite Element Method (FEM)," in in *High Voltage Engineering: Fundamentals*, 1st ed., Pergamon Press, 1984, pp. 266–279.

[94] R. N. Clarke and National Physics Laboratory, "Dielectric Properties of Materials," 2013. [Online]. Available: http://www.kayelaby.npl.co.uk/general_physics/2_6/2_6_5.html. [Accessed: 17-May-2013].

[95] S. Kasap, *Dielectric Materials: Relative Permittivity*, no. 2. Web-Materials, 2002, pp. 1–7.

[96] R. Kurtus, "Polar and Non-Polar Molecules," *School of Champions*, 2005. [Online]. Available: http://www.school-for-champions.com/chemistry/polar_molecules.htm. [Accessed: 17-May-2013].

[97] COMSOL, *AC/DC Module User's Guide*. COMSOL, 2012.

[98] E. Husain and R. S. Nema, "Analysis of Paschen Curves for Air, N_2, and SF_6 using the Townsend Breakdown Equation," *IEEE Transactions on Electrical Insulation*, vol. EI-17, no. August, pp. 4–7, 1982.

[99] G. R. Govinda Raju and R. Hackam, "Sparking Potentials of Dry air, Humid Air and Water Vapour between Concentric Sphere-Hemisphere Electrodes," *Proceedings of IEE*, vol. 120, no. August, pp. 927–933, 1973.

[100] J. Lux, "Pachen's Law," *High Voltage Experimenter's Handbook*, 2004. [Online]. Available: http://home.earthlink.net/~jimlux/hv/paschen.htm. [Accessed: 28-Jul-2013].

[101] M. S. Naidu and V. Kamaraju, "Paschen's Law," in in *High Voltage Engineering*, 4th ed., Tata McGraw-Hill, 2009, pp. 45–48.

[102] P. N. Mavroidis, P. N. Mikropoulos, and C. a. Stassinopoulos, "Discharge Characteristics in Short Rod-Plane Gaps under Lightning Impulse Voltages of Both Polarities," in *42nd International Universities Power Engineering Conference*, 2007, pp. 1070–1074.

[103] A. E. D. Heylen, "Sparking formulae for very high-voltage Paschen characteristics of gases," *IEEE Electrical Insulation Magazine*, vol. 22, no. 3, pp. 25–35, May 2006.

[104] J. S. Pearson and J. A. Harrison, “A Uniform Field Electrode for use in a Discharge Chamber of Restricted Size: Design and Performance,” *Journal of Physics D: Applied Physics*, vol. 2, no. 1, pp. 77–84, 1969.

[105] S.-Y. Woo, D.-H. Jeong, K.-B. Seo, and J.-H. Kim, “A Study on Dielectric Strength and Insulation Property of SF_6/N_2 Mixtures for GIS,” *Journal of International Council on Electrical Engineering*, vol. 2, no. 1, pp. 104–109, 2012.

[106] E. Kuffel and W. S. Zaengl, “Fields in Homogeneous, Isotropic Materials,” in in *High Voltage Engineering: Fundamentals*, 1st ed., Pergamon Press, 1984, pp. 224–232.

[107] P. R. Howard, “Process Contributing to the Breakdown of Electronegative Gases in Uniform and Non-Uniform Electric Fields,” *Proceedings of the IEE - Part A: Power Engineering*, vol. 104, no. 14, pp. 139–142, 1957.

[108] W. D. Greason, Z. Kucerovsky, S. Bulach, and M. W. Flatley, “Investigation of the Optical and Electrical Characteristics of a Spark Gap,” *IEEE Transactions on Industry Applications*, vol. 33, no. 6, pp. 1519–1526, 1997.

[109] T. Takuma, “Discharge Characteristics of Gaseous Dielectrics,” *IEEE Transactions on Electrical Insulation*, vol. EI-21, no. 6, 1986.

[110] Y. Hoshina, M. Sato, M. Shiiki, M. Hanai, and E. Kaneko, “Lightning Impulse Breakdown Characteristics of SF_6 Alternative Gases for Gas-Insulated Switchgear,” *IEE Proceedings - Science, Measurement and Technology*, vol. 153, no. 1, pp. 1–6, 2006.

[111] C. Jones, “Future Trends of Gas Insulated Substations,” in in *Gaseous Dielectrics X*, L. G. Christophorou, J. K. Olthoff, and P. Vassiliou, Eds. New York: Springer Science + Business Media, Inc., 2004, pp. 375–384.

[112] L. B. Loeb and A. F. Kip, “Electrical Discharges in Air at Atmospheric Pressure - The Nature of the Positive and Negative Point-to-Plane Coronas and the Mechanism of Spark Propagation,” *Journal of Applied Physics*, vol. 10, no. 3, pp. 142–160, 1939.

[113] C. N. Works and T. W. Dakin, “Dielectric Breakown of Sulfur Hexafluoride in Nonuniform Fields,” *Transactions of the American Institute of Electrical Engineers*, vol. 72, no. 5, pp. 682–689, 1953.

[114] L. Nierneyer, L. Ullrich, and N. Wiegart, “The Mechanism of Leader Breakdown in Electronegative Gases,” *IEEE Transactions on Electrical Insulation*, vol. 24, no. 2, pp. 309–324, 1989.

[115] A. H. Sharbaugh and P. K. Watson, “Breakdown Strengths of a Perfluorocarbon Vapor (FC-75) and Mixtures of the Vapor with SF_6,” *IEEE Transactions on Power Apparatus and Systems*, vol. 83, no. 2, pp. 131–136, 1964.

[116] M. J. Mulcahy, “Electrical Breakdown of Air and SF_6 Mixtures,” *Proceedings of the Institution of Electrical Engineers*, vol. 113, no. 11, pp. 1878–1880, 1966.

[117] S. J. MacGregor, I. D. Chalmers, and G. Street, “The Switching Properties of SF_6 Gas Mixtures,” in *Pulsed Power Conference*, 1989, pp. 510–513.

[118] Elimsan Group, “SF_6 Gas Circuit Breakers.”

[119] ABB Limited, “Indoor Live Tank SF_6 Circuit Breaker,” 2009.

[120] T. Yoshida, H. Fujinami, and T. Kawamoto, “V-t Characteristics of SF_6 Gas during Lightning Surges,” *Electrical Engineering in Japan*, vol. 119, no. 4, pp. 1232–1239, 1997.

[121] O. Yamamoto, T. Takuma, S. Hamada, and Y. Yamakawa, “Applying a Gas Mixture Containing c-C_4F_8 as an Insulation Medium,” *IEEE Transactions on Dielectrics and Electrical Insulation*, vol. 8, no. 6, pp. 1075–1081, 2001.

[122] W. Xing, G. Zhang, K. Li, W. Niu, X. Wang, and Y. Wang, “Experimental Study on Partial Discharge Characteristics of C_4F_8-N_2 Mixtures,” *Proceedings of the Chinese Society for Electrical Engineering*, vol. 31, no. 7, pp. 119–124, 2011.

[123] K. Yanallah and F. Pontiga, “A Semi-Analytical Stationary Model of a Point-to-Plane Corona Discharge,” *Plasma Sources Science and Technology*, vol. 21, no. 4, 2012.

[124] D. McMullan, “Scanning Electron Microscopy,” 1993. [Online]. Available: http://www-g.eng.cam.ac.uk/125/achievements/mcmullan/mcm.htm. [Accessed: 31-May-2013].

[125] J. Atteberry, “How Scanning Electron Microscopes Work,” *HowStuffWorks.com*, 2009. [Online]. Available: http://science.howstuffworks.com/scanning-electron-microscope.htm. [Accessed: 31-May-2013].

[126] Central Facility for Advanced Microscopy and Microanalysis, “Introduction to Energy Dispersive X-ray Spectrometry (EDS),” 1996.

APPENDIX A

PROTOTECH THE COMPLETE ENGINEERING SERVICE

J & L Greenaway, 112 Milton Road, Sutton Courtenay, Abingdon, Oxon, OX14 4BT, England
Tel: +44 (0) 1235 847070 Fax: +44 (0) 1235 847037 Email: sales@prototech.co.uk

TEST AND INSPECTION REPORT

Company……Pipaway Engineering Ltd……

Order No……..11058……

Item Description……..Mild Steel Cylinder ……

Quantity……..1 off……

Manufactured to Drawings… N/A……

Degreased to specification…. N/A……..

Pressure tested to drawing…Sketch 5/7/2010……

Testing has been completed in accordance with customer requirements using calibrated test equipment traceable to national standards. The results reported apply only to the sample as supplied.

Equipment: Digital Pressure Gauge LE02-1-30bar Serial No: 28942

Remarks

Mild Steel Cylinder assembly pressure tested using Dry Nitrogen at 10 bar, held for 30 minutes.
All welds checked using PH Gas Leak Detector Spray.
No pressure drop recorded.
No leaks located.

Pressure Equipment Regulations 1999 – Exempt
Regulation 4(2). Regulations shall not apply to the assembly of pressure equipment on the site and under the responsibility of the user.

Tested by……

Date….1st February 2011……..

QREC-PDN-06 (Rev 2)

APPENDIX B

SOLD ON SERVICE
BSP SALES Centre
PNEUMATIC : HOSE : HYDRAULIC
Unit 5, seawall Court, Seawall Road, cardiff CF24 5TH
Tel: (029) 2046 5451 Fax: (029) 2046 5455
e-mail: info@bspsales.com

BSP CALIBRATION CERTIFICATE
Certificate 002/11

Date of Test : 29/06/2011
Item : prv ¼-0-7

Equipment used:

1. Pressure Booster Pneumax Model Px 1740.50n
2. Pressure Gauge 0-14 Bar.

   Traceable to T.J Williams Calibration Certificate TJ48/10

Method:

Presssure applied to unit using pressure booster. Valve set to relieve at 6 bar and locked.

Calibrated by :

Signed: N T PARSONS.....

Date 29.06.2011

NOTE: ANY ALTERATION TO THE AS SUPPLIED VALVE WILL INVALIDTE THIS CERTIFICATE